TUHH
Hamburg
University of
Technology

Institute for Ship Structural Design and Analysis (M-10)

Master's Thesis

Development of a Floe-Ice Breaking Simulation for the Generation of Propeller–Ice Load Spectra

Entwicklung einer Simulation für das Brechen von Eisschollen zum Erstellen eines Propeller-Eislast Spektrums

Lina Sapp, B.Sc.

First examiner:	D.Sc. (Tech.) R. U. Franz von Bock und Polach
Second examiner:	Prof. Dr.-Ing. habil. Alexander Düster
Supervisor:	Angelo Mario Böhm, M.Sc.
Registration number:	50820

ORCID: https://orcid.org/0009-0002-4022-540X
DOI: https://doi.org/10.15480/882.8574

August 16, 2023

Abstract

Within the scope of this work, an icebreaking simulation for floe ice is developed and implemented. The existing failure descriptions of local failure by bending and global failure by cracking as well as failure by direct rotation are extended by a newly described local failure by cracking. This combines the failure initiation of cracking with the fracture pattern of failure by bending. The simulation is validated for both the fracture forces at the bow and the generated breaking pattern by comparison with observations. Furthermore, the impact of different simulative as well as physical parameters on the model is investigated by a parameter study.

The simulation can be applied to arbitrary ice floe fields in combination, in conjunction with the bow contour of different icebreaking vessels, to calculate the breaking pattern including the ice fragments that migrate under the bow. In this work, the PSRV S.A. Agulhas is primarily used, with additional comparative simulations for the RV Polarstern. Additionally, an algorithm is developed and applied to generate load and torque spectra based on the computed ice cusps from the icebreaking simulation. Finally, the generated torque spectrum is compared with field measurement data.

Zusammenfassung

Im Rahmen dieser Arbeit wird eine Eisbruchsimulation für Scholleneis entwickelt und implementiert. Neben den bestehenden Beschreibungen des lokalen Versagens durch Biegung und des globalen Versagens durch Rissbildung sowie des Versagens durch direkte Rotation kommt eine hier neu entwickelte Beschreibung des Versagens durch lokale Rissbildung zur Anwendung. Diese kombiniert die Versagensauslösung durch Rissbildung mit dem Bruchverlauf des Versagens durch Biegung. Die Simulation wird sowohl für die Bruchkräfte am Bug als auch für das erzeugte Bruchmuster durch Vergleich mit Beobachtungen validiert. Weiterhin wird der Einfluss verschiedener simulativer wie physikalischer Parameter auf das Modell durch eine Parameterstudie untersucht.

Die Simulation kann auf beliebige Eisschollenfelder in Kombination mit der Bugkontur verschiedener eisbrechender Schiffe angewandt werden, um das Bruchmuster einschließlich der Eisbruchstücke, die unter den Bug gezogen werden, zu berechnen. Die Simulationen in dieser Arbeit werden in erster Linie auf die PSRV S.A. Agulhas angewandt, mit zusätzlichen Vergleichssimulationen für die RV Polarstern. Darüber hinaus wird ein Algorithmus zur Erzeugung von Last- und Drehmomentspektren auf der Grundlage der berechneten Eisbruchstücke aus der Eisbruchsimulation entwickelt und angewandt. Abschließend wird das generierte Drehmomentspektrum mit Feldmessdaten verglichen.

Contents

List of Figures

List of Tables

List of Algorithms

List of Symbols

Symbol	Meaning	Unit
a	crack length	m
A_c	contact area between bow and ice floe	m^2
$A_{\text{crit,1}}$	critical area of floes to fail by direct rotation	m^2
$\bar{A}_{\text{cusp}}$	mean cusp area	m^2
$A_{\text{cusp}}^{\text{tot}}$	total area of cusps	m^2
A_{field}	total area of generated ice field (ice and open water)	m^2
$A_{\text{flip}}^{\text{tot}}$	total area of floes failed by direct rotation	m^2
A_h	horizontal intersection area between bow and ice floe	m^2
$A_{\text{ice,tot}}$	observed total ice-covered area	m^2
$\bar{A}_{\text{ice}}$	mean area per ice floe	m^2
$\mathbf{A}_{\text{ice,cat}}$	floe area for each diameter category	m^2
A_l	horizontal intersection at lower ice waterline area between bow and ice floe	m^2
A_{rotate}	area of floes fail by direct rotation	m^2
A_u	horizontal intersection at upper ice waterline area between bow and ice floe	m^2
A^{tot}	total area of cusps and floes failed by direct rotation	m^2
b	floe length in crack direction	m
$\mathcal{C}_{\text{bend}}$	bending part of local cracking line	-
$\mathcal{C}_{\text{Bezier}}$	Bezier curve in local cracking line	-
$\mathcal{C}_{\text{crack}}$	cracking part of local cracking line	-
$\bar{c}_{\text{ice}}$	observed mean ice concentration	-
D	flexural rigidity of the ice floe	kJ m^3
$\mathbf{d}_{\%}$	observed diameter distribution percentage	-
$\mathbf{d}_{\text{ice}}$	diameter of every diameter category	m
$d_{\mathbf{x}_{\text{pos}}^i, \mathbf{x}_{\text{pos}}^j}$	distance between floes i and j	m
$\text{dist}_{\text{bow}}^{\text{max}}$	maximal distance of ice floe to the bow	m
E	Young's modulus of the ice floe	GPa
E_{kin}	kinetic energy	kJ
F_c	crushing force	N
$F_{c,\text{avg}}$	averaged crushing force	kN
F_f	friction force	N
F_h	resulting horizontal forces on the bow	N
F_t	tensile force	N
F_v	resulting vertical forces on the bow	N
g	gravitational acceleration	$\frac{\text{m}}{\text{s}^2}$
G_c	fracture energy	kJ
$\bar{h}_{\text{ice}}$	observed mean ice thickness	m
h_{max}	maximum value for randomized ice thickness	m
h_{min}	minimum value for randomized ice thickness	m

Symbol	Meaning	Unit
h_{rand}	randomized ice thickness	m
$\bar{h}_{\text{rand}}$	mean value of randomized ice thickness	m
$i_{\text{lastCrack}}$	index of last cracking line point	-
k	foundation modulus of the ice floe	$\frac{\text{MN}}{\text{m}^3}$
K_I	stress-intensity factor for failure mode I	$\text{kN}\,\text{m}^{-3/2}$
K_{Ic}	fracture toughness	$\text{kN}\,\text{m}^{-3/2}$
l	length of the ice floe	m
ℓ	characteristic length of the ice floe	m
m	index of last cracking point	-
m_{cusp}	mass of the ice cusp	kg
$\mathbf{m}_d$	number of observed ice floes	-
m_{floe}	total number of observed floes	-
N	number of intersection zones of a single floe	-
n	index of first bending point	-
n_h	number of samples for randomized ice thickness	-
$\mathbf{n}_{\text{Bezier}}$	nodes of Bezier curve	-
$\mathbf{n}_{\text{bow},i}$	normal vector on bow segment i	-
n_{cusp}	number of cusps	-
n_{flip}	number of floes failed by direct rotation	-
n_{int}	number of intersection points	-
O	joint origin of all wedges	-
P	bending capacity	N
p	linear crack face loading	$\frac{\text{N}}{\text{m}}$
p_h	number of summed-up random numbers of randomized ice thickness	-
$P_{0.7_{\%}}$	pitch percentage of propeller blades	-
$P_{0.7}$	pitch of propeller blades	m
P_t	tensile capacity	N
$\mathbf{r}$	vector containing all floe radii	-
r	floe radius	m
$R_{0.7}$	70% of propeller radius	m
r_{prop}	propeller radius	m
rpm	rotations per minute of propeller	min^{-1}
T_{prop}	torque on the propeller around x-axis	kN m
V	volume of cusp or floe	m^3
$\bar{V}_{\text{cusp}}$	mean cusp volume	m^3
v_{cusp}	cusp velocity	$\frac{\text{m}}{\text{s}}$
$V_{\text{cusp}}^{\max}$	maximal volume for different cusp size categories	m^3
v_{ship}	vessel velocity	$\frac{\text{m}}{\text{s}}$
w	width of the ice floe	m
$w(x, y)$	lateral deflection of the flow in vertical direction	-
$\mathbf{x}_{\text{bow}}$	x-coordinates of bow nodes	-
$\mathbf{x}_{\text{crack}}$	nodes defining the cracking line	-

Symbol	Meaning	Unit
x_{end}	final position of the bow tip	m
x_{field}	length of the floe field	m
$\mathbf{x}_{\text{int}}$	intersection point between bow and ice floe	-
$\mathbf{x}_{\text{pos}}^{i}$	position vector of every ice floe	-
$\mathbf{X}_{\text{pos}}$	matrix containing all floe position vectors	-
x_{start}	initial position of the bow tip	m
x_{step}	discretization step width of bow movement	m
$\mathbf{y}_{\text{bow}}$	y-coordinates of bow nodes	-
y_{field}	width of the floe field	m
$\alpha_{\text{nextcrack}}$	Angle between possible cracks	$^\circ$
δ_P	propeller pitch angle	$^\circ$
μ	friction coefficient	-
ν	Poisson ratio of the ice floe	-
ν_t	total porosity of sea ice	-
φ	wedge discretization angle	$^\circ$
ψ	angle between the lead and the tangent to the hull	$^\circ$
ψ_{AGU}	angle between the lead and the tangent to the hull of PSRV S.A. Agulhas II	$^\circ$
ψ_{PS}	angle between the lead and the tangent to the hull of RV Polarstern	$^\circ$
ρ_{ice}	density of sea ice	$\frac{\text{kg}}{\text{m}^3}$
ρ_w	density of seawater	$\frac{\text{kg}}{\text{m}^3}$
σ_c	crushing strength of sea ice	$\frac{\text{N}}{\text{m}^2}$
$\sigma_{\text{ice}}^{\text{rand}}$	standard deviation for randomized ice thickness	m
σ_n^t	tensile strength (scale effect law)	$\frac{\text{N}}{\text{m}^2}$
σ_t	tensile strength	$\frac{\text{N}}{\text{m}^2}$
σ_T	transversal stress	$\frac{\text{N}}{\text{m}^2}$

Eidesstattliche Erklärung

Ich, Lina Sapp (Studentin des Theoretischen Maschinenbaus an der Technischen Universität Hamburg, Matrikelnummer 50820) versichere an Eides statt, dass ich die vorliegende Masterarbeit

> *Entwicklung einer Simulation für das Brechen von Eisschollen zum Erstellen eines Propeller-Eislast Spektrums*

selbstständig verfasst und keine anderen als die angegebenen Hilfsmittel und Quellen verwendet habe. Die Arbeit wurde in dieser oder ähnlicher Form noch keiner Prüfungskommission vorgelegt.

Hamburg, 20. Oktober 2023

Lina Sapp

1. Introduction

Ice-going vessels and especially their propulsion system are exposed to high forces due to contact with ice. The loads on the hull have been measured multiple times in the past[1, 2, 3] and can be calculated to some extent. However, the loads on the propeller are extremely difficult to measure directly. Propeller–ice contacts can cause substantial damage to the propeller or the bearing. For example, the German research vessel RV Polarstern had to cease an expedition in Antarctic regions due to damage at the variable pitch propeller [4]. The US Coast Guard heavy icebreaker USCGC Polar Star had a failure in the shaft seal, which resulted in flooding in one of the engine rooms. Even though the failure could be repaired quickly, some damage occurred and the ship's schedule was delayed by two days [5]. These are only two exemplary damage cases due to ice conditions at the propeller and the propulsion system. During the period 2007-2016, more than 450 shipping incidents happened in Arctic Circle waters, 198 of which were caused by machinery damage or failure [6]. For the Antarctic Circle waters, additional incident numbers can be assumed. The exact loads due to ice conditions on the propeller can only be estimated, but no reliable approach to calculate them with sufficient accuracy exists today. This leads to a lack of knowledge, which is compensated for by applying long-term experience in naval construction and sufficiently large factors of safety for relevant components. To allow more efficient construction and to guarantee more safety in ice conditions, there is gread interest to determine the exact loads due to the ice conditions.

One approach to determine the forces acting on the propulsion system due to ice contact is the indirect, reverse computation based on the torques measured on the shaft [7]. Even if there has been a lot of effort put into the numerical, reverse approach of calculating the forces acting on the propeller, the methods are computationally expensive and sensitive towards perturbations. Instead of this indirect approach, another approach is followed in this work: An icebreaking simulation for floe ice is developed and implemented based on the icebreaking simulation of level ice by Erceg et al. [8]. The ice floes are broken by the contact with the bow and the resulting pieces of the ice, the ice cusps, are pulled underneath the ship and migrate towards the propeller. The simulation is used to compute these ice cusps, which are then the basis to generate a load spectrum for the occurring contact forces between the propeller and the ice cusps.

A brief overview of the research done in the field of this work is given in Section 1.1. The developed algorithm to generate randomized floe ice fields is introduced and described in Chapter 2. Based on these floe fields, the algorithm of the developed ship–ice interaction simulation is described in Chapter 3. The different failure modes used during the simulation are introduced and explained in Chapter 4. The failure mode newly developed in this work is described in Section 4.3. The results of the application of the icebreaking simulation on the generated floe ice fields are discussed and validated against other works in Chapter 5. To determine the influence of different parameters used during the simulation, a parameter study is performed in Section 5.3. In Chapter 6, the computed ice cusps are used to generate a load spectrum on the propeller. The developed simulation and the assumptions made as well as the ice load spectrum generation algorithm are discussed in

Chapter 7. Finally, Chapter 8 sums up the results of this work and gives an outlook on possible further research based on this work.

1.1. Related Work

In the following, the research done around the scope of this work is described. The research field is divided into three different areas of interest: Sea ice modelling, ice–structure interaction, and propeller–ice interaction. Subsequently, this work is contextualised into the research field. The research work in the field of sea ice mechanics can be separated into different fields of interest: The field of sea ice modelling described further in Section 1.1.1, the field of ice–structure interaction with the resulting breaking of ice floes highlighted in Section 1.1.2 and the propeller–ice interaction as a special case of the ice–structure interaction in Section 1.1.3. This work is contextualised within these fields in Section 1.1.4

1.1.1. Sea Ice

The field of sea ice modelling contains the development of different ice model descriptions including material models for sea ice as well as mechanical properties of sea ice. According to Schulson et al. [9], the mechanical properties and the structure of sea ice can be described for different ice configurations. Sea ice can be roughly divided into level ice and floe ice. The level ice describes a closed ice sheet on the surface in contrast to the floe ice, which consists of single ice floes of different sizes. If ice floes collide with each other ice ridges can develop. These ridges are not regarded within the scope of this work. Another differentiation of sea ice is based on its age. First-year sea ice has a larger salinity and is more elastic than multi-year sea ice. The salt is contained in the seawater and therefore in the new ice conglomerates in brine channels. There, the sole diffuses out of the ice floe through to the bottom side, which leads to a decreasing salinity concentration with increasing age of the floe. In this work, a special case of new floe ice is considered: Pancake ice occurs, if the recently frozen sea is influenced by waves which break up the fresh ice sheet. The occurring floes collide with each other, which leads to a round shape of the floes. The engineering properties resulting from the different structures of sea ice are reviewed by Timco and Weeks [10].

Herrnring [11] developed a Mohr-Coulomb-based ice material model to describe the mechanical behaviour of granular ice. This model is intended to apply to different ice scenarios, for example, ice core simulation, level ice simulation or iceberg collision simulation.

Herman [12, 13, 14, 15] investigated the mechanical simulation of sea ice floes, especially on the clustering of sea ice floes due to the fluid dynamic forces between the floes and the surrounding water: Ice floes tend to cluster with neighbouring floes and especially larger floes contribute smaller floes in front of them while drifting due to the flow fields existing in the sea. The different floe formations in Arctic sea ice are described by Hopkins and Thorndike [16] and the drift of pancake ice in the marginal ice zone during Antarctic winter is described by Alberello et al. [17].

1.1.2. Ice Floe Breaking

The structure–ice interaction is another field of interest in the research area of ice modelling. The failure properties of the ice resulting from interaction with a body can be determined by different numerical methods. One of them is the discrete element method (DEM). For bending failure of thin plates on a linear elastic foundation Nevel [18] introduced a DEM approach for narrow free infinite wedges. This model is applied to level ice to determine the ice resistance of ships by Lindqvist [19].

The approach by Lindqvist is used by Erceg et al. [8] for level-ice breaking simulation using a DEM approach. Lu et al. developed a floe-ice breaking simulation method based on the approach by Nevel for both in-plane fracture [20] and out-of-plane failure [21] of an ice floe and validated this method against observation and measurement results of a full-scale scenario [22]. All these approaches are based on force-based, static regard of the structure–ice interaction with the breaking capacity of each ice floe as the relevant breaking parameter. Both Lu et al. [20] and Erceg et al. [8] calculate the resulting forces between the ship bow and the sea ice using a Winkler-based elastic foundation, analytically described by Li et al. [23]. This elastic foundation represents the hydrostatic influence of the water underneath the ice floe and is represented by a system of spring and damping units depending on the density of the water and the ice. The dynamic bending of an ice floe resting on a Winkler-type foundation is described by Kim et al. [24]. A bonded discrete element method for modelling the ship–ice interactions in both broken and unbroken sea ice fields is invented by Jou et al. [25]. They also classify the different failure scenarios of cracking and bending failure for different floe sizes and the direct flip of floes instead of the failure of the ice floe.

Another approach to simulate floe ice breaking is developed by Bažant et al. [26, 27] and Dempsey et al. [28], which includes the scale effect of ice floe diameters. This means that no linear correlation between the change in the floe size and the change in the tensile capacity exists. Using different scale effect laws for different scenarios allows to include these scale effects with a low computational effort. In contrast to the approaches by Lu et al. [20] and Erceg et al. [8], the approach by Bažant et al. is based on an energy-based regard of the structure–ice interaction. Instead of the breaking capacity, the critical breaking energy, also called fracture toughness, is regarded.

Huang et al. [29] developed a combined method of DEM and computational fluid dynamics (CFD) to determine the loads and forces on a ship moving through a field of floating ice floes, especially pancake ice. In that work, the focus is not on the ice breaking, but on the forces due to the additional resistance of the sea ice. In the same focus field, Uto et al. [30] investigated the resistance of an ice-going vessel in floe ice. Wang et al. [31] used an elastic ice model to numerically simulate the ice loads on a ship. They also focused on the ice loads on the bow rather than the ice breaking itself.

A numerical model for a real-time simulation of ship–ice interaction is developed by Lubbad and Løset [32]. This model can solve level ice as well as floe ice. The broken ice cusps computed are always triangular. Another two-dimensional discrete element approach is described by Sawamura [33]. The method is applied on floe ice with rectangular shapes and different sizes and with a continuous drift velocity and direction. All failures are assumed to be in-plane, meaning that no classical bending occurs.

1.1.3. Propeller–Ice Interaction

The propeller–ice interaction is regarded as a special case of structure–ice interaction since the propeller rotation leads to much larger contact velocities and resulting contact forces than the classical structure–ice interaction. Soininen [34] investigated the propeller–ice interaction on a model scale, validated it against full-scale measurements and developed a propeller–ice contact model for both solid and crushed ice. Veith [35] developed a mathematical model to simulate the cutting process during propeller–ice interaction and determine the occurring contact forces. Veith assumes the propeller to be a rigid body. Ice cusps are also defined as rigid bodies until contact between the cusp and the propeller occurs. The contact forces are validated using experimental data on laboratory ice. Additionally, the equations of motion based on the ship's hull contour are defined there.

The forces and failure patterns appearing in the case of propeller–ice contact are investigated multiple times for model-scale and laboratory granular ice for different contact loading rates. Böhm et al. [36, 37] drove model-scale experiments using a propeller-like indenter and laboratory granular ice on a low-speed scale ($\leq 0.2\frac{\mathrm{m}}{\mathrm{s}}$), to determine the contact forces, the specific strain energy and the failure pattern for two different-sized indenters. The contact forces occurring under high-speed contact conditions are investigated experimentally by Böhm et al. [38].

Another approach besides the measurement of model-scale experimental data is the usage of data analysis on different torque data measured at the propulsion shaft and other propulsion system components except for the propeller itself. Nickerson et al. [7] invented a reverse, numerical approach to determine the forces on the propeller based on the measured torques on the propulsion shaft. Purcell et al. [39] developed an inverse determination on the ice cusps appearing at the propeller by a frequency analysis of the torques measured at the propeller shaft.

1.1.4. Contextualization of this Work

In summary, lots of effort was put into the investigation of structure–ice and propeller–ice interaction. However, especially for the propeller–ice interaction, no computationally efficient approach has been successful. In this work, a new approach is developed: The propeller–ice forces are estimated based on the size of the broken ice cusps. Therefore, an icebreaking simulation for floe ice is introduced.

To allow the application of the new approach on observed ice fields, an algorithm to generate synthetic ice fields based on an ice observation protocol is developed. In contrast to the floe fields simulated by Herman [13], the computed floes are intended to be used as static ice information. Therefore, the floe fields in this work are made without a fluid simulation, but by solving one single optimization problem to save computational effort. These floes are then put into the icebreaking simulation.

The icebreaking simulation developed in this work uses a similar structure as the algorithm proposed by Lubbad and Løset [32], but in contrast, the ice floes computed in this work can be of arbitrary shape, not only triangular. Multiple failure modes are used within the icebreaking simulation. The failure by bending used by Erceg et al. [8] for level ice is adapted in this work to the simulation of floe ice. The different failure modes

by cracking used in this work are a combination of the force-based approach by Lu et al. [21] and the energy-based approach by Dempsey et al. [28]. Both of them are adapted and extended for the usage of arbitrarily shaped ice floes.

Using the ice cusps computed by the icebreaking simulation, a load spectrum at the propeller is generated. The load spectra are then compared to the data computed by Nickerson et al. [7] and Purcell et al. [39]. Both works are based on the same expedition measurement and observation data as used in this work.

2. Generation of Floe Fields

In this work, circular-shaped ice floes of different sizes and thickness are used. The main simulation case of this work is the simulation of a vessel proceeding in pancake ice. Pancake ice occurs when the water is moving during the freezing process due to waves: The small, growing floes collide with each other and potential edges are broken or deformed. This leads to floes of elliptical or mostly circular shape.

Two different cases are tested: First, to analyse the general breaking pattern systematically, a single floe at different positions with different dimensions is used. This scenario is further described in Section 5.2. Second, the more realistic scenario of randomized floe fields is studied.

2.1. Algorithm

Evaluation of Ice Observation Data The randomized floe fields are generated based on the field observation data of the expedition of the PSRV S.A. Agulhas II during December 2019 and January 2020. The observation data consists of the distributions and mean values of the sea ice concentration, the floe radii and the floe thickness and were sampled every ten minutes. The mean sea ice concentration describes the percentage of ice-covered water in relation to the total water area. A mean ice concentration of $\bar{c}_{\text{ice}} = 0\%$ denotes open water without any ice occurrence, whereas $\bar{c}_{\text{ice}} = 100\%$ is equivalent to a closed ice cover, which is called level ice. All ice concentrations between those two extrema denote the occurrence of ice floes. In this work, for certain samples, the mean values of the sea ice concentration and the floe thickness as well as the distribution of the floe diameter are used to create ice floe fields with the same characteristics as the observed one for different observation periods. The observation data used are shown in Table 1.

In the first step, the number of ice floes of every size category $\mathbf{m}_d$ based on the concentration and the size of the floes is determined as

$$\mathbf{m}_d = \mathbf{d}_{\%} m_{\text{floe}}$$

with the observed diameter distribution percentage $\mathbf{d}_{\%}$ and the total number of ice floes

$$m_{\text{floe}} = \lceil \frac{A_{\text{ice,tot}}}{\bar{A}_{\text{ice}}} \rceil.$$

The total ice-covered area is denoted as $A_{\text{ice,tot}}$ and the mean area per ice floe as $\bar{A}_{\text{ice}}$. To get the covered area $A_{\text{ice,tot}}$, the mean ice concentration $\bar{c}_{\text{ice}}$ is multiplied by the total area (ice and open water) of the generated ice field A_{field}:

$$A_{\text{ice,tot}} = \bar{c}_{\text{ice}} A_{\text{field}}.$$

For the mean area of each floe

$$\bar{A}_{\text{ice}} = \langle \mathbf{A}_{\text{ice,cat}}, \mathbf{d}_{\%} \rangle$$

holds with the area of each floe size category

$$\mathbf{A}_{\text{ice,cat}} = \pi \frac{\mathbf{d}_{\text{ice}}{}^{2}}{2}$$

and the diameter set

$$\mathbf{d}_{\text{ice}} = \{2.5, 7.5, 15, 60, 300\} \text{ m}$$

as listed in Table 1. This diameter set contains the equivalent diameters of the floes. In the following, the floes are handled as circular floes representing the equivalent circular shape of the observed floes. This is assumed since ice floes and especially pancake ice floes can be described approximately by a circle [12]. The diameter distribution $\mathbf{d}_{\%}$ can be found in Table 1 for different ice observation periods.

Table 1: Exemplary ice observation data from expedition Agu19/20

Date	**Time**		**Concentration**	**Thickness**	**Diameter Distribution** $\mathbf{d}_{\%}$ [%]				
	start	end	$\bar{c}_{\text{ice}}$ [%]	$\bar{h}_{\text{ice}}$ [m]	2.5	7.5	15	60	300 m
18/12/2019	20:20	20:30	44	0.36	20	40	40		
18/12/2019	22:30	22:40	89	0.82		40	40	20	
19/12/2019	04:40	04:50	79	1.12			20	60	20
30/12/2019	07:10	07:20	36	0.46		50	30	20	
30/12/2019	13:10	13:20	46	0.46	20	40	30		10
30/12/2019	16:10	16:20	79	0.62		20	40	40	
02/01/2020	15:20	15:30	41	0.30		20	50	30	
02/01/2020	17:50	18:00	45	0.84	20	50	30		
03/01/2020	13:40	13:50	19	0.25	45	33	22		
03/01/2020	17:40	17:50	52	0.32	30	20	50		

Generation of Floe Fields Afterwards, the positions of the floes are determined. In the first step, the floes are placed randomly inside the bounds of the ice floe field. Every floe is described by a radius r_i and a vector describing its position $\mathbf{x}^i_{\text{pos}}$. The radius of each floe is set for every floe such that the total diameter distribution $\mathbf{d}_{\%}$ is fulfilled. The position of the floes is set randomly as

$$\mathbf{x}^i_{\text{pos}} = \begin{pmatrix} x_{\text{rand}} x_{\text{field}} \\ y_{\text{rand}} y_{\text{field}} \end{pmatrix}, \quad x_{\text{rand}}, y_{\text{rand}} \in [0, 1]$$

with the length of the floe field x_{field} and the width y_{field}. The floe description parameters are stored in the vector $\mathbf{r} = (r_1, r_2, \dots)$ and the matrix $\mathbf{X}_{\text{pos}} = \left(\mathbf{x}^1_{\text{pos}}, \mathbf{x}^2_{\text{pos}}, \dots\right)$. In the second step, the positions are optimized using a sequential quadratic programming (SQP) algorithm, such that no overlapping of floes occurs and the floes stay inside the boundaries of the floe field.

To reach this, the following optimisation problem is solved:

$$\min_{\mathbf{X}_{\text{pos}}} f\left(\mathbf{X}_{\text{pos}}\right) \qquad s.t.\ g_i\left(\mathbf{X}_{\text{pos}}\right) \leq 0,\ i \in \{1,2,3,4,5\}$$

with the cost function

$$f\left(\mathbf{X}_{\text{pos}}\right) = \left| \min_{\mathbf{x}^i_{\text{pos}}} \left(\min_{\mathbf{x}^j_{\text{pos}}} \left(d_{\mathbf{x}^i_{\text{pos}}, \mathbf{x}^j_{\text{pos}}} \right) \right) - \max_{\mathbf{x}^i_{\text{pos}}} \left(\min_{\mathbf{x}^j_{\text{pos}}} \left(d_{\mathbf{x}^i_{\text{pos}}, \mathbf{x}^j_{\text{pos}}} \right) \right) \right| \ \forall i, j \in \{1, 2, \ldots, m_{\text{floe}}\}$$

with

$$d_{\mathbf{x}^i_{\text{pos}}, \mathbf{x}^j_{\text{pos}}} = \text{dist}\left(\mathbf{x}^i_{\text{pos}}, \mathbf{x}^j_{\text{pos}}\right) - \left(r_i + r_j\right)$$

representing the distances between the floes with center points $\mathbf{X}_{\text{pos}}$. Since floes tend to conglomerate, minimizing the distance between the floes is a logical approach [13]. The cost function f is optimized with subject to multiple constraints: First, no overlapping of ice floes is allowed. Therefore, the pairwise distance of the ice floes has to be larger than the pairwise sum of the radii:

$$g_1^{ij}\left(\mathbf{X}_{\text{pos}}, \mathbf{r}\right) = \begin{cases} \left| |r_i - r_j| - \text{dist}\left(\mathbf{X}^i_{\text{pos}}, \mathbf{X}^j_{\text{pos}}\right) \right| & i \neq j \\ 0 & i = j \end{cases}$$

Second, all floes must remain within the given boundaries of the desired floe field. Therefore, four additional constraints are used:

$$\begin{aligned} g_2\left(\mathbf{X}_{\text{pos}}\right) &= x_{\min}\mathbf{J}_{m_{\text{floe}},1} - \mathbf{X}^x_{\text{pos}} \\ g_3\left(\mathbf{X}_{\text{pos}}\right) &= \mathbf{X}^x_{\text{pos}} - x_{\max}\mathbf{J}_{m_{\text{floe}},1} \\ g_4\left(\mathbf{X}_{\text{pos}}\right) &= y_{\min}\mathbf{J}_{m_{\text{floe}},1} - \mathbf{X}^y_{\text{pos}} \\ g_5\left(\mathbf{X}_{\text{pos}}\right) &= \mathbf{X}^y_{\text{pos}} - y_{\max}\mathbf{J}_{m_{\text{floe}},1} \end{aligned}$$

The floe field boundaries are defined by the corner points $(x_{\min}, y_{\min})$, $(x_{\min}, y_{\max})$, $(x_{\max}, y_{\min})$ and $(x_{\max}, y_{\max})$. The vector of ones is defined as

$$\mathbf{J}_{m_{\text{floe}},1} = \begin{pmatrix} 1 \\ \vdots \\ 1 \end{pmatrix}, \quad \mathbf{J}_{m_{\text{floe}},1} \in \mathbb{R}^{m_{\text{floe}}}.$$

The floe fields are then saved, such that they can be used for simulation without the need to generate them again. Some exemplary floe fields are shown in Figure 1.

2.2. Validation

Since the ice observation data do not log the exact position of the ice floes and whether they are in the ship's surge direction, it is unknown which floes interact with the ship. To overcome this uncertainty, different floe fields for the same observation sample are

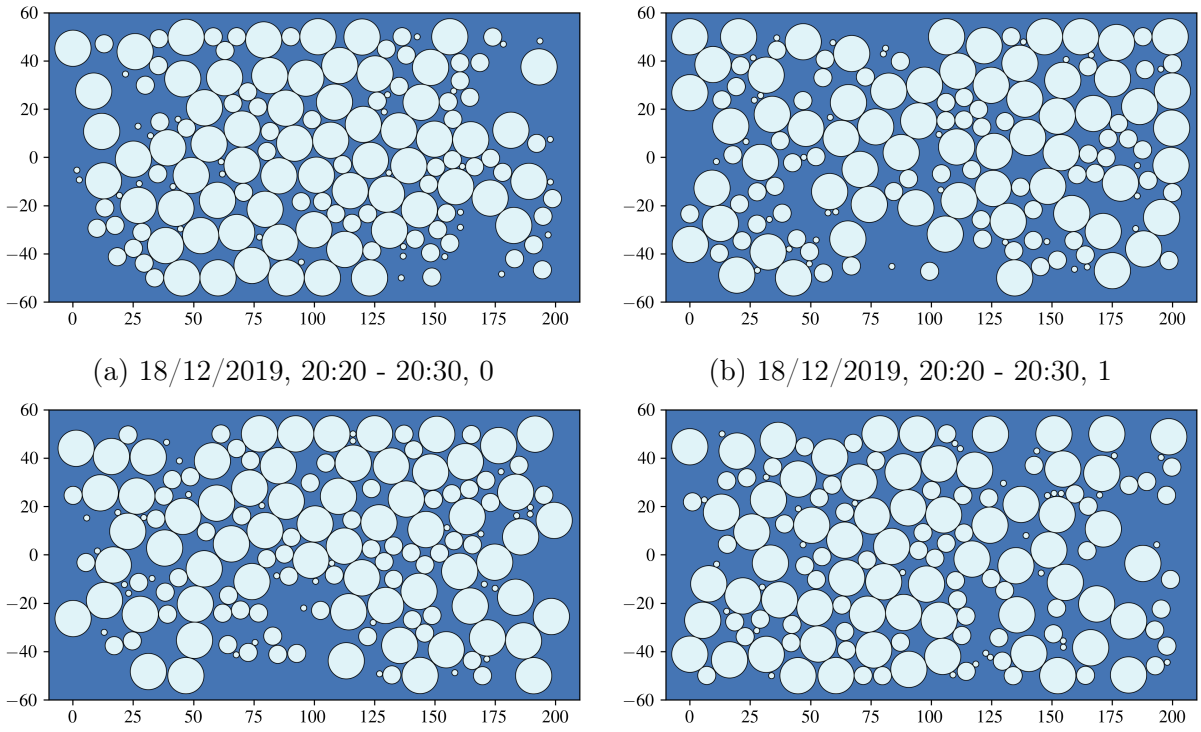

(a) 18/12/2019, 20:20 - 20:30, 0

(b) 18/12/2019, 20:20 - 20:30, 1

(c) 18/12/2019, 20:20 - 20:30, 2

(d) 18/12/2019, 20:20 - 20:30, 3

Figure 1: Four different examples for a randomized floe field using the data from observation at 18/12/2019, 20:20 - 20:30 as shown in Table 1.

tested using a Monte Carlo approach. The floes can not be validated directly, since no position observation of the ice floes was done during the expedition. Nevertheless, the generated, synthetic floe ice fields are compared to the observations and simulated models by Herman [13]. The same conglomeration phenomenon of floes of the same size as described by Herman occurs in the generated floe ice fields: Small floes take their bearings from the large ones and are surrounded by them. In particular, small floes rarely appear alone, but always with floes of similar size.

3. Ship–Ice Interaction

This section describes the model of the ice floes, the vessel, and the interaction process between the two components, as well as the simulation algorithm used for the icebreaking simulation. The ship–ice interaction model and especially the underlying assumptions are described in Section 3.1. The model is then applied to the floe fields described in Section 2 using the algorithm described in Section 3.2. The different failure modes are described in detail in Chapter 4.

In this work, the polar supply and research vessel PSRV S.A. AGULHAS II is regarded. This is a South African, polar class PC5 icebreaking vessel with a length of 134.2 m, a beam of 21.7 m and a draught of 7.65 m [40].

The coordinate system used in the following is shown in Figure 2. The x-axis points in the surge direction, the y-axis in the portside direction and the z-axis is perpendicular to the water surface pointing upwards. The bow contour is described for the upper ice waterline and the lower ice waterline. The upper ice waterline is the intersection between the bow and the upper surface of the ice floe, the lower ice waterline describes the intersection line between the bow and the lower surface of the ice floe. All bow points below the latter one are in contact with water and all points between the ice waterlines are in contact with the ice floe.

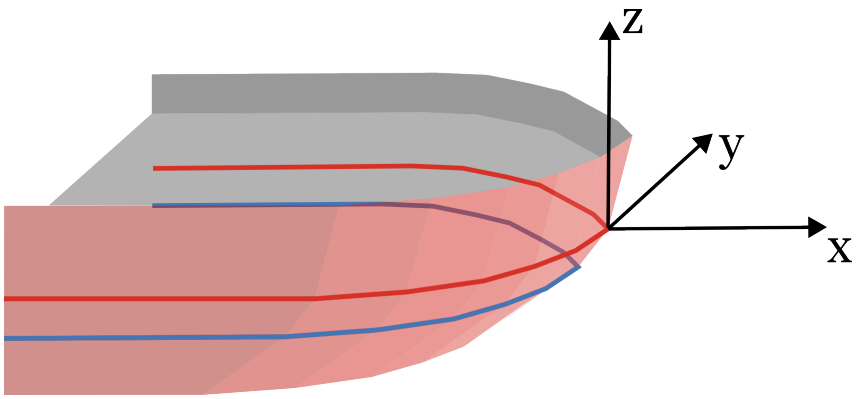

Figure 2: Coordinate system used in this work. The origin of the coordinate system is at the initial position of the tip of the upper ice waterline. The red line marks the upper ice waterline, and the blue line the lower ice waterline.

3.1. Assumptions

In the following, the assumptions used are introduced and explained. They are summed up in Table 2 and reviewed regarding the simulation results in Section 7.1.

General The icebreaking simulation model is built as a two-dimensional simulation with a parametrized third dimension. The two simulated dimensions are defined by the surface of the sea. The third, parametrized dimension is orthogonal to the surface of the sea. The sea is assumed to be flat, meaning that there are no waves.

Sea Ice Model The ice floes are assumed to be at fixed positions without rotation in the xy-plane, especially during the interaction with the bow. Therefore, no interaction between different ice floes occurs. Furthermore, the ice floes are handled as homogeneous bodies and brine channels as well as different salinity inside the floe are neglected. Especially, all grain boundaries inside the ice are neglected. The thickness of the floes is handled either as constant or as normally distributed with fixed minimal and maximal values of the thickness. Except for the energy-based cases of failure by cracking, the floes are modelled as rigid bodies laying on a Winker-type foundation and without any deformation until the final failure occurs. The ice floes remain in the two fully modelled dimensions as long as there is no contact with the hull. If there is contact with the ship, the floes can be bent or flipped using the parametrized third dimension.

Vessel Model The ship's hull is modelled as a rigid body. The bow is discretized in a fixed number of bow panels, which can be non-equally distributed. Each panel is assumed to be a linear plate, therefore no additional curves are modelled and the bow contour is not globally differentiable. Instead of simulating the vessel velocity, the vessel is moved forward by a predefined, constant step width. The predefinition of positions due to the fixed step width leads to the neglecting of the vessel velocity in the simulation and hence, all dynamical effects on the icebreaking process are neglected. The ship is moving forward parallel to the two fully modelled dimensions. The hull in the two fully modelled dimensions is completed in the third, parametrized dimension by defining the hull contour on different heights. It is assumed that the vessel can always proceed and does not get stuck in between the ice floes. To reach this, the propulsion power is assumed to be always high enough to compensate for the ice pressure. The upper and lower ice waterlines are assumed to be constant using a mean value over different ice thickness values. Especially, they do not adapt to different ice thickness values.

Ice–Structure Interaction The dimensions of the floe are the relevant parameters for the classification of the failure mode. Since the floes can have arbitrary shapes, the width and length of the floe are assumed to be the length and width of the cuboid bounding box around the floe. At the beginning of the simulation, there must not be any initial ice contact between the bow and the ice. The contact area between the ice floe and the bow is the crushing area. This is assumed to be rectangular, even if in reality the area is not rectangular due to the shape of the bow. If a floe fails neither by bending nor by cracking, but by direct rotation due to its position at the bow, it is assumed to stay beside the vessel. This case occurs if the floe is sufficiently close to the shoulder and too small to fail by bending. The failure cases are described detailed in Section 4.

In case of failure by cracking, a uniform cracking is assumed. This includes that the fracture modes shown in Figure 10 are not combined. In this work, only mode I fracture is regarded, since this is the dominant fracture mode during the interaction of the bow and especially the bow tip with the ice floe. If cracking is initiated, it is assumed to lead to a full crack. This assumption is associated with the assumption of no dislocations and a homogenous ice structure. Except for the case of punctual loading, cracking is regarded as an energy-based failure with the usage of fracture toughness. Depending on the load

cases described in Section 4, the fracture toughness and therefore the fracture energy is used for energy-regarded failure by cracking. Failure by bending is always handled as a force-regarded failure.

Table 2: Overview about the assumptions made for the different failure modes

Assumption	Bending	Cracking
General		
two-dimensional simulation, the third dimension is parametrized	✓	✓
neglection of waves	✓	✓
Sea Ice Model		
fixed floe positions	✓	✓
no interaction between floes	✓	✓
homogeneous ice, no grain boundaries	✓	✓
isotropic material behaviour of the ice	✓	✓
neglecting brine channels and varying salinity	✓	✓
ice thickness constant or normally distributed	✓	✓
ice floes are rigid bodies	✓	(✓) [2]
no deformation computed until failure	✓	(✓) [2]
Winkler-type foundation	✓	(✓) [2]
Vessel Model		
linear bow panels	✓	✓
rigid body	✓	✓
neglection of vessel velocity	✓	✓
dynamic effects are neglected	✓	✓
vessel force is assumed to be always sufficient	✓	✓
no vertical ship movement	✓	✓
fixed upper and lower ice waterlines for all ice thickness values	✓	✓
Ice–Structure Interaction		
failure classification based on rudimentary bounding boxes, not the real shape	✓	✓
uniform cracking, no combination of fracture modes		✓
cracking started once will lead to full crack		✓
floes rotated due to position at the bow stay beside the vessel	✓	✓
crushing area is calculated as rectangular-like shape	✓	✓
no initial contact between bow and ice at first step $x_{\text{step}} = 0$	✓	✓
force regarding	✓	(✓) [2]
energy regarding		(✓) [1]

[1] Not for punctual load case
[2] Only for punctual load case

3.2. General Algorithm

The simulation is executed stepwise for every position of the bow. During these steps, all floes are checked for contact and if contact occurs, the contact forces are calculated and evaluated regarding the failure conditions. Therefore, the ice floe is discretized in wedges with constant angle $\varphi = 5°$, as described by Erceg et al. [8]. A rough overview of the algorithm is given in Figure 3. The floes are handled independently from each other, and floe–floe interaction is not considered. Only floes that are near the hull are checked for contact. This is realized by computing the distance between each floe and the hull first. The vessel is moving forward to designated points, but the vessel speed is not modelled. This includes that the ship–ice interaction is evaluated for discrete position steps statically without considering dynamic effects.

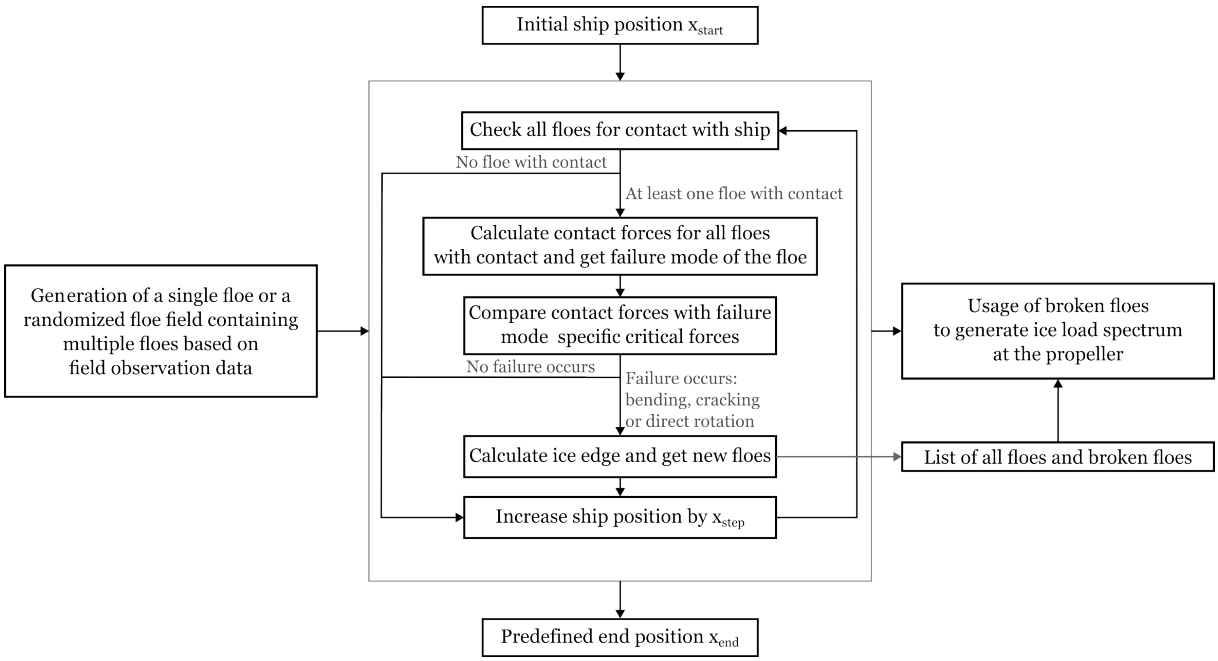

Figure 3: Overview of the algorithm for the ship–ice interaction

As depicted in the detailed flow chart of the algorithm provided in Figure 4, every simulation step starts by identifying all nearby ice floes using the Euclidian distance between the hull and the ice edge. All ice floes that have a distance below a certain threshold, e.g.

$$\mathrm{dist}_{\mathrm{bow}}^{\mathrm{max}} = 1.0\,\mathrm{m},$$

are used in the following simulation step. All other floes are ignored in this step and checked again at the beginning of the next step. Every floe near the bow is evaluated for intersection points with the hull, especially with the bow section. If there is no intersection, the current ice floe is ignored in this step. If there are at least two intersection points, the forces due to the ship–ice contact in horizontal and vertical directions are calculated. This is described in Section 4.1.1.

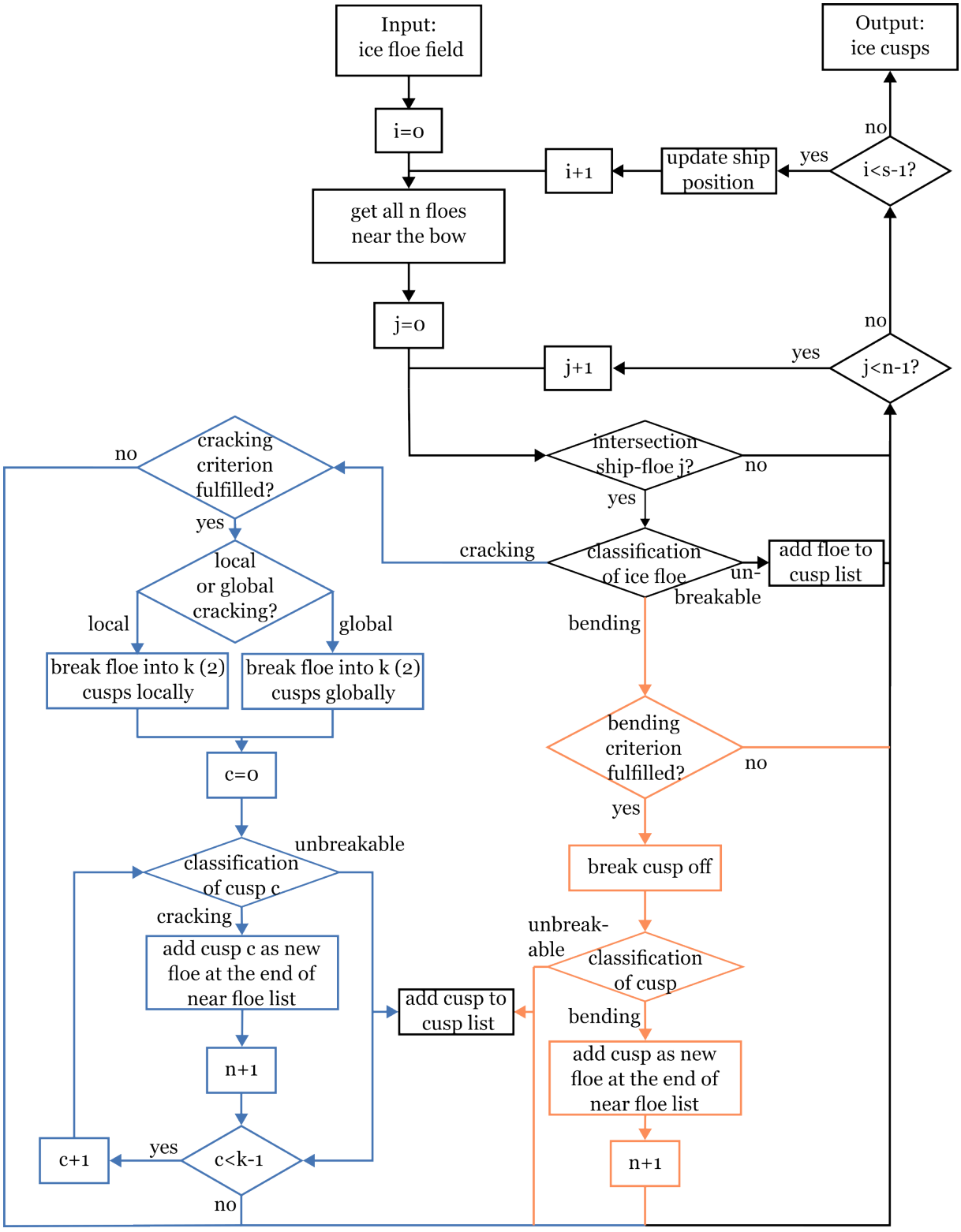

Figure 4: Flow chart of the algorithm for the ship–ice interaction

A single ice floe can have more than one intersection with the bow because the floes can be arbitrary polygons, that can be described as connected spaces. Arbitrarily shaped floes can also appear if the floes are initially modelled as circles since floes are broken in arbitrarily shaped cusps. The number of intersection zones is described by the parameter N. There must be at least two intersection points since every intersection zone is bounded by one intersection point per side. This leads to an even amount of intersection points n_{int}, as described by

$$n_{\text{int}} = 2N.$$

The next step is to decide in which way the floe will fail if it fails. The possible failure modes – local failure by bending, global failure by cracking or local failure by circumferential cracking and direct rotation of the ice floe – are described in the following sections. An overview of the possible failure scenarios is given in Figure 5. The algorithm used for the classification is shown in Appendix 2. An ice floe flips if the total area is below a certain threshold and the dimension ratios are inside a defined interval. The flipping of floes and the critical values are described in section 4.4.

After determining the failure mode, the acting forces are compared to a failure mode-specific critical force. In the case of bending, the vertical force component is compared to the maximal bending capacity, which depends on the ice thickness and the ice elasticity. In the case of cracking, either the critical stress intensity factor or the bending capacity is used as the threshold for the horizontal force component. Using the bending capacity instead of the tensile strength is an assumption made because the tensile capacity of sea ice is difficult to determine. Since the bending capacity of ice is larger than the tensile strength, higher crushing forces and larger cusps can occur. This leads to a conservative estimation of the cusp sizes. The algorithms for the different failure modes are described in Appendix 4, 5 and 6.

If this threshold is exceeded, the floe is either cracked into new floes or a part of the floe is separated by bending. For both the special algorithms are explained in sections 4.1, 4.2 and 4.3. After breaking the ice floe, the resulting ice cusp is once again checked for failure mode and broken if the related condition is fulfilled. This will be repeated until all cusps are classified as unbreakable instead of bending or cracking.

The decision of whether the floe fails by cracking or bending depends on the length l and width w of the floe. The length is always the dimension orthogonal to the current bow section, the width is parallel to the current bow section. To respect the thickness of the floe, the characteristic length of the floe ℓ is defined as

$$\ell = \sqrt[4]{\frac{D}{k}} \tag{1}$$

with the flexural rigidity of the ice floe

$$D = \frac{Eh^3}{12(1-\nu^2)},$$

where k is the foundation modulus, E is Young's modulus, h is the thickness of the ice floe and ν is the Poisson ratio [21].

The floe fails by bending if either both the width and the length of the floe are bigger than the doubled characteristic length, meaning

$$w > 2\ell \wedge l > 2\ell, \tag{2}$$

or if the width of the floe is lower than the length of the floe, although the width of the floe is lower than the doubled characteristic length:

$$w < l \wedge w \leq 2\ell, \tag{3}$$

In the last case, the absolute value of the length of the floe is not important. The value of the length could also be below the doubled characteristic length. If the width and the length of the floe are smaller than the doubled characteristic length and the width is bigger than the length of the floe, meaning

$$w > l \wedge l \leq 2\ell, \tag{4}$$

the floe will fail by cracking.

There are two cases where the floe is considered unbreakable. A floe that is considered unbreakable is classified as failed as soon as it is rotated out of the xy-plane.

In the first case, the total area of the floe is below a predefined threshold depending characteristic length of the floe ℓ. Lu et al. [21] assumed the characteristic length of ice floes for rectangular floes to be

$$\ell = 13.5h^{\frac{3}{4}}$$

with the ice floe thickness h. A floe will neither fail by bending nor by cracking if the length and width of the floe are smaller than the characteristic length ℓ, which leads to a maximal floe area of

$$A_{\text{rotate}} = \ell^2 = 13.5^2 h^{\frac{3}{2}}$$

for quadratic floes. Since arbitrarily shaped floes are used in this work, the threshold for failing by direct rotation without checking for the other failure modes is set to

$$A_{\text{rotate}} = 1\,\text{m} \cdot \ell. \tag{5}$$

This assumption allows small floes to be directly classified as unbreakable without additional computational effort. All floes above this threshold are tested for failure by direct rotation using the second criterion.

The second case occurs if the floe area is above the threshold defined by Equation (5). Then, the floe is checked for failure by bending or cracking, as described in Equations (2), (3) and (4). If none of them occurs, the floe fails by direct rotation.

If the floe fails and the resulting cusp neither fails by bending nor by cracking, it is assumed to be finished and is listed as a cusp. The shape and the initial position of the cusps are logged. This information can be used to determine the path of the cusp below the hull and towards the propeller. After computing all interactions between the hull and the ice segments in the current step, the vessel is moved forward by the step width x_{step}. If all floes are broken and all resulting ice segments are handled as ice cusps, the simulation ends. Otherwise, the simulation continues until the predefined simulation endpoint x_{end} is reached.

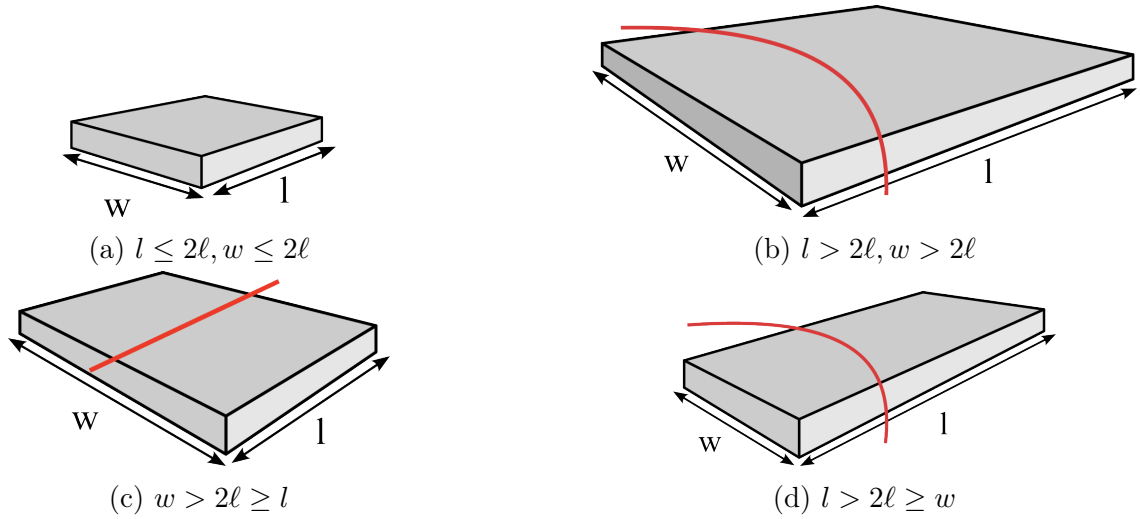

(a) $l \leq 2\ell, w \leq 2\ell$ (b) $l > 2\ell, w > 2\ell$

(c) $w > 2\ell \geq l$ (d) $l > 2\ell \geq w$

Figure 5: Failure scenarios of a single ice floe depending on the floe size. The floe is bent for floes with a length and width bigger than the critical length (b) and for narrow and long floes (d). The floe is cracked globally or locally for short and wide floes (c). If no initial crack point exists or the floe is narrow and short, the floe is flipped (a).

4. Failure Modes

The possible failure modes described in Section 3.2 are detailled in this section. Failure modes can be separated into local and global failure [21]. A local failure concerns only a limited area of the floe, whereas a global failure affects the whole floe. Another differentiation is the in-plane failure versus the out-of-plane failure. During the first, the floe is not rotated out of the xy-plane, in the latter case, the floe is at least partially rotated. Four different failure modes are considered in this work: The local out-of-plane failure by bending as described by Erceg et al. [8] and Lu et al. [21], the global in-plane failure by cracking described by Lu et al. [20] and Dempsey et al. [28], a newly invented local in-plane failure by cracking and the failure by direct rotation [21].

4.1. Bending

The bending formula used is based on the approach by Nevel [18] to model a narrow free infinite wedge on an elastic foundation. Narrow means that the wedge has a sufficiently small width, such that tangential bending can be neglected. Free means that apart from the contact force at the wedge tip and the reaction force of the base, no other forces act on the wedge. As a base, a Winkler-type foundation is used to model the elastic behaviour of the sea surface concerning the ice floe position. Figure 6 shows an elastic plate on a Winkler-type foundation. A simplified Winkler-type foundation consists of a spring system below an elastic plate and can be described mathematically by

$$D\nabla^4 w + kw = F_v \delta(x - x_0)\delta(y - y_0)[21]$$

with the lateral deflection in vertical direction $w(x, y)$, the vertical forces acting on the floe F_v and the coordinates of the force application point (x_0, y_0), the foundation modulus $k = \rho_w g$ with the density of the seawater ρ_w, the gravitational acceleration g and the Dirac function δ. The biharmonic operator is defined as

$$\nabla^4 = \frac{\partial^4}{\partial x^4} + 2\frac{\partial^4}{\partial x^2 \partial y^2} + \frac{\partial^4}{\partial y^4}.$$

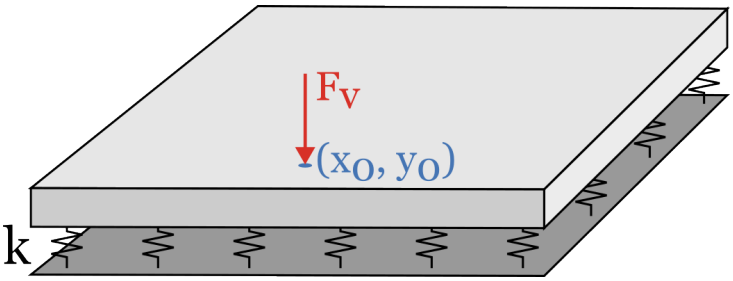

Figure 6: Linear elastic plate on a Winkler-type foundation. The vertical force F_v acting on the plate at the force application point (x_0, y_0). The foundation modulus is denoted as k.

The floe is modelled using the discrete element method (DEM). The main principle of the DEM includes that a solid body is discretized in multiple solid elements. In this work, the ice floe is discretized in wedges with regular angle φ, as described by Erceg et al. [8] and Kim et al. [24] and shown in Figure 7. If a contact between the bow and the ice occurs, the contact forces are determined separately for each wedge and afterwards compared to the maximum bending capacity of sea ice. If the maximum bending capacity is reached at least in one wedge, the whole floe is broken.

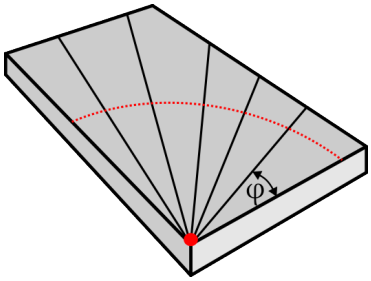

Figure 7: Discretization of the ice floe in wedges with regular angle φ [8]

4.1.1. Contact Force Determination

The contact forces are computed using the contact area and the contact angle at the corresponding bow segment, as described by Erceg et al. [8] and shown in Figure 8. The assumption made to calculate the contact area is a linear bow contour line. The bow is modelled in two layers, one is at the upper ice waterline, the other at the lower ice

waterline. The area of the ice floe that is between these two ice waterlines is named A_h. In this case, the waterlines are projected onto the same layer, e.g. the top surface of the ice floe. To determine A_h, the intersection area of the lower ice waterline with the ice floe A_l and the intersection area of the upper ice waterline with the ice floe A_u are calculated.

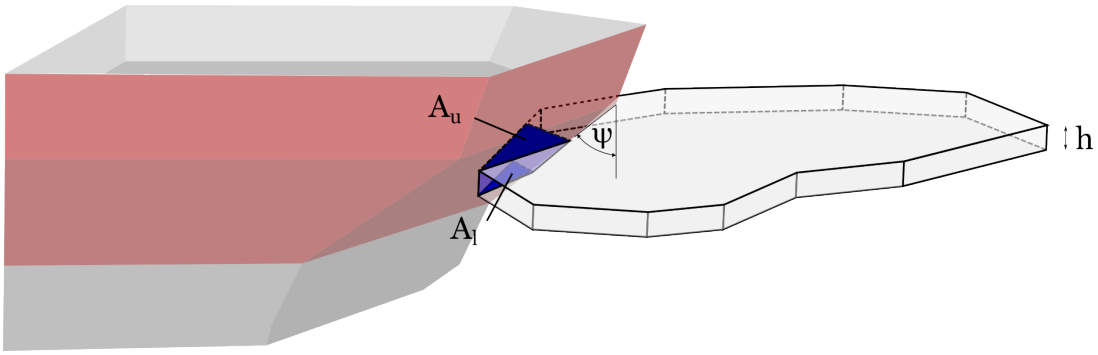

Figure 8: Ship–ice contact. The upper and lower crushing areas A_u and A_l are marked in blue. The bow panel angle ψ is the angle between the tangent panel on the bow and the z-axis.

The horizontal intersection area is then calculated as

$$A_h = A_u - A_l.$$

Afterwards, the horizontal intersection area is projected onto the bow to determine the contact area between the ship and the ice floe. The part of the ice floe that is calculated to be inside the bow is assumed to be crushed. With the angle ψ between the perpendicular represented by the z-axis and the vertical tangent to the hull, the contact area A_c can be determined as

$$A_c = \frac{A_h}{\sin(\psi)}. \tag{6}$$

The crushing force is calculated as

$$F_c = \sigma_c A_c \tag{7}$$

with the crushing strength of ice σ_c. Additionally to the crushing force the force due to friction between the bow and the ice floe must be regarded. This is realised by taking into account the friction force

$$F_f = \mu F_c \tag{8}$$

with the friction constant μ. The resulting forces in the vertical and horizontal directions due to the crushing force and the friction force are described by the vertical force

$$F_v = F_c \cos(\psi) - F_f \sin(\psi) \tag{9}$$

and the horizontal force

$$F_h = F_c \sin(\psi) + F_f \cos(\psi). \tag{10}$$

The relevant component of the crushing force F_c concerning bending is the vertical component F_v. The ice floes are assumed to be linear elastic with Young's modulus $E = 2\,\mathrm{GPa}$ and Poisson coefficient $\nu = 0.3$, as described and verified by Erceg et al. [8] using a finite element computational model.

4.1.2. Bending Line Determination

Based on the calculated vertical component of the crushing force F_v, the bending moment of each ice wedge is calculated. The ice wedges are equally distributed using a constant wedge angle. Erceg et al. [8] showed that the approach by Nevel [18] is valid for wedge angles below $\varphi_{\mathrm{crit}} = 60°$. Since the bending line consists of the same amount of points as there are wedges, a smaller wedge angle leads to a finer resolution of the resulting curve. To get a compromise between calculation effort and resolution the wedge angle is set to be $\varphi = 5°$ in this work.

The bending capacity P describes the maximum bending force that can be applied on the floe without failure by bending. Therefore,

$$F_v > P \tag{11}$$

has to be fulfilled for the vertical component of the crushing force F_c to cause a failure by bending. The bending capacity is defined as

$$P = \frac{1}{2}\sum_{i=1}^{2}\frac{1}{2}\sum_{j=1}^{2}\frac{1}{2}\sum_{k=1}^{2} P_{\mathrm{interpol}}(h_i r_j \beta_k)$$

with the interpolated bending capacity P_{interpol} defined by Erceg et al. [8]. The computations used to determine the interpolated bending capacity are shown in Appendix A.4.

To define the bending line, the breaking length of every wedge is calculated starting at the joint origin of all wedges O. The joint wedge origin is calculated based on the intersection area between the bow and the ice floe. The breaking length is the distance along the centre of the wedge where the maximum bending moment occurs. This moment is calculated using the discrete polynomials by Nevel [18] for a semi-infinite narrow free wedge. Erceg et al. [8] proved the validity of the approach by Nevel applied on semi-infinite wedges as used in this work too. If the bending condition is fulfilled, the floe is split into two floes using the computed bending line. Both new floes are then handled again as described in Section 3.2.

4.2. Cracking

Besides the failure by bending, an ice floe can also fail by cracking. In comparison to the local out-of-plane failure by bending, failure by cracking is called a global in-plane failure [21]. In this work, two different approaches for determining the cracking criterion are used

and described. First, the approach described by Lu et al. [21] for an ice floe based on a Winkler-type foundation is used, as described in Section 4.2.1. This is then compared to the approach of a mode I breaking failure with fracture toughness as the cracking criterion. Three different load cases to compute the fracture toughness concerning the scale effects of different ice floe sizes are introduced in Section 4.2.2.

4.2.1. Tensile Capacity as Breaking Criterion

As described in Section 4.1, the Winkler-type foundation is a possibility to model the influence of the water surrounding the ice floe. This influence can not be neglected for the cracking forces either. Using the crushing force F_c and the friction force F_f described in Equations (7) and (8), the horizontal force F_h equals to the tensile force

$$F_t = F_c \sin(\psi) + F_f \cos(\psi) \tag{12}$$

as described in Equation (10). The horizontal force then is the relevant force component regarding the cracking failure.

The tensile strength of sea ice in this first approach is set to

$$\sigma_t = 4.278\nu_t(-0.6455)\,\mathrm{MPa} \tag{13}$$

with the total porosity of sea ice $\nu_t = 50\mathrm{ppt}$ [10]. The tensile capacity of the ice floe P_t is calculated to

$$P_t = \sigma_t h l$$

with σ_t following from Equation (13), the ice thickness h and the length of the ice floe l. Cracking occurs, if the tensile force F_t described in Equation (12) fulfills the condition

$$F_t \geq P_t. \tag{14}$$

In the following, three other approaches using the tensile strength instead of the tensile force capacity of the ice floe as a relevant input parameter are shown.

4.2.2. Stress-Intensity Factor as Breaking Criterion

Dempsey et al. [28] described a method to deal with the scale effects of differently sized ice floes during cracking. Three kinds of breaking failure are described in continuum mechanics. Mode I describes the crack opening symmetrically to the xy-plane, as shown in Figure 9. Mode II is used for anti-symmetrically crack opening to the xy-plane and mode III is the separation tangential to the crack front [41]. Assuming a mode I fracture failure, the tensile strength of the ice floe can be estimated using different size effect laws. For the ice cracking at the tip of the bow, mode I is used. The ice is assumed to fail under plane stress conditions. Therefore, the stress in the z-direction is set to $\sigma_z = 0$. In general terms, the stress in the crack tip near-field can be described using [41]

$$\begin{pmatrix} \sigma_x \\ \sigma_y \\ \tau_{xy} \end{pmatrix} = \frac{K_I}{\sqrt{2\pi r}} \cos\left(\frac{\theta}{2}\right) \begin{pmatrix} 1 - \sin\left(\frac{\theta}{2}\right)\sin\left(\frac{3\theta}{2}\right) \\ 1 + \sin\left(\frac{\theta}{2}\right)\sin\left(\frac{3\theta}{2}\right) \\ \sin\left(\frac{\theta}{2}\right)\cos\left(\frac{3\theta}{2}\right) \end{pmatrix}$$

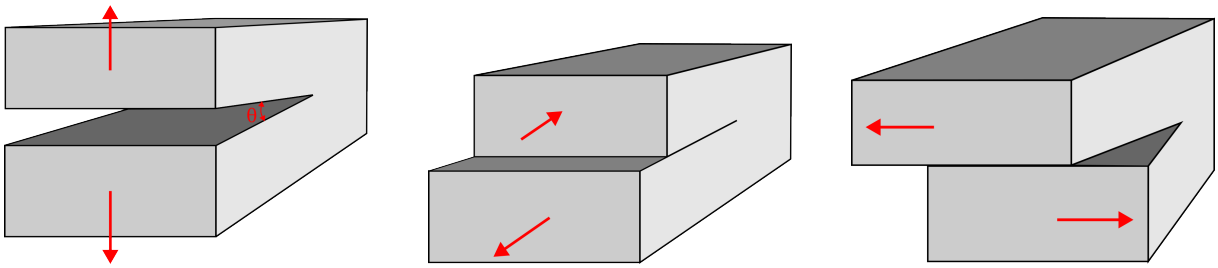

(a) Mode I (b) Mode II (c) Mode III

Figure 9: The different ice fracture modes [41]

with the stress intensity factor for mode I K_I, the crack opening angle θ as depicted in Figure 9a and the stress components σ_x, σ_y and τ_{xy}. For larger distances from the crack tip, the stress and strain formulation simplify to

$$\begin{pmatrix} \sigma_x \\ \sigma_y \\ \tau_{xy} \end{pmatrix} = \begin{pmatrix} \sigma_T \\ 0 \\ 0 \end{pmatrix}$$

with the constant transversal stress σ_T.

Due to the scale effects of ice floes of different sizes, the stress at the crack tip varies with changing floe size without linearity with respect to the scaling factor of floe size. Regarding these scaling effects, different size effect laws based on the law

$$\sigma_n^t = \frac{\Sigma}{\left(1 + \frac{L}{B}\right)^{\frac{1}{2}}} \text{ (BZ)} \tag{15}$$

proposed by Bažant et al. [26] were developed. Dempsey et al. [28] provide values for the constants Σ, L and B for different ranges of floe diameter. Bažant and Pfeiffer [27] introduced two of these additional size effect laws:

$$\sigma_n^t = \frac{\Sigma}{\left(1 + \frac{L}{B} + \frac{C}{L}\right)^{\frac{1}{2}}} \text{ (BZ1)} \tag{16}$$

$$\sigma_n^t = \frac{\Sigma}{\left(1 + \left(\frac{L}{B}\right)^F\right)^{\frac{1}{2}F}} \text{ (BZ2)} \tag{17}$$

The first one is made for smaller floe sizes, the latter one is optimized for larger floe sizes and therefore a failure using linear elastic fracture mechanics (LEFM). In this work, the parameter set for floe size between 0.5 m and 80 m is used. The parameters for the diameter range used in this work are shown in Table 3. The value of F for the law BZ2 is changed in comparison to the values given by Dempsey et al. from 466 to 4.66: Chosing $F = 466$ leads to a dimishing stress σ_n^t, which causes the calculation to crash. Dempsey et al. [28] name also the constants for the floe diameter ranges 0.1 m to 80 m and 0.1 m to 3 m. In the first range, the parameter F is chosen to 1.5, in the latter one 1.9. This leads to the conclusion, that a parameter of $F = 466$ does not only lead to errors in terms of

Table 3: Constants for different scale-effect laws for floes within diameter range 0.5 m – 80 m [28]; value F for BZ2 changed in comparison to [28].

Law	Σ	B	C	F
BZ	0.68	0.26		
BZ1	2.4	0.02	5.85	
BZ2	0.38	0.71		4.66

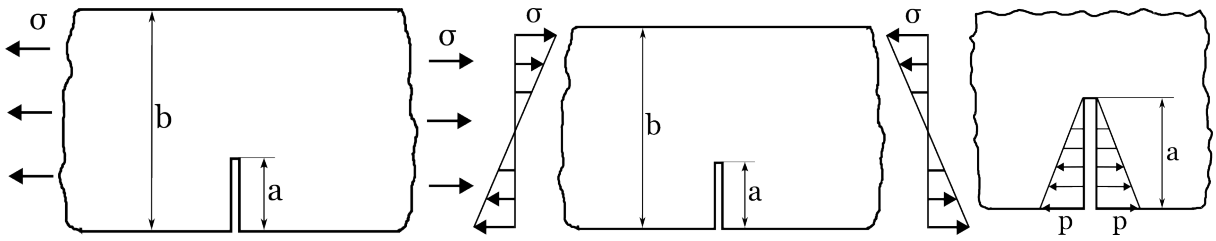

(a) pure tensile stress (b) pure flexural stress (c) linear crack face loading

Figure 10: Different loading scenarios for ice cracking with the crack length a and the floe length b [41].

mathematic, but also in terms of content. Chosing the parameter $F = 4.66$, the computed stress σ_n^t is in a similar order of magnitude as for the other floe size ranges.

As a dimension for the stress especially in the near field, the stress-intensity factor K_I is used. Using the stress-intensity factor, the fracture criterion can be expressed by

$$K_I = K_{Ic}, \tag{18}$$

where K_{Ic} is the material-specific critical stress-intensity factor, also called fracture toughness. Typical values for K_{Ic} are given in Table 4. For modes II and III a similar condition like Equation (18) holds. The K-factor for mode I for an edge crack with a linear crack face loading p can be calculated by [41]

$$K_I = 0.439p\sqrt{\pi a}$$

with the crack length a as indicated in Figure 10c. For an edge crack at mode I with pure tensile stress as shown in Figure 10a, the K-factor is calculated as [41]

$$K_I = \sigma\sqrt{\pi a}\sqrt{\frac{2b}{\pi a}\tan\left(\frac{\pi a}{2b}\right)}G_I\left(\frac{a}{b}\right) \tag{19}$$

with

$$G_I(\epsilon) = \frac{0.923 + 0.199\left(1 - \sin\left(\frac{\pi}{2}\epsilon\right)\right)^4}{\cos\left(\frac{\pi}{2}\epsilon\right)}$$

and the crack length a, the floe length b and the stress σ acting on the floe, as depicted in Figure 10. For the same crack with pure flexural stress shown in Figure 10b, Equation (19) holds with

$$G_I(\epsilon) = \frac{0.752 + 2.02\epsilon + 0.37\left(1 - \sin\left(\frac{\pi}{2}\epsilon\right)\right)^4}{\cos\left(\frac{\pi}{2}\epsilon\right)}.$$

Determining the fracture toughness of sea ice was the topic of multiple research projects in the past. Liu et al. [42] investigate the fracture toughness of freshwater ice under different loading rates and varying temperatures. For a loading rate of $v = 1\frac{\text{mm}}{\text{s}}$ and temperatures between $-30°C$ and $-10°C$, the mean fracture toughness is around $K_{Ic} = 230\,\text{kN}\,\text{m}^{-3/2}$. Fischer et al. [43] name a mean value of $K_{Ic} = 145.7\,\text{kN}\,\text{m}^{-3/2}$ at temperature $-15°C$ for the quasi-static case of freshwater granular laboratory-made ice. Cristmann et al. [44] determine the fracture toughness of Antarctic freshwater glacier ice with a similar density as first-year sea ice in the range of $K_{Ic} = 60, \ldots, 140\,\text{kN}\,\text{m}^{-3/2}$ with a mean value around $K_{Ic} = 120\,\text{kN}\,\text{m}^{-3/2}$. Since the most important factor of the fracture toughness of ice is the porosity of the ice, which is directly included in the density, these values can also be used for the first-year sea ice in this work. Dempsey et al. [45] describe the fracture energy G_c and the short-term elasticity modulus E for three different measurements in antarctic sea ice. With the formulation $K_{Ic} = \sqrt{G_c E}$, the resulting fracture toughness is $K_{Ic} = \{177.820, 180.222, 215.034\}\,\text{kN}\,\text{m}^{-3/2}$.

All compared values for the fracture toughness are in a similar range. In this work, three different values for fracture toughness are compared during the simulation. Since the values given by Dempsey et al. are all between the values given by Liu et al. and Fischer et al., these values can be regarded as upper and lower bounds for the value range described by Dempsey et al. Therefore, these values are not used during the parameter study described in Section 5.3. The results are shown in Section 5.3.1. All values of the fracture toughness are summed up in Table 4.

Table 4: Comparison of different values of the fracture toughness

Author	**Density**	**Loading rate**	**Temperature**	**K_{Ic}**
Liu	-[1]	$1\,\frac{\text{mm}}{\text{s}}$	$-30\,°\text{C}$ to $-10\,°\text{C}$	$230\,\text{kN}\,\text{m}^{-3/2}$
Fischer	$891\,\frac{\text{kg}}{\text{m}^3}$	-[1]	$-15\,°\text{C}$	$145.7\,\text{kN}\,\text{m}^{-3/2}$
Christmann	(840 to 870) $\frac{\text{kg}}{\text{m}^3}$	-[1]	$-15\,°\text{C}$	$120\,\text{kN}\,\text{m}^{-3/2}$
Dempsey[2]	-[1]	-[1]	-[1]	$180.222\,\text{kN}\,\text{m}^{-3/2}$

[1] No value given
[2] Not used in this work; listed only for comparability

4.2.3. Cracking Line Determination

The cracking line is assumed to tend orthogonal to the bow shape at the ice interaction zone. Lu et al. [21] described radial cracking as a global failure with an orthogonal cracking direction with respect to the tangent at the bow section. If the floe is big enough, additional cracks with angles between 30° and 45° occur left and right of the

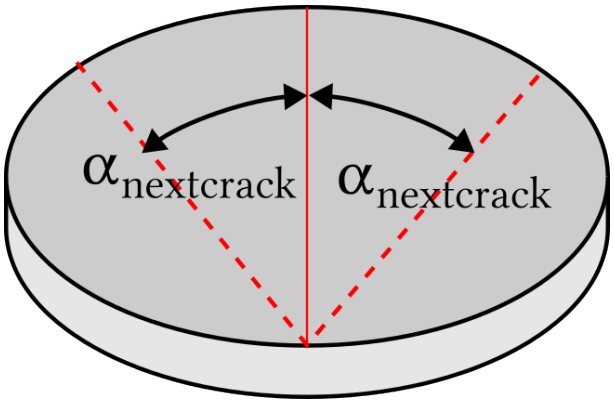

Figure 11: Possible cracking lines of the ice floe. If the floe is big enough to be cracked more than once, the additional cracking lines (dashed) are used too.

straightforward crack. In this work, the initial crack of a floe is always orthogonal to the current bow section. If the remaining floes are again classified as cracking failure, the cracking line is rotated by $\alpha_{\text{nextcrack}} = 30°$, as shown in Figure 11.

The direction of the cracking line is based on the normal vectors of the bow at the nodes of the bow contour. These normal vectors are calculated using

$$\mathbf{n}_{\text{bow},i} = \begin{pmatrix} y_{\text{bow},i-1} - y_{\text{bow},i+1} \\ x_{\text{bow},i+1} - x_{\text{bow},i-1} \end{pmatrix}, \tag{20}$$

with $x_{\text{bow},i}$ and $y_{\text{bow},i}$ indicating the nodes of the bow for $i \in \mathbb{N}_0 \wedge i \leq n$ with n beeing the number of bow nodes. Equation (20) is then normalized to length 1 and, if necessary, multiplied by -1 such that the normal vector points outwards of the bow.

If cracking started once, it is assumed to continue until the end of the floe. The main assumption made in this case is the homogeneity of the ice floe, especially with no existing dislocations in the ice grain structure.

4.3. Local Cracking

In icebreaking processes, the ice floes are not only broken at the tip of the bow but also at the bow side and the shoulder. Besides the failure by bending, the bent floes fail by cracking in this area too. The reason for this cracking is not the splitting by the bow tip, but the shear and local bending forces due to the hull shape and the acting buoyancy forces [46, 47]. Since the simulation in this work is done in two dimensions with a third, parametrized dimension, the ice breaking due to the hull contour is not modelled in a fully three-dimensional case, but the breaking pattern is described in the two-dimensional surface. Therefore, a new formulation of cracking is invented. In comparison to classical cracking, the new kind of cracking is not a global failure, but a local one. It starts as a cracking failure and ends as a bending failure. The resulting breaking pattern is described by Ettema et al. [47]. Following them, the ice cusps created by bending are then broken by a failure line starting orthogonal to the bow, but then turning towards the stern instead of separating the floe directly. In this work, this kind of cracking is called *local cracking*.

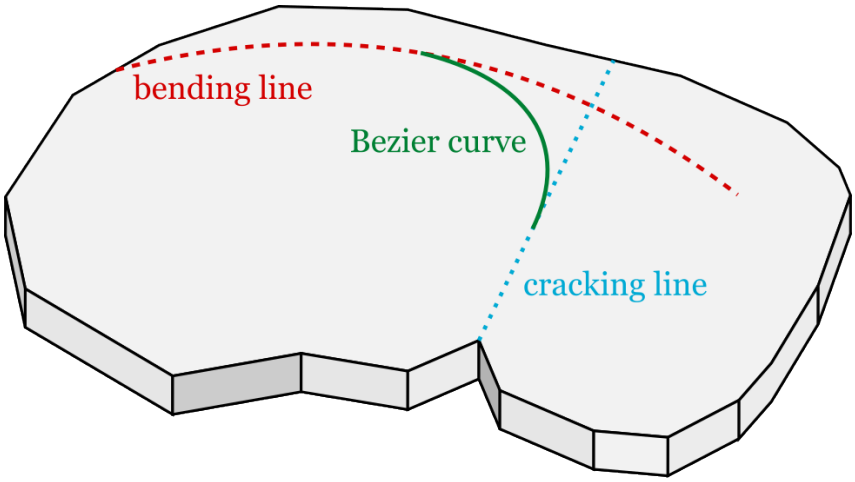

Figure 12: Concatenation of the breaking line for local cracking. The cracking line (blue, dotted) and the bending line (red, dashed) are linked by a Bezier curve (green, solid).

4.3.1. Cracking Criterion

As the cracking condition of the local cracking, the same condition as the one of the bending failure holds. As described in Section 4.1, Equation (11) holds. This cracking criterion is chosen since the failure ends as bending and therefore, the floe must be able to bend. The initial cracking can occur already with a lower load because the tensile capacity of ice is lower than the bending capacity. Therefore, the cracking condition is always fulfilled if the bending condition is fulfilled.

4.3.2. Cracking Line Determination

In the first part, the cracking line is dominated by the cracking component of the breaking process. The last part is then dominated by the bending component. In between, these two parts are connected. Therefore, the cracking line is separated into three parts, as shown in Figure 12. The first part consists of a pure cracking line, as described in Section 4.2 and is named $\mathcal{C}_{\text{crack}}$. To get the last part, the bending line of the floe is computed as described in Section 4.1, here named $\mathcal{C}_{\text{bend}}$. If the bending line is too close to the outside of the floe, the floe edge line is used as the third part of the cracking line. This is equal to a non-existing third part because then no bending in this section takes place. The second part of the cracking line connects the last and the first part using a Bezier-curve $\mathcal{C}_{\text{Bezier}}$ defined by the nodes $\mathbf{n}_{\text{Bezier}}$. These nodes can be structured in three kinds:

$$\mathbf{n}_{\text{Bezier}} = \left[\mathbf{n}_{\text{Bezier0}}, \mathbf{n}_{\text{Bezier1}}, \mathbf{n}_{\text{Bezier2}}\right]. \tag{21}$$

The first element, $\mathbf{n}_{\text{Bezier0}}$, contains the last point used of the pure cracking segment x_{crack}, which is determined by

$$\mathbf{n}_{\text{Bezier0}} = \mathbf{x}_{\text{crack}}(i_{\text{lastCrack}}) \quad s.t. \min_{i_{\text{lastCrack}}} \text{dist}\left(\mathbf{x}_{\text{crack}}(i_{\text{lastCrack}}), \mathbf{x}_{\text{int}}\right)$$

with $\mathbf{x}_{\text{int}}$ being the frontmost intersection point between the bow and the ice floe. The second element, $\mathbf{n}_{\text{Bezier1}}$, is the intersection point $\mathbf{x}_{\text{int,Bezier}}$ between the pure cracking line and the pure bending line. In contrast to the first two elements, the third element, $\mathbf{n}_{\text{Bezier2}}$, can contain multiple points of the pure bending line. The pure bending line $\mathcal{C}_{\text{bend}}$ is orientated, such that the first point is the nearest one to the bow and the last one is the nearest one to the stern. Starting at the first point of $\mathcal{C}_{\text{bend}}$ after the intersection point $\mathbf{x}_{\text{int,Bezier}}$ with the index n_0, $\mathbf{n}_{\text{Bezier2}}$ contains all points of the pure bending line that have the same or a lower distance dist_m to the intersection point $\mathbf{x}_{\text{int,Bezier}}$ as the point used of the pure cracking curve $\mathbf{n}_{\text{Bezier0}}$:

$$\mathbf{n}_{\text{Bezier2},i} = \mathcal{C}_{\text{bend},i};\ i \in \mathbb{N} \cup [n_0, n]$$

with

$$n = \max_{i \in \mathbb{N}_0} \left(\text{dist}\left(\mathcal{C}_{\text{bend},i}, \mathbf{x}_{\text{int,Bezier}} \right) \leq \text{dist}_m \right).$$

The Bezier curve $\mathcal{C}_{\text{Bezier}}$ is then calculated using the nodes concatenated with Equation (21). The final failure curve for the local cracking consists of

$$\mathcal{C}_{\text{local}} = \{\mathcal{C}_{\text{crack,local}}, \mathcal{C}_{\text{Bezier}}, \mathcal{C}_{\text{bend,local}}\}$$

with

$$\mathcal{C}_{\text{crack,local},i} = \mathcal{C}_{\text{crack},i},\ \forall i < m, i \in \mathbb{N}$$

and

$$\mathcal{C}_{\text{bend,local},i-(n+1)} = \mathcal{C}_{\text{bend},i},\ \forall i > n, i \in \mathbb{N}.$$

with the index of the last used cracking line point m and the index of the first used bending line point n.

4.4. Direct Rotation

If a floe is sufficiently small, it will neither fail by bending nor by cracking. Instead, it will fail by direct rotation [21]. If the size is below the lower bound required for the thin plate theory, the floe is handled as an unbreakable floe. The important value for the thin plate theory is the length of the ice floe l. If $l \geq \ell$ with ℓ being the characteristic length of the ice floe, the floe can be handled as a thin plate. Another more conservative threshold invented by Lu et al. [20] is $l \geq 2\ell$. This more conservative threshold is used in this work for floes that are originally classified as failure by cracking, but no initial cracking takes place due to the position of the floe at the bow and the shape of the floe.

The ice floe is flipped if the vertical force acting on the floe results in a momentum around an imagined axis inside the floe. Different parameters influence this momentum: The vertical force due to the ship–ice contact itself, the shape of the ice floe, the thickness of the ice floe and – as a result of the latter two parameters – the buoyancy force of the floe. In the simulation, two different types of floes fail by direct rotation. In addition to the case of sufficiently small floes mentioned above, a second case occurs for floes that are classified as cracking failure in the back of the bow near the shoulder. If a floe with bow contact in the back part has no initial crack or edges, which leads to a higher stress concentration, no cracking will take place. Instead, it will be flipped.

5. Validation of the Ship–Ice Interaction

To validate the developed icebreaking simulation, different approaches are used: First, in Section 5.1, the developed icebreaking simulation is used for two different icebreaking vessels: The PSRV S.A. Agulhas II which is already used in the previous chapters and the German icebreaking research vessel RV Polarstern. The resulting crushing forces for bending failure are then compared to those computed by the icebreaking simulation for bending failure of level ice by Erceg et al. [8]. The crushing forces are, in combination with the bending capacity, the major criterion for failure by bending. The results are then compared to the crushing forces computed for both vessels using the simulation developed in this work.

Afterwards, in Section 5.2, the breaking pattern is analysed systematically for different positions relative to the bow. Different floe diameters and thickness values are validated using the breaking patterns described in different research works.

Finally, the influence of different physical and simulation parameters is analysed in Section 5.3.

5.1. Comparison of Forces

The crushing forces that occur during the bending of ice floes applying the simulation developed in this work on the PSRV S.A. Agulhas II with thickness $h = 1.0\,\mathrm{m}$ are mainly in the range of

$$F_c = [0\,\mathrm{kN}, 2500\,\mathrm{kN}].$$

Erceg et al. [8] determined for RV Polarstern the maximal crushing forces at the forward bow section at ice thickness $h = 1.0\,\mathrm{m}$ values above $F_c^{\max} = 6000\,\mathrm{kN}$, with most of the forces below $F_c = 3000\,\mathrm{kN}$. The probability densities of the occurring forces are shown in Figure 13. The stem angle of the RV Polarstern is $\psi_{\mathrm{PS}} = 45°$, whereas the PSRV S.A. Agulhas II has a stem angle of $\psi_{\mathrm{AGU}} = 63°$ according to the design drawings. The larger the stem angle value is, the higher the vertical component of the crushing force. This component is relevant to create bending failures. It has to be noted that the RV Polarstern is an icebreaking vessel of the ice class GL-Arc3 (corresponding to polar class PC2 [48]), whereas the PSRV S.A. Agulhas II is a PC5 icebreaker. Therefore, RV Polarstern is a more capable icebreaker that can break multi-year ice, whereas the PSRV S.A. Agulhas II mostly operates in first-year ice. Due to the expected different ice conditions, the values named for the RV Polarstern can be assumed to be upper boundary values for the values computed for the PSRV S.A. Agulhas II. Some of the force values calculated for the PSRV S.A. Agulhas II in this work are unexpectedly high. This may be caused by numerical errors and the division of the ice pressure by very small contact areas.

Additionally to the comparison of the values for the RV Polarstern given by [8], the MATLAB-Code developed by Erceg et al. [8] is used to compare the breaking resistance forces of the PSRV S.A. Agulhas II for bending with the forces occurring for bending and cracking in this work. The crushing forces values are up to $F_{c,\mathrm{avg}} = 5000\,\mathrm{kN}$. This

corresponds to the crushing forces computed in this work, under the assumption that the high values with low probability density are caused by numerical errors and not by physical simulation results. Another possible reason for the force peaks at the bow may be due to the calculation formula of the crushing area. The same peaks can be found in the resulting crushing forces shown by Erceg et al. [8] since the same determination method for the crushing area is used. The crushing area is calculated using Equation (6). This equation is valid for horizontal intersection areas A_h, which can be approximately assumed to be rectangular. This is because the crushing area A_c is assumed to be rectangular. Due to the non-linearity of the sinus function, an arbitrarily shaped horizontal intersection area can not be transformed properly to a rectangular intersection area. This error gets amplified for small bow angle values ψ and therefore unbounded large values of $\frac{1}{\sin(\psi)}$.

Besides the first peak of crushing forces simulated using the level ice simulation developed by Erceg et al. the probability density values of the crushing force in the case of bending computed by the simulation developed in this work agree well with those for the application of the simulation tool developed by Erceg et al. on the *S.A. Agulhas*. Additionally, the crushing forces computed and validated for the RV Polarstern [8] are compared. As shown in Figure 13, the general distributions of the crushing forces are similar for the simulation results of both the PSRV S.A. Agulhas II and the RV Polarstern. The mean crushing force applying the simulation tool on the PSRV S.A. Agulhas II are slightly smaller than those of the RV Polarstern. This is explainable by the different ice classes of the vessels. Compared to the results by Erceg et al. [8], the distribution for the RV Polarstern has minor qualitative differences, although the agreement with the field observation data by Hoffmann [1] is pretty good, apart from for the small crushing forces $F_c \leq 200\,\text{kN}$.

In this work, the icebreaking of floe ice is simulated, whereas Erceg et al. simulate the icebreaking of level ice. Because of the arbitrary positions of the ice floes, ice contact near the shoulder occurs more often in comparison to the level ice simulation by Erceg et al. This results in more and probably higher load peaks at the bow. The lack in accordance for small crushing force probability densities can be based on the different ice scenarios simulated.

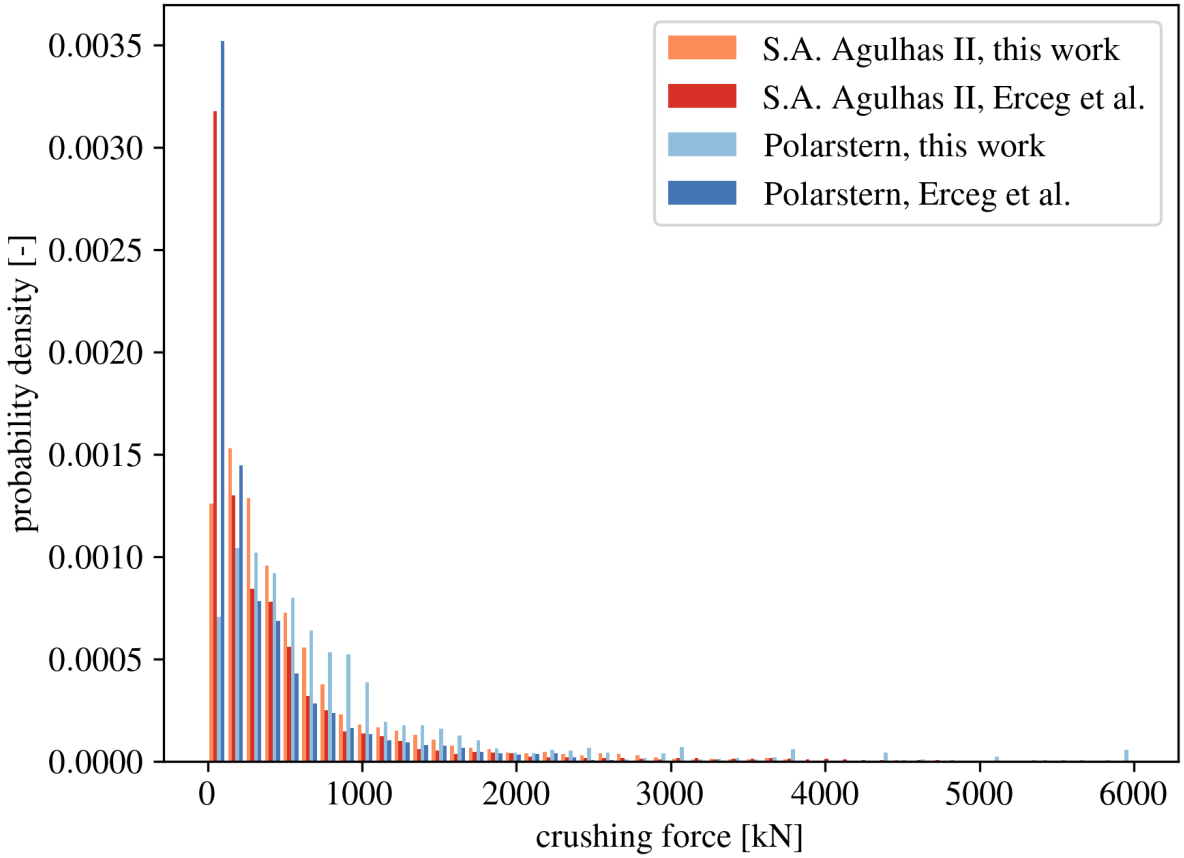

Figure 13: Crushing force spectrum of the bending failures for ice thickness $h = 1.0\,\mathrm{m}$ resulting from this work and from the simulation by Erceg et al. (pure bending).

5.2. Validation Strategy for the Breaking Pattern

During this work, the created simulation is validated against the breaking pattern observed by Puntigliano [46] and Ettema et al. [47] in model scale tests. This is done for both floe fields and single floes. As shown in Figure 14, the single floes are placed systematically for different floe sizes at five positions each:

a) near the shoulder on the port side

b) between the bow tip and shoulder on the port side

c) near the shoulder on the starboard side

d) between the bow tip and shoulder on the starboard side

e) midship in front of the bow

for every diameter of the diameter set

$$D \in \{10\,\mathrm{m}, 20\,\mathrm{m}, 30\,\mathrm{m}\}$$

and every ice thickness of the thickness set

$$h \in \{0.8\,\mathrm{m}, 1.0\,\mathrm{m}, 1.2\,\mathrm{m}\}.$$

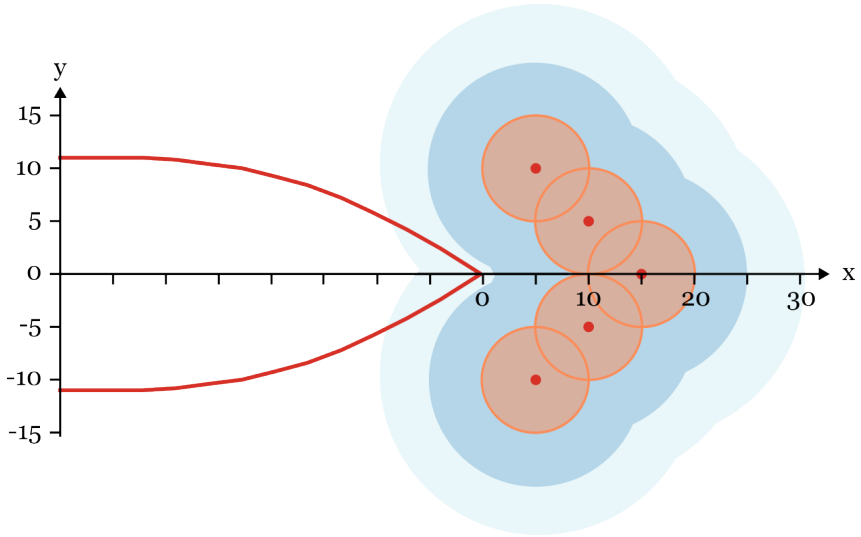

Figure 14: Positions of the single ice floes for testing relative to the initial position of the bow. At every position, different diameters ($d = \{10, 20, 30\}$ m) and ice thickness values are simulated. If initial bow contact occurs, the floe is shifted in the x-direction.

Using this procedure, the simulation can be tested for a large number of different ice scenarios. The breaking pattern for the different scenarios is exemplarily shown in Figure 15 for floes with diameter $D = 10\,\mathrm{m}$ and thickness $h = 0.8\,\mathrm{m}$ and in Figure 16

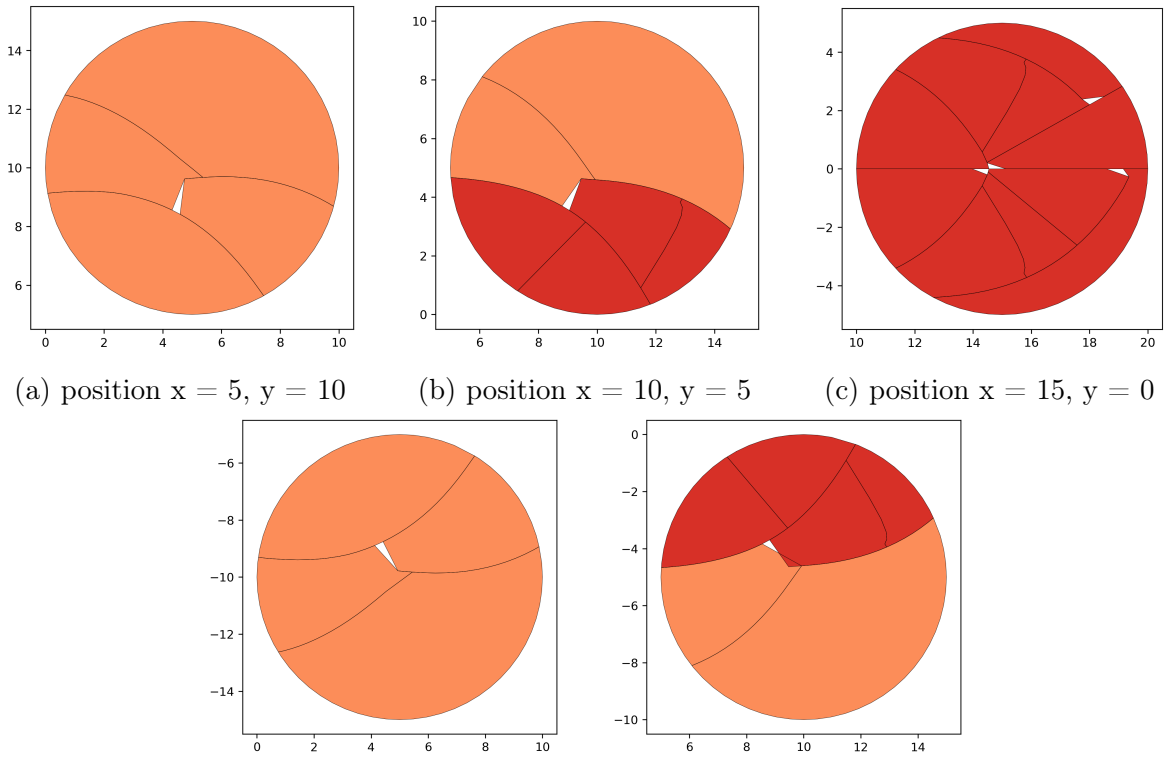

(a) position x = 5, y = 10 (b) position x = 10, y = 5 (c) position x = 15, y = 0

(d) position x = 5, y = -10 (e) position x = 10, y = -5

Figure 15: Breaking pattern of floes with 10 m diameter and 0.8 m thickness. The position values are given in m. Orange floes are flipped and are assumed to stay outside the bow and red floes are cracked until they are unbreakable due to their size and then handed to the propeller.

for floes with diameter $D = 20\,\text{m}$ and thickness $h = 1.0\,\text{m}$. Especially for the floes with diameter $D = 20\,\text{m}$, the same fan-shaped breaking pattern as observed by Puntigliano [46] and Ettema et al. [47] occurs. Even at the smaller floes, this breaking pattern is visible, although it is not as distinctive due to the small size of the floes and therefore the limited number of cusps. The slight differences in the breaking pattern for port and starboard are due to the discretization of the bow and numerical inaccuracy during the simulation.

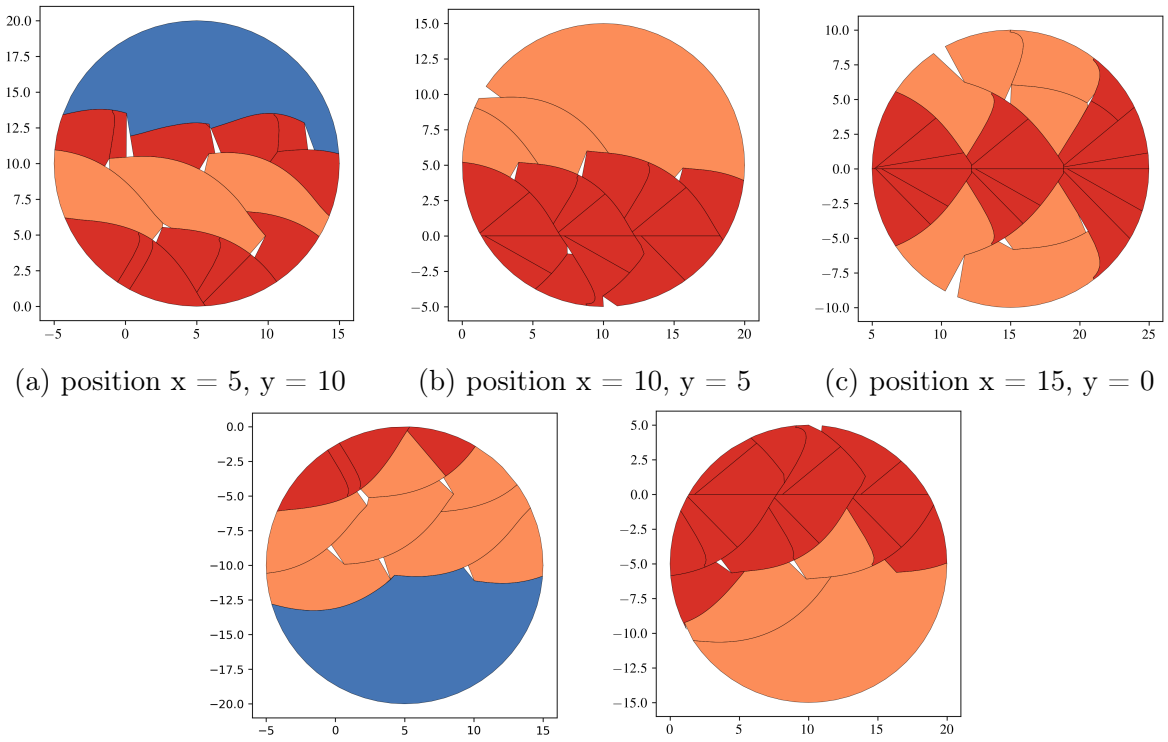

(a) position x = 5, y = 10 (b) position x = 10, y = 5 (c) position x = 15, y = 0

(d) position x = 5, y = -10 (e) position x = 10, y = -5

Figure 16: Breaking pattern of floes with 20 m diameter and 1 m thickness. The position values are given in m. Blue floes are not changed, orange floes are flipped and are assumed to stay outside the bow and red floes are cracked until they are unbreakable due to their size and then handed to the propeller.

5.3. Parameter Studies

To validate the simulation and determine the influence of different physical and simulation parameters, different parameter studies are conducted. The analysed parameters are the fracture toughness in Section 5.3.1, the breaking mode in case of failure by cracking in Section 5.3.2, the ice thickness in Section 5.3.3 and the scale effect law in Section 5.3.4. As a reference case, the following parameter combination is used: Fracture toughness $K_{Ic} = 145.7\,\mathrm{kN\,m^{-3/2}}$, breaking due to pure tensile stress, ice thickness $h = 1.0\,\mathrm{m}$ and scale effect law by Bažant indicated as BZ. The results of the parameter study are summed up in Section 5.3.5.

5.3.1. Fracture Toughness

The fracture toughness depends on the density, the brine concentration and the temperature of the ice as well as the contact velocity between the ship and the ice [43, 10]. To determine the influence of the fracture toughness on the calculated breaking pattern and cusp sizes during the simulation, different values of the fracture toughness are compared within the scope of a parameter study. Both the cusp size distribution and the breaking pattern are compared for the different fracture toughness values K_{Ic} shown in Table 5.

The fracture toughness is used for all stress-based cracking criteria. Another cracking criterion used in this work is a force-based criterion, which is not dependent on the fracture toughness and hence not considered in this section. Therefore, different fracture toughness values are compared for three different cracking criteria: pure tensile stress, pure flexural stress and linear crack face loading.

Figure 17 shows the cusp volumes of the breaking simulation of all four floe fields shown in Figure 1 for a cracking failure due to tensile stress. As one can see in Figure 18 the width of the cracked floes is larger for larger values of the fracture toughness K_{Ic}. This is explainable by the higher resistance against cracking of the floes due to higher fracture toughness. On the other hand, a higher value of fracture toughness leads to a stiffer, more brittle material, which leads to smaller fragments. This can also be seen in Figure 18, since the ice cusps are shorter for increasing K_{Ic}. This results in more compact fragments, which is the expected behaviour for a brittle material.

Besides the smaller fragments due to cracking, larger already bent floes fail by direct rotation for increasing values of K_{Ic}. Because the brittle material properties are only respected in cracking, but not in bending failure, the bending shape does not change. Due to the increased resistance against cracking for higher values of fracture toughness, a higher initial contact force and higher tensile stress are needed to initiate cracking. This contact force is not always applicable and some floes remain as they are and fail by direct rotation.

Since the implemented failure criterion for failure by bending does not depend on the fracture toughness, the bending failure occurs also in load situations for higher fracture toughness values whereas for lower fracture toughness values, cracking occurs. Therefore, the cusp volume is not larger in total for higher fracture toughness values. This is shown by the mean cusp volumes, which decrease slightly with increasing fracture toughness. The exact values are shown in Table 5, the reference configuration is marked in light blue.

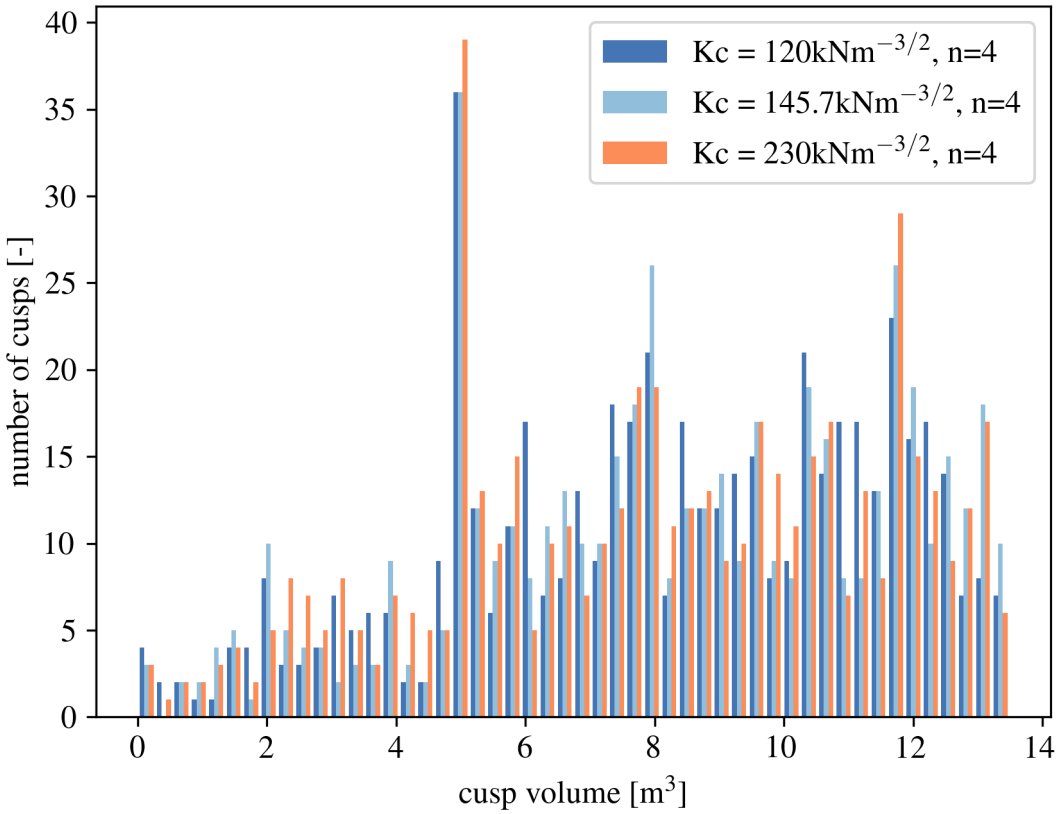

Figure 17: Cusp volume spectrum for varying the fracture toughness K_{Ic} at scale effect law BZ, ice thickness $h = 1.0\,\mathrm{m}$ and cracking due to pure tensile stress.

Table 5: Mean values of cusp volume $\bar{V}_{\text{cusp}}$ and the cusp area $\bar{A}_{\text{cusp}}$, number of cusps n_{cusp} and floes failed by direct rotation n_{flip}, the total area of the floes failed by direct rotation due to unbreakable size ($A^{\text{tot}}_{\text{cusp}}$) and due to their position at the bow ($A^{\text{tot}}_{\text{flip}}$) for different fracture toughness values averaged over all four floe fields shown in Figure 1. The reference configuration is highlighted in light blue.

K_{Ic}	$\bar{V}_{\text{cusp}}$	$\bar{A}_{\text{cusp}}$	n_{cusp}	n_{flip}	$A^{\text{tot}}_{\text{cusp}}$	$A^{\text{tot}}_{\text{flip}}$
$120\,\text{kN m}^{-3/2}$	$8.16\,\text{m}^3$	$8.16\,\text{m}^2$	129	82	$1053.03\,\text{m}^2$	$2391.07\,\text{m}^2$
$145.7\,\text{kNm}^{-3/2}$	$8.14\,\text{m}^3$	$8.14\,\text{m}^2$	125	83	$1019.48\,\text{m}^2$	$2426.90\,\text{m}^2$
$230\,\text{kN m}^{-3/2}$	$8.05\,\text{m}^3$	$8.05\,\text{m}^2$	127	82	$1024.01\,\text{m}^2$	$2432.66\,\text{m}^2$

Deviating from the mean value of the cusp volume, the distribution of the volumes changes for different fracture toughness values: especially the smaller cusps with a maximal volume of $V^{\text{max}}_{\text{cusp}} = 4\,\text{m}^3$ occurs more often for lower values of the fracture toughness, as shown in the cusp volume distribution in Figure 17. In contrast, for higher values of the fracture toughness, there are slightly more cusps with a volume above $V^{\text{max}}_{\text{cusp}} = 11\,\text{m}^3$. The sum of the total cusp area and the total area of all floes failed by direct rotation $A^{\text{tot}}_{\text{cusp}} + A^{\text{tot}}_{\text{flip}}$ is nearly constant and within the range of 0.4% deviation around the reference parameter combination.

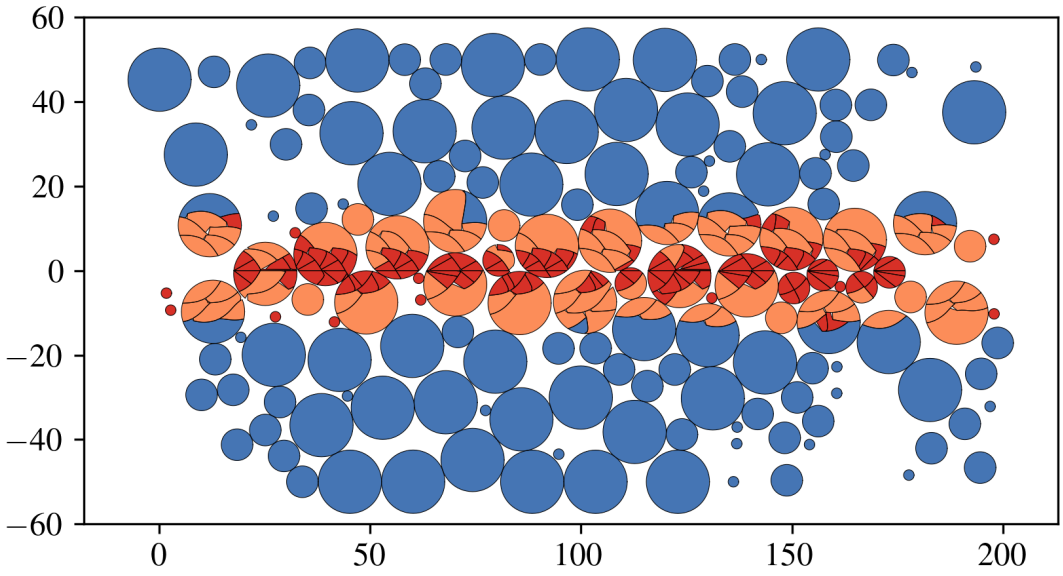

(a) $K_{Ic} = 120\,\mathrm{kN\,m^{-3/2}}$

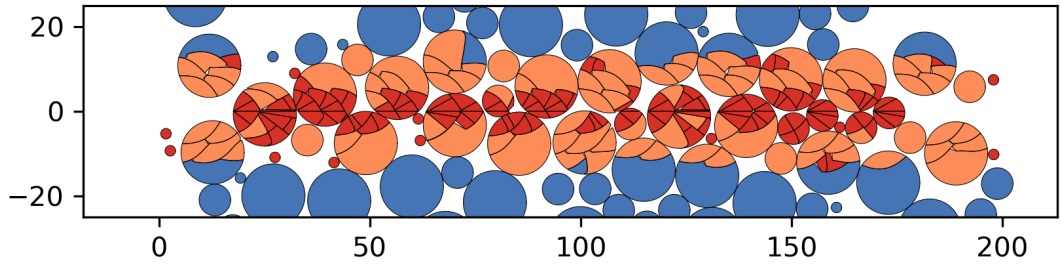

(b) $K_{Ic} = 145.7\,\mathrm{kN\,m^{-3/2}}$

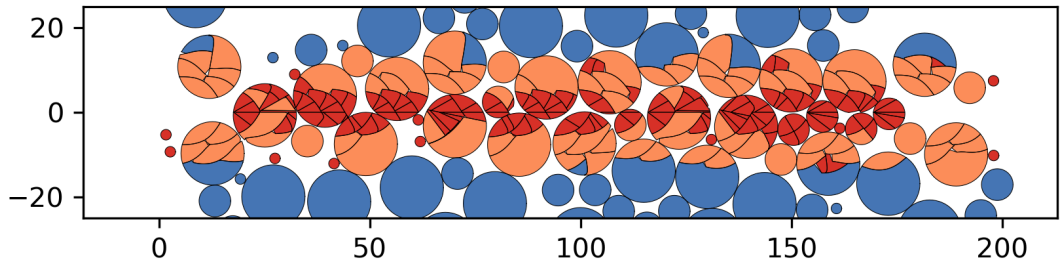

(c) $K_{Ic} = 230\,\mathrm{kN\,m^{-3/2}}$

Figure 18: Breaking pattern for varying fracture toughness K_{Ic} using the ice floe field shown in Figure 1a. Floe properties: $h = 1\,\mathrm{m}$, failure by tensile stress, scale effect law BZ. Blue floes are not changed, orange floes are flipped and are assumed to stay outside the bow and red floes are cracked until they are unbreakable due to their size and then handed to the propeller.

5.3.2. Breaking Mode

Four different breaking modes for failure by cracking are investigated in this work. Three of them are energy-based, namely the cracking criteria due to pure tensile stress, pure flexural stress and the induced cracking energy due to a linear crack face load. In all these cases, the fracture toughness calculated by the fracture energy is used to determine the cracking criterion and thereby to define whether the floe is broken. The fourth cracking criterion is force-based using the horizontal component of the crushing force calculated based on a Winkler-based foundation. This breaking mode is named point load in the following. The resulting breaking patterns in the floe field are shown in Figure 20. Comparing the two stress-based cases shown in Figure 20c for pure tensile stress, which is the reference case, and Figure 20d for pure flexural stress, the latter one leads to a slightly more brittle breaking pattern with again larger floes failed by direct rotation than the first one. The mean cusp volume in case of pure tensile stress is $\bar{V}_{\text{cusp}} = 8.14\,\text{m}^3$, whereas it is $\bar{V}_{\text{cusp}} = 8.04\,\text{m}^3$ with pure flexural stress. In the latter case, slightly fewer cusps are created, because more floes fail by direct rotation.

The point load at the crack faces leads to relatively small cusp sizes, even if more floes fail by direct rotation than for the stress-based cases. This leads to the fact that cracking occurs less frequently, but if it occurs, the cusps are smaller than using the stress-based approaches. Contrariwise, the number of cusps is similar to that of the reference configuration, whereas the number of floes failing by direct rotation is around 4% higher for the point load case than for the tensile stress-based one.

In contrast, the linear crack face load leads to more and slightly bigger cusps in combination with fewer floes failing by direct rotation. In comparison to the tensile stress-based case, 19% more cusps occur for the linear crack face loading. Instead, 7% fewer floes fail by direct rotation. Even if the number of floes diverges for both failure cases, the total area of affected floes $A^{\text{tot}}_{\text{cusp}} + A^{\text{tot}}_{\text{flip}}$ for all parameter configurations is nearly constant with a deviation of less than 0.5% from the reference configuration.

The total distribution of the ice cusp volumes averaged over all four floe fields shown in Figure 1 is shown in Figure 19 and the mean cusp volumes are listed in Table 6.

Table 6: Mean values of cusp volume $\bar{V}_{\text{cusp}}$ and cusp area $\bar{A}_{\text{cusp}}$, number of cusps n_{cusp} and floes failed by direct rotation n_{flip}, the total area of the floes failed by direct rotation due to unbreakable size ($A^{\text{tot}}_{\text{cusp}}$) and due to their position at the bow ($A^{\text{tot}}_{\text{flip}}$) for different breaking modes averaged over all four floe fields shown in Figure 1. The reference configuration is highlighted in light blue.

Breaking Mode	$\bar{V}_{\text{cusp}}$	$\bar{A}_{\text{cusp}}$	n_{cusp}	n_{flip}	$A^{\text{tot}}_{\text{cusp}}$	$A^{\text{tot}}_{\text{flip}}$
point load	$7.84\,\text{m}^3$	$7.84\,\text{m}^2$	125	86	$983.52\,\text{m}^2$	$2464.64\,\text{m}^2$
linear crack face load	$8.24\,\text{m}^3$	$8.24\,\text{m}^2$	149	78	$1233.53\,\text{m}^2$	$2210.96\,\text{m}^2$
pure tensile stress	$8.14\,\text{m}^3$	$8.14\,\text{m}^2$	125	83	$1019.48\,\text{m}^2$	$2426.90\,\text{m}^2$
pure flexural stress	$8.04\,\text{m}^3$	$8.04\,\text{m}^2$	122	84	$983.03\,\text{m}^2$	$2473.95\,\text{m}^2$

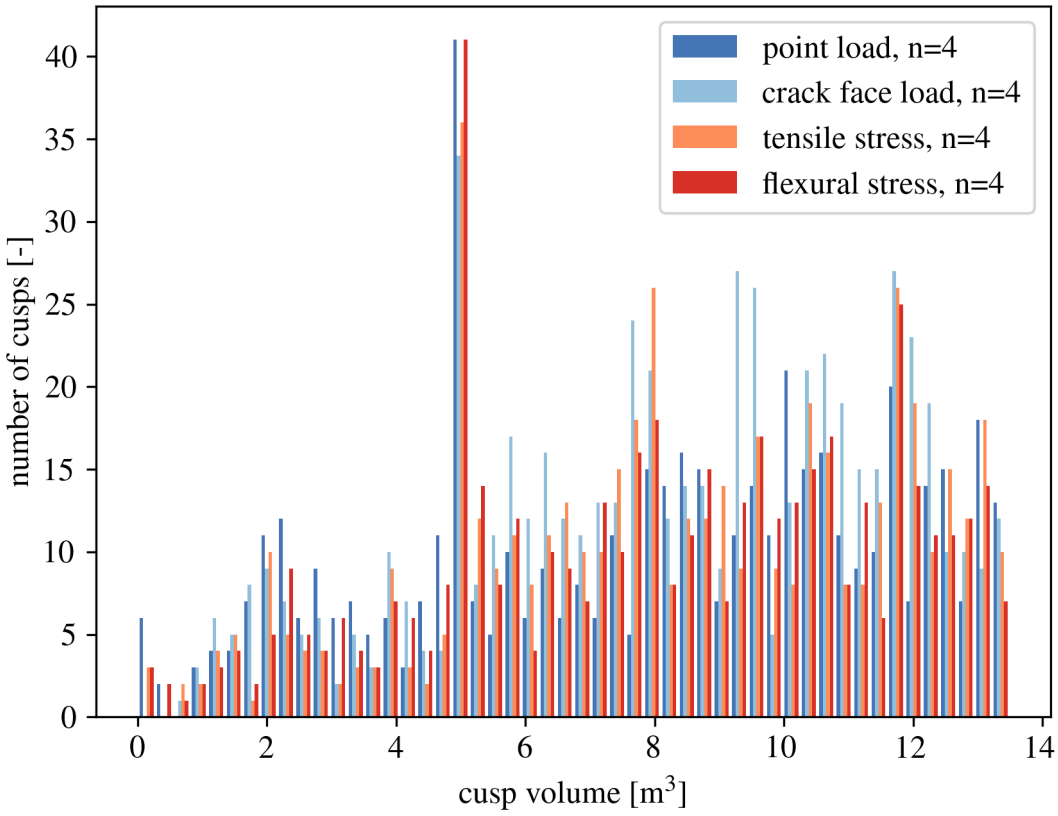

Figure 19: Cusp volume spectrum for varying the breaking mode at fracture toughness $K_{Ic} = 145.7\,\mathrm{kN\,m^{-3/2}}$, scale effect law BZ and ice thickness $h = 1.0\,\mathrm{m}$.

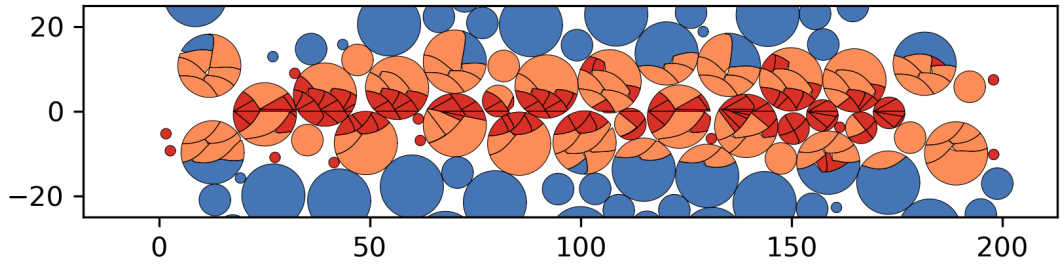

(a) Point load at crack face

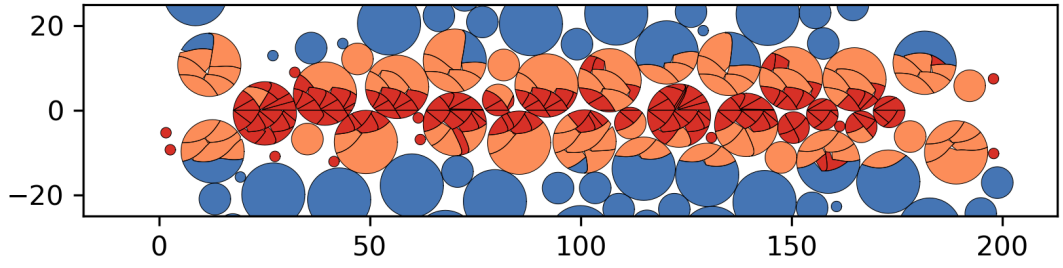

(b) Line load at crack face

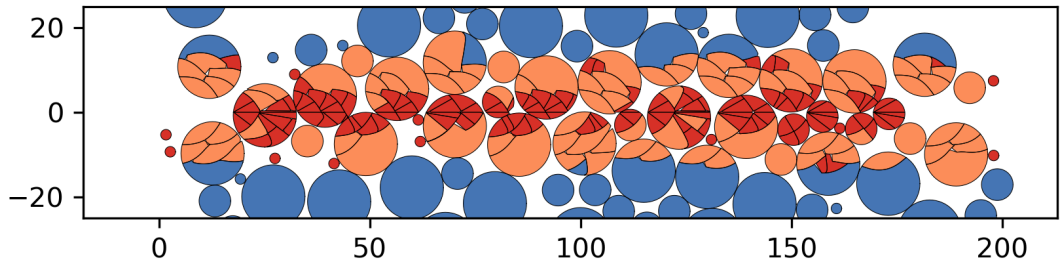

(c) Tensile stress at crack face

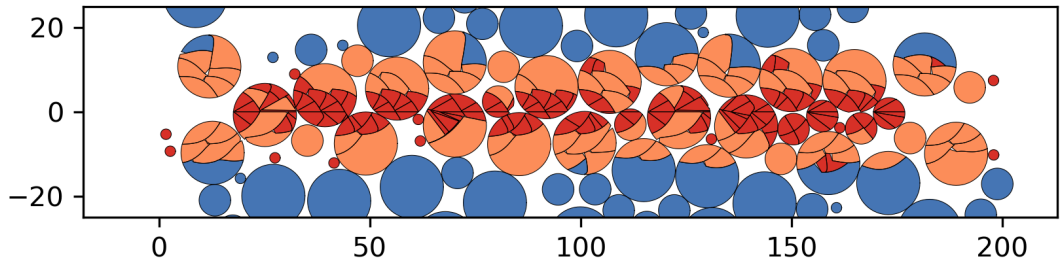

(d) Flexural stress at crack face

Figure 20: Breaking pattern for varying breaking modes using the ice floe field shown in Figure 1a. Floe properties: $h = 1.0\,\mathrm{m}$, $K_{Ic} = 145.7\,\mathrm{kN\,m^{-3/2}}$, scale effect law BZ. Blue floes are not changed, orange floes are flipped and are assumed to stay outside the bow and red floes are cracked until they are unbreakable due to their size and then handed to the propeller.

5.3.3. Ice Thickness

Three different ice thickness values are used in the main part of the simulation:

$$h = \{0.8\,\mathrm{m}, 1.0\,\mathrm{m}, 1.2\,\mathrm{m}\}$$

The main difference in the cusp volume spectrum is the increasing maximal cusp volume for increasing ice thickness. Because of the direct dependency of the characteristic length ℓ on the ice thickness described in Equation (1), the characteristic length shrinks for thinner ice floes. This length determines whether a floe is unbreakable because of its small size. For a larger ice thickness, floes can have a larger area to be unbreakable. Additionally, the floe thickness influences the cusp volume directly, because the cusp area is multiplied by the cusp thickness to determine the cusp volume. In general, thinner floes tend to break in more different cusps than thicker floes. The cracking pattern of small ice floes is quite similar for the different floe thickness values. For larger floes that fail by bending first, the breaking pattern looks different, because the cusps resulting from the bending failure are of different shapes. The mean cusp volumes and additionally the mean cusp areas for better comparison of the breaking pattern are shown in Table 7.

The number of ice cusps is determined by

$$n_{\mathrm{cusp}} = \frac{A^{\mathrm{tot}}_{\mathrm{cusp}}}{\bar{A}_{\mathrm{cusp}}}$$

with the mean area of the ice cusps $\bar{A}_{\mathrm{cusp}}$. Breaking the thinner ice floes of thickness $h = 0.8\,\mathrm{m}$ results in around 29% more ice cusps than for the reference configuration with ice floes of thickness $h = 1.0\,\mathrm{m}$. Ice floes of thickness $h = 1.2\,\mathrm{m}$ produce around 5% less ice cusps than the reference configuration. Unlike in the previously described parameter variations, the total affected area differs for the different ice thickness values. The total area of the floes with thickness $h = 1.0\,\mathrm{m}$ is

$$A^{\mathrm{tot}}_{h=1.0} = A^{\mathrm{tot}}_{\mathrm{cusp},h=1.0} + A^{\mathrm{tot}}_{\mathrm{flip},h=1.0} = 3446.38\,\mathrm{m}^2$$

whereas the total area for thickness $h = 0.8\,\mathrm{m}$ is

$$A^{\mathrm{tot}}_{h=0.8} = A^{\mathrm{tot}}_{\mathrm{cusp},h=0.8} + A^{\mathrm{tot}}_{\mathrm{flip},h=0.8} = 3361.58\,\mathrm{m}^2,$$

which is 2.5% lower than using the reference thickness. The total area for thickness $h = 1.2\,\mathrm{m}$ is with

$$A^{\mathrm{tot}}_{h=1.2} = A^{\mathrm{tot}}_{\mathrm{cusp},h=1.2} + A^{\mathrm{tot}}_{\mathrm{flip},h=1.2} = 3536.22\,\mathrm{m}^2,$$

again around 2.5% higher than for the reference thickness. This results from the higher amount of floes that fail by direct rotation due to their position at the bow. Since the mean cusp size increases with increasing ice thickness and especially because of the increasing characteristic length of the floes, the floes have to be larger to experience failure by bending instead of failure by cracking. If the floe is then more towards the shoulder than the bow tip and no critical edges at the ice edge occur, cracking can not be initiated. Resulting of the combination of larger cusps created by bending and therefore another breaking pattern of the bent cusps, and the different cracking behaviour, more floes fail by direct rotation because of their position, before they are unbreakable because of their size.

Table 7: Mean values of cusp volume $\bar{V}_{\text{cusp}}$ and the cusp area $\bar{A}_{\text{cusp}}$, number of cusps n_{cusp} and floes failed by direct rotation n_{flip}, the total area of the floes failed by direct rotation due to unbreakable size ($A^{\text{tot}}_{\text{cusp}}$) and due to their position at the bow ($A^{\text{tot}}_{\text{flip}}$) for different ice thickness values averaged over all four floe fields shown in Figure 1. The reference configuration is highlighted in light blue.

h	$\bar{V}_{\text{cusp}}$	$\bar{A}_{\text{cusp}}$	n_{cusp}	n_{flip}	$A^{\text{tot}}_{\text{cusp}}$	$A^{\text{tot}}_{\text{flip}}$
0.8 m	5.50 m^3	6.87 m^2	161	95	1110.09 m^2	2251.49 m^2
1.0 m	8.14 m^3	8.14 m^2	125	83	1019.48 m^2	2426.90 m^2
1.2 m	11.21 m^3	9.34 m^2	119	73	1111.99 m^2	2424.23 m^2

Randomized Ice Thickness Additionally, a randomized ice thickness with predefined minimal and maximal values can be used. In this case, the distribution of the thickness h_{rand} is similar to a normal distribution, but with fixed finite minimal and maximal values. It is defined by

$$h_{\text{rand}} = h_{\text{min}} + (h_{\text{max}} - h_{\text{min}}) \frac{1}{p_h} \sum_{i=0}^{p_h} x, \;\; x \in \mathbb{R} \cap [0, 1]$$

with the minimal ice thickness h_{min}, the maximal ice thickness h_{max}, the number of samples n_h and the number of summed-up random numbers p_h. The higher the value of p_h, the smaller the empirical standard deviation of the ice thickness distribution

$$\sigma^{\text{rand}}_{\text{ice}} = \sqrt{\frac{1}{n_h} \Sigma_{i=1}^{n_h} \left(h_i - \bar{h}_{\text{rand}}\right)^2}$$

around the mean value

$$\bar{h}_{\text{rand}} = h_{\text{min}} + (h_{\text{max}} - h_{\text{min}}) \cdot \frac{1}{2}$$

with n_h being the number of samples. The cusp volume distribution for a randomized ice thickness can be found in Figure 21. The distribution is quite similar to those of ice with a thickness of $h = 1.0\,\text{m}$, with slight differences, especially in the boundary areas of the cusp volume distribution. Since the mean value of the randomized ice thickness is $\bar{h}_{\text{rand}} = 1.0\,\text{m}$ and the normal distribution is relatively small with $\sigma^{\text{rand}}_{\text{ice}} = 0.0042\,\text{m}$, the difference between the constant ice thickness $h = 1.0\,\text{m}$ and the randomized ice thickness is small. As shown in Figure 22d, the breaking pattern is also similar to those of the ice floes with constant ice thickness $h = 1.0\,\text{m}$, although some floes fail more similar to the smaller or larger ice thickness values shown. This is the expected breaking pattern since the ice thickness is mainly around the mean value $\bar{h}_{\text{rand}} = 1.0\,\text{m}$, although some ice wedges have ice thickness values that are closer to the boundaries of the randomization interval.

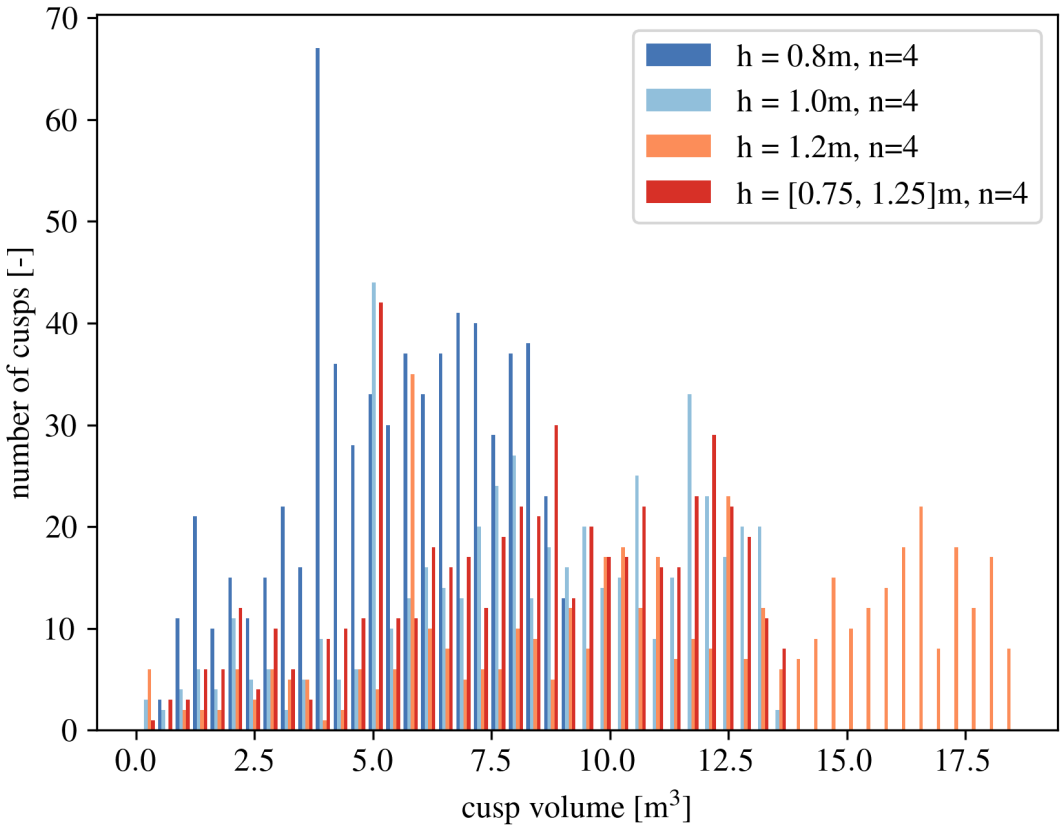

Figure 21: Cusp volume spectrum for varying the ice thickness h at fracture toughness $K_{Ic} = 145.7\,\mathrm{kN\,m^{-3/2}}$, scale effect law BZ and cracking due to pure tensile stress.

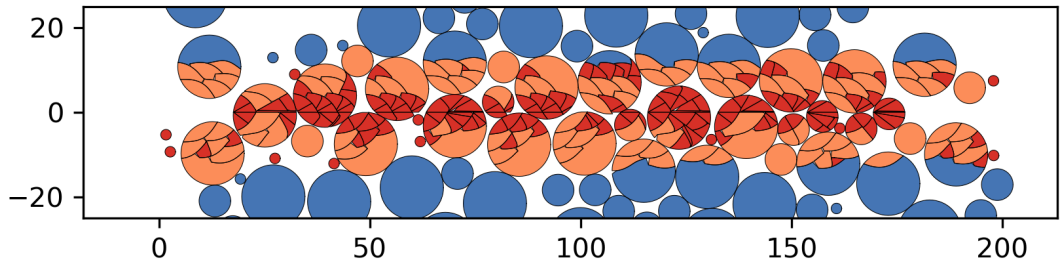

(a) $h = 0.8\,\mathrm{m}$

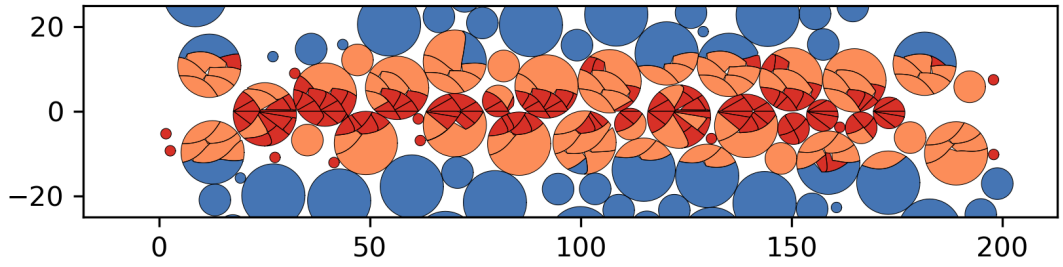

(b) $h = 1.0\,\mathrm{m}$

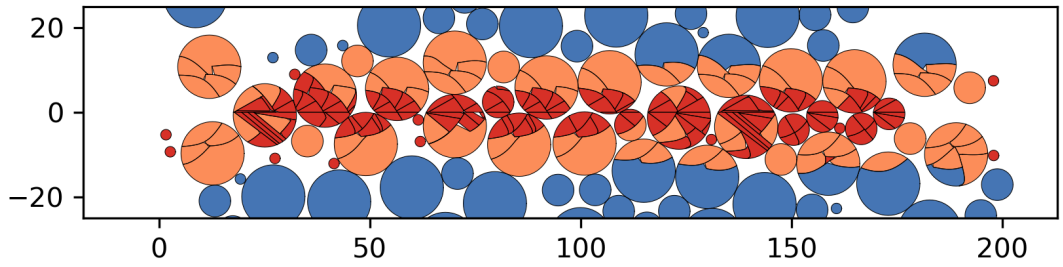

(c) $h = 1.2\,\mathrm{m}$

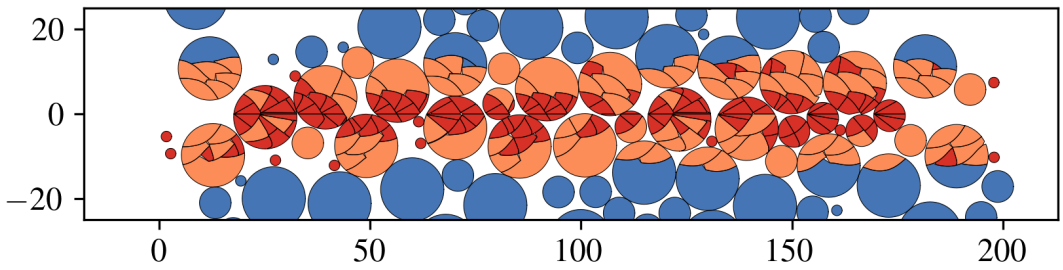

(d) $h \in [0.75\,\mathrm{m}, 1.25\,\mathrm{m}]$

Figure 22: Breaking pattern for varying ice thickness h using the ice floe field shown in Figure 1a. Floe properties: $K_{Ic} = 145.7\,\mathrm{kN\,m^{-3/2}}$, failure by tensile stress, scale effect law BZ. Blue floes are not changed, orange floes are flipped and are assumed to stay outside the bow and red floes are cracked until they are unbreakable due to their size and then handed to the propeller.

5.3.4. Varying the Scale Effect Law

The scale effect laws described by Bažant [26] and Bažant and Pfeiffer [27] are used in this work. Therefore, the tensile stress σ_n^t is described by Equations (15), (16) or (17). As introduced in Section 4.2, the first equation is marked as BZ, the second as BZ1 and the third as BZ2. This leads to the definition of the scale effect law variation scope

$$\mathrm{SEL} = \{\mathrm{BZ}, \mathrm{BZ1}, \mathrm{BZ2}\}.$$

The scale effect law in the reference configuration is the original scale effect law by Bažant (BZ). In Table 8, this row is highlighted in light blue. In comparison to the reference scale effect law, the first scale effect law by Bažant and Pfeiffer (BZ1) leads to 0.6% larger cusps than the reference configuration. In combination with slightly more cusps, the total area of all cusps increases by 2%. The distribution of the ice cusp volumes for BZ1 is nearly identical to those of BZ, as can be seen in Figure 23. Using the second scale effect law by Bažant and Pfeiffer (BZ2), the mean value of the cusp volume is about 1.2% larger than those of the BZ law. The number of cusps is again slightly higher than those of the reference configuration. This results in a total cusp area that is increased by 3% in comparison to the total cusp area using the BZ law. The distribution of the cusp volumes for the BZ2 law is slightly different to those of the other two scale effect laws: Larger cusp volumes occur more often than the smaller cusp volumes in comparison to the other two scale effect laws. This is also represented in the mean cusp volume listed in Table 8.

The total area of affected floes for the BZ1 law is

$$A_{BZ1}^{\mathrm{tot}} = A_{\mathrm{cusp},BZ1}^{\mathrm{tot}} + A_{\mathrm{flip},BZ1}^{\mathrm{tot}} = 3455.645\,\mathrm{m}^2$$

and that of the BZ2 law

$$A_{BZ2}^{\mathrm{tot}} = A_{\mathrm{cusp},BZ2}^{\mathrm{tot}} + A_{\mathrm{flip},BZ2}^{\mathrm{tot}} = 3442.19\,\mathrm{m}^2,$$

which are both less than 0.3% larger than the total area for the BZ law with

$$A_{BZ}^{\mathrm{tot}} = A_{\mathrm{cusp},BZ}^{\mathrm{tot}} + A_{\mathrm{flip},BZ}^{\mathrm{tot}} = 3446.38\,\mathrm{m}^2.$$

The similar breaking patterns for the different scale effect laws can also be seen in Figure 24.

Table 8: Mean values of cusp volume $\bar{V}_{\text{cusp}}$ and cusp area $\bar{A}_{\text{cusp}}$, number of cusps n_{cusp} and floes failed by direct rotation n_{flip}, the total area of the floes failed by direct rotation due to unbreakable size ($A^{\text{tot}}_{\text{cusp}}$) and due to their position at the bow ($A^{\text{tot}}_{\text{flip}}$) for different scale effect laws averaged over all four floe fields shown in Figure 1. The reference configuration is highlighted in light blue.

Scale Effect Law	$\bar{V}_{\text{cusp}}$	$\bar{A}_{\text{cusp}}$	n_{cusp}	n_{flip}	$A^{\text{tot}}_{\text{cusp}}$	$A^{\text{tot}}_{\text{flip}}$
BZ	$8.14\,\text{m}^3$	$8.14\,\text{m}^2$	125	83	$1019.48\,\text{m}^2$	$2426.90\,\text{m}^2$
BZ1	$8.19\,\text{m}^3$	$8.19\,\text{m}^2$	127	82	$1042.14\,\text{m}^2$	$2413.51\,\text{m}^2$
BZ2	$8.24\,\text{m}^3$	$8.24\,\text{m}^2$	127	83	$1051.12\,\text{m}^2$	$2391.07\,\text{m}^2$

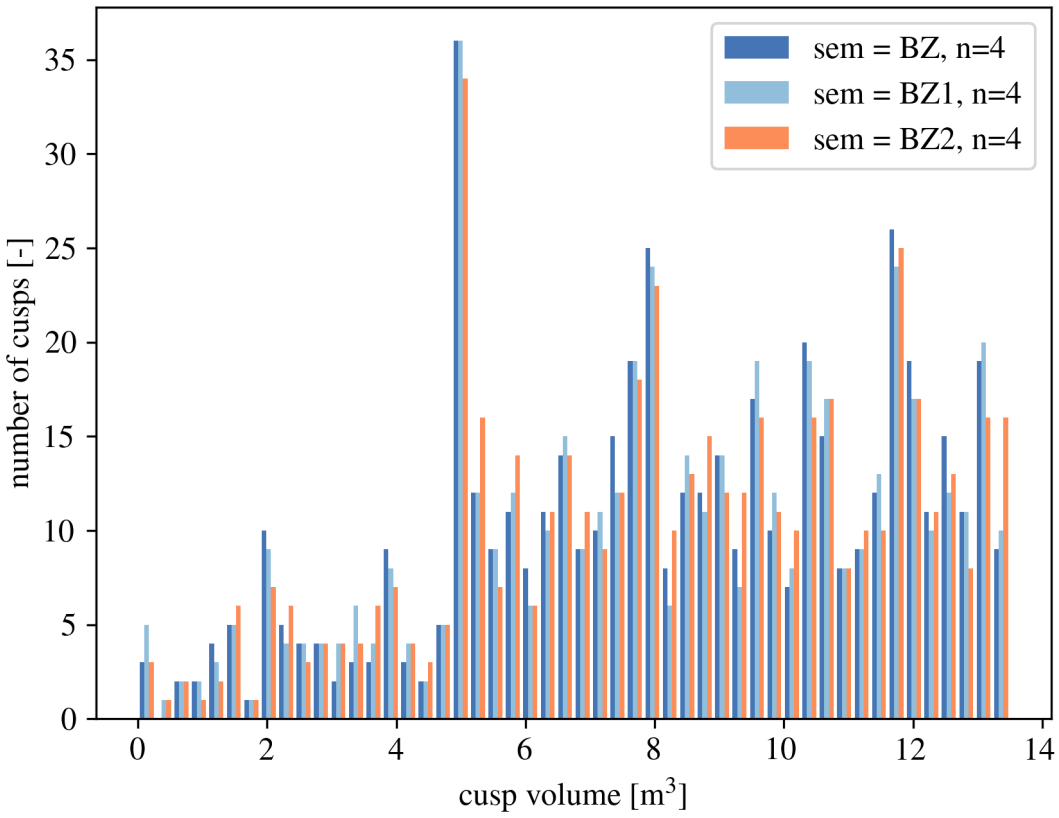

Figure 23: Cusp volume spectrum for varying the scale effect law at fracture toughness $K_{Ic} = 145.7\,\text{kN}\,\text{m}^{-3/2}$, ice thickness $h = 1.0\,\text{m}$ and cracking due to pure tensile stress.

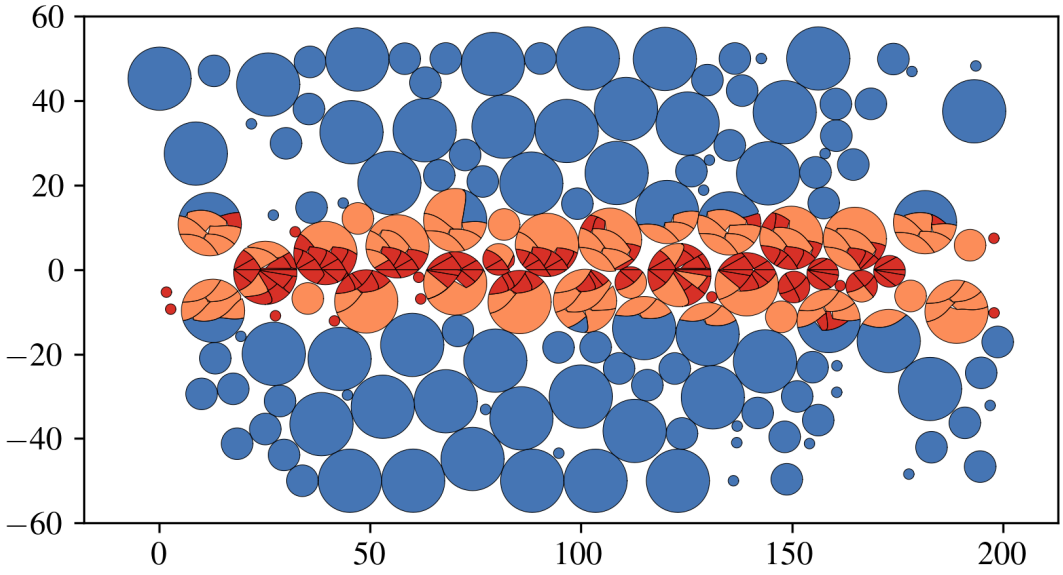

(a) BZ

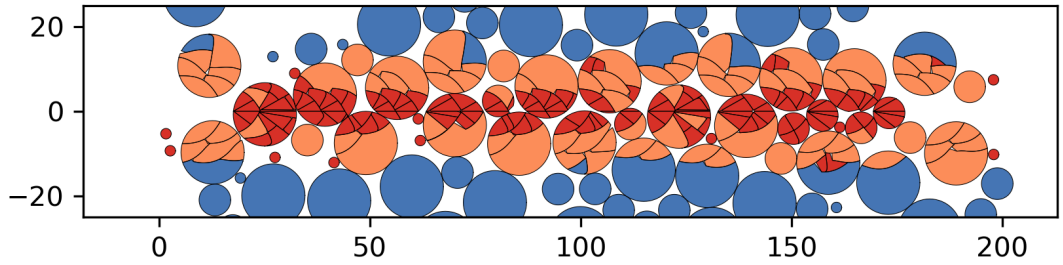

(b) BZ1

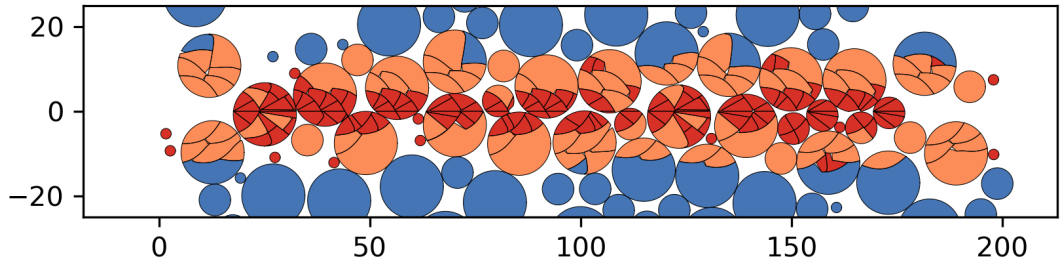

(c) BZ2

Figure 24: Breaking pattern for varying scale effect law using the ice floe field shown in Figure 1a. Floe properties: $K_{Ic} = 145.7\,\mathrm{kN\,m^{-3/2}}$, $h = 1.0\,\mathrm{m}$, failure by tensile stress. Blue floes are not changed, orange floes are flipped and are assumed to stay outside the bow and red floes are cracked until they are unbreakable due to their size and then handed to the propeller.

5.3.5. Conclusion of Parameter Studies

The parameter that has the greatest influence on the cusp size and cusp volume is the ice thickness h. Varying h by 20%, the cusp volume changes accordingly by around 35%. Figure 25 shows the influence of these two parameters on the breaking properties. Meaning, an increase in the ice thickness leads to an increase in the cusp volume and vice versa. This is due to the doubled effect of the increasing cusp area for increasing ice thickness values and the multiplication of this area with the ice thickness to determine the cusp volume. In comparison, the stochastic variation of the ice thickness has a smaller impact than the mean value of the ice thickness. This variation can be used to randomize the results slightly, but not to obtain a different breaking pattern or cusp sizes.

The parameter with the second largest impact is the breaking mode for the cracking failure. Especially the linear crack face loading leads to larger and especially more ice cusps than the other values. Additionally, the point load case proposed by Lu et al. [21] leads to a relatively large decrease in the cusp volume while the number of cusps remains constant. Therefore, the cusp area is affected by this breaking mode with a decrease of around 20% in comparison to the linear crack face case. On the other hand, the difference in the total cusp area between the two stress-based cases is less than 4% concerning the tensile stress case.

Both changing the scale effect law and the fracture toughness in the scope of this work results in small changes for the mean cusp volume in the range of 1%. Due to different numbers of cusps, the total area of the cusps varies up to 3% for different fracture toughness values.

Since four different, randomly generated floe fields are included in this parameter study, a mean value can be created, but stochastic effects are still present. Therefore, especially the small influences detected in this parameter study are somewhat uncertain. The influences of the ice thickness and the difference between the force-based and stress-based cracking criteria are so large that they are outside of the range of stochastic uncertainties. Resulting from this parameter study, the ice thickness and the breaking mode for the cracking case are the most influential parameters in the developed simulation tool. This coincides with the findings by Erceg et al. [8] that the ice thickness is the main parameter influencing the icebreaking pattern in level ice, especially the length of the broken ice cusps.

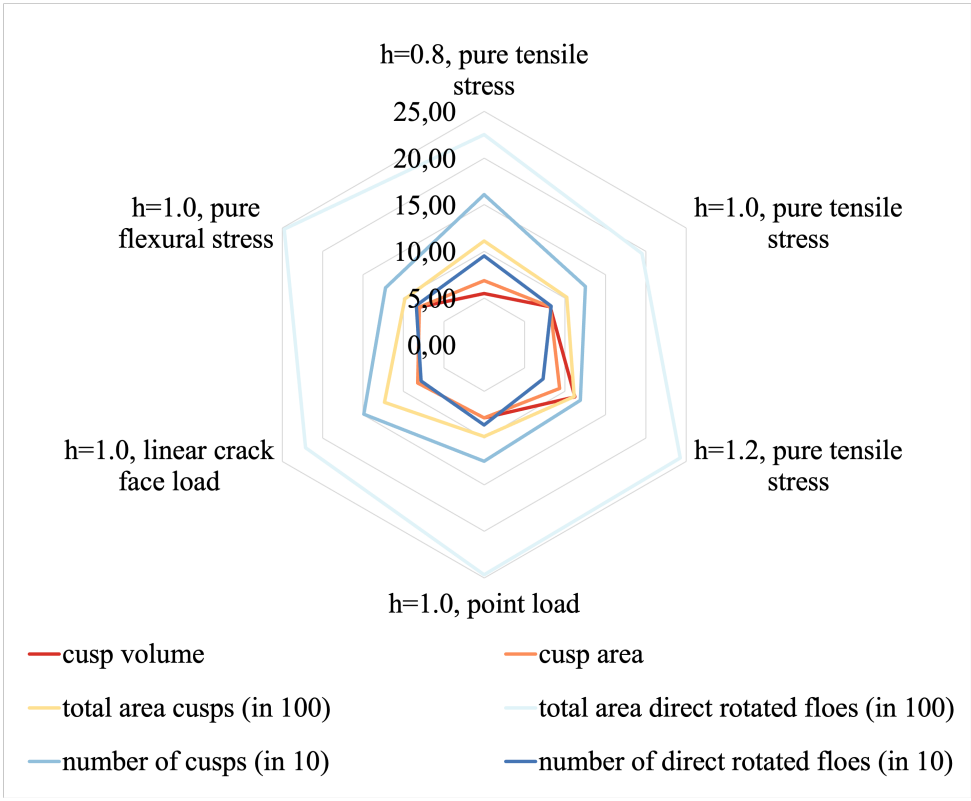

Figure 25: Spider diagram to sum up the results of the most relevant parameters of the parameter study. The more the data line is a regular hexagon, the less the influence of the different parameters on this cusp or floe property. All areas are given in [m^2], all volumes in [m^3].

6. Propeller–Ice Interaction

In this work, the icebreaking simulation is combined with an interpolation scheme to generate a propeller–ice load spectrum caused by the resulting ice cusps from the icebreaking simulation. Based on the finite element method (FEM) simulation of four exemplarily ice cusps described in Section 6.1.1 a cubic interpolation polynomial is defined and used to determine the additional loads due to ice contact at the propeller. This FEM simulation is not part of this work, instead only the results of the FEM simulation are used for further calculations. Section 6.1.2 introduces the model used in the FEM simulation to allow a detailed discussion of the computed forces and torques in Sections 6.2 and 6.3 in accordance with the icebreaking simulation developed in this work, as described in Sections 3 and 4.

6.1. Method

In the following, the methods used to generate an ice load spectrum based on the ice cusps computed by the icebreaking simulation developed in this work are described. The PSRV S.A. Agulhas II has two variable pitch propellers. In this work, the total amount of ice cusps interaction with both propellers is regarded.

6.1.1. Exemplary Ice Cusps

The overall method uses exemplary ice cusps to calculate the resulting forces and torques using a FEM simulation. These exemplary values are then interpolated to get a rough function to determine the occurring forces and torques depending on the ice cusp size. First, the ice cusps resulting from the simulation described in Section 3 are categorized in four different volume categories

$$\begin{aligned} V_1 &\leq 5\,\mathrm{m}^3 \\ 5\,\mathrm{m}^3 < V_2 &\leq 8\,\mathrm{m}^3 \\ 8\,\mathrm{m}^3 < V_3 &\leq 11\,\mathrm{m}^3 \\ 11\,\mathrm{m}^3 < V_4 &\leq 14\,\mathrm{m}^3. \end{aligned}$$

For every volume category, the ice cusp dimensions are averaged using the resulting breaking pattern of all single floes described in Section 5.2. Therefore, the mean values of the thickness and the lengths of the shorter and longer edge of the cuboidal bounding box around the ice cusp are computed. The main parts of the determination of these bounding boxes are shown in Figure 26 and Algorithm 1. The reason for choosing four different size categories is that this allows using cubic interpolation polynomials and therefore respects a potentially higher order nonlinearity of the dependence between the ice cusp volume and the resulting forces and torques. This limited number of size categories is chosen to keep the computational time small. Therefore, the chosen number of volume categories is a compromise between the accuracy and the computational effort of the interpolation and the needed FEM simulations. The resulting ice cusp dimensions are listed in Table 11.

Algorithm 1: Determination of averaged ice cusp sizes

input : ice cusp arrays
output: Mean cusp volumes and dimensions

for *cusp_array* **in** *ice_cusp_arrays* **do**
  Read cusps and save to *cusp_list*
  for *cusp* **in** *cusp_list* **do**
    Compute the bounding box of the ice cusp and get the dimensions of the box
    Add bounding box dimensions (x, y, z) to *bounding_box_list*
    Add bounding box volume to *cusp_volume_list*
  end
end
$volume\_list \leftarrow [5, 8, 11, 14]$
for *i, volume* **in** *volume_list* **do**
  if $i > 0$ **then** $prevVolume = volume\_list[i-1]$
  else $prevVolume = 0$
  $ind \leftarrow$ **where**($cusp\_volume\_list \leq volume$ **and** $cusp\_volume\_list > prevVolume$)
  $longerSide \leftarrow$ **max**($bounding\_box\_list[ind][:, :2]$, axis=1)
  $shorterSide \leftarrow$ **min**($bounding\_box\_list[ind][:, :2]$, axis=1)
  $meanLonger \leftarrow$ **mean**($longerSide$)
  $meanShorter \leftarrow$ **mean**($shorterSide$)
  $meanThickness \leftarrow$ **mean**($bounding\_box\_list[ind][:, 2]$)
  $meanVolume \leftarrow$ **mean**($cusp\_volume\_list[ind]$)
  Save calculated mean values to *meanDimension*
end

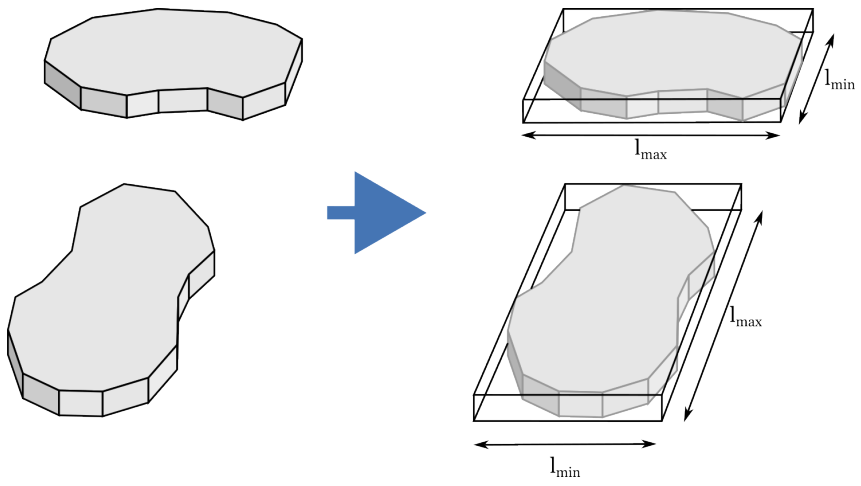

Figure 26: Method to get the ice cusp bounding box mean values. The side lengths of the bounding boxes are classified as shorter side length $l_{\min}$ and longer side length $l_{\max}$.

6.1.2. FEM simulation

Using the FEM simulation, the peak forces in the x-direction and torques around the x-axis are determined. These values are shown in Table 11. The simulation setting is shown in Figure 28 for neutral pitch position $P_{0.7_{\%}} = 0\%$ and in Figure 29 for pitch $P_{0.7_{\%}} = 95\%$. The pitch is defined as the distance covered by the idealized propulsion during one propeller revolution. The pitch is computed at 70% of the propeller radius and is adjusted by the angle of the propeller blades, as depicted in Figure 27 [49]. The percentage pitch value is the current pitch in relation to the maximum pitch. The propeller is modelled as a rigid body and rotates with a constant circumferential velocity and 140 rotations per minute. In this work, the contact between one propeller blade and the ice cusp is regarded. Therefore, the propeller rotates for 130° or up to 160°, such that one blade fully crosses the ice cusp. The propeller of the S.A. Agulhas II is made of stainless

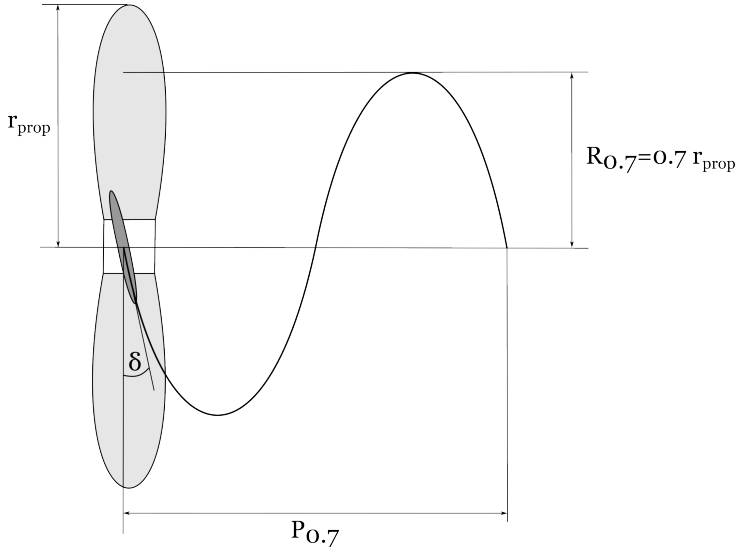

Figure 27: The propeller pitch is defined as the distance covered by the idealized propulsion during one propeller revolution. The sinusoidal curve marks the trajectory in the xz-plane of the $0.7r_{\text{prop}}$ point on the dark grey propeller blade during one rotation of the propeller.

steel. In this work, the material parameters of steel 1.4217 used are listed in Table 9. The propeller pitch at the position $R_{0.7} = 0.7r_{\text{prop}}$ is set to two different values: First, the neutral position

$$P_{0.7}^{0} = 0\,\text{m}$$

is used as the first approach. Afterwards, the real pitch that was used during the ice observation slot, is used for the simulation. The mean pitch percentage at measurement slot 18.12.2019, 20:20-20:29 is

$$P_{0.7_{\%}} = 95.8551\%$$

with minimum and maximum pitch percentages of $P_{0.7_\%}^{\min} = 95.75\%$ and $P_{0.7_\%}^{\max} = 95.91\%$. The maximum pitch of the propeller of the S.A. Agulhas II is [50]

$$P_{0.7} = 5.15\,\text{m}.$$

This leads to the actual pitch value at pitch percentage 95%

$$P_{0.7}^{95} = P_{0.7_\%} P_{0.7} = 4.9365\,\text{m}.$$

The pitch can be defined as

$$P(x) = \sin\left(\frac{2\pi}{P_{0.7}^{95}} x\right) R_{0.7} \tag{22}$$

with

$$R_{0.7} = 0.7 r_{\text{prop}}$$

being 70% of the total propeller radius r_{prop} [49]. The propeller parameters are listed in Table 9. To determine the propeller pitch angle δ_P at position $x = 0$ using Equation (22), the following equation holds:

$$\delta_P = \arctan\left(\frac{1}{\frac{d}{dx}P(0)}\right)$$

Using

$$\frac{d}{dx}P(x) = \frac{2\pi}{P_{0.7}^{95}} \cos\left(\frac{2\pi}{P_{0.7}^{95}} x\right) R_{0.7}$$

and the values of the propeller radius and maximum pitch, the Equation (22) leads to

$$\delta_P = 20.07°.$$

The rotation interval of the propeller is chosen such that the propeller blade fully enters and leaves the ice cusp. This scenario is chosen to represent as many load case scenarios for an open propeller named in *Rules for Ice and Cold Operations* by the International Maritime Organization [51] as possible.

The ice cusp is modelled with two different materials: The part of the ice cusp that interacts with the propeller is modelled using the Mohr-Coulomb ice material model by Herrnring [11]. The material parameters used for the FEM analysis are slightly different from those in the icebreaking simulation. To enable comparability with the work of Erceg et al. [8], the parameters given by Erceg et al. are used for the simulation, whereas in the FEM simulation, the parameters proposed by Herrnring [11] are used since these parameters are validated for the Mohr-Coulomb model. The parameters used in the FEM simulation are listed in Table 9. The other part of the ice cusp, which has no interaction with the propeller, is modelled as a rigid body with the same mass and inertia as the equivalent Mohr-Coulomb ice model would have. This is done to decrease the

Table 9: Material parameters and propeller dimensions used in the FEM simulation. The ice parameters used are the same as proposed by Herrnring [11] to use with the Mohr-Coulomb ice model.

Parameter	**Symbol**	**Value**	**Unit**
density of steel 1.4217	ρ_{prop}	7850	$\frac{\text{kg}}{\text{m}^3}$
Young's modulus of steel 1.4217	E_{prop}	210	GPa
Poisson's ratio of steel 1.4217	ν_{prop}	0.3	-
propeller radius	r_{prop}	2.15	m
maximal propeller pitch	$P_{0.7}$	5.15	m
density of ice	$\rho_{\text{ice}}^{\text{FEM}}$	900	$\frac{\text{kg}}{\text{m}^3}$
Young's modulus of ice	$E_{\text{ice}}^{\text{FEM}}$	3.5	GPa
Poisson's ratio of ice	$\nu_{\text{ice}}^{\text{FEM}}$	0.33	-

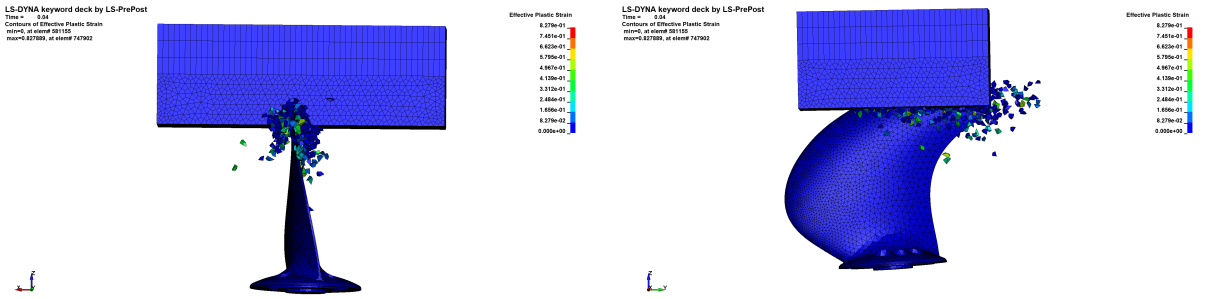

(a) xy-plane (b) yz-plane

Figure 28: FEM simulation of propeller–ice interaction. The propeller is modelled as a rigid body, the ice is described using a Mohr-Coulomb material model. The modelled ice cusp is the smallest cusp volume listed in Table 11. The propeller pitch is set to $P_{0.7_{\%}} = 0\%$.

computational effort of the model. Two different ice model separations are done in this work: The ice models for the neutral pitch position are separated horizontally, as can be seen in the different discretization structures in Figure 28. For the propeller pitch $P_{0.7_{\%}} = 95\%$, the ice model is separated vertically, as depicted in Figure 29. In the first case, the ice cusp is placed such that the propeller penetrates the bottom quarter of the ice cusp, whereas in the latter case, the top point of the cusp is fixed and the propeller penetrates the whole ice cusp. This leads to a varying contact area between the propeller and the ice cusp. In the latter case, the cusp is separated vertically to avoid feedback from the rigid part of the ice cusp due to the large penetration depth.

The FEM simulation is not part of this work, instead only the results of the FEM simulation are used for further calculations. The resulting forces and the torques around the x-axis acting on the propeller averaged for the highest 100 values each are listed in Table 11. This averaging is used to overcome the occurring load and torque peaks, which occur especially for the smaller cusp sizes. Possible reasons are discussed in Section 6.3.

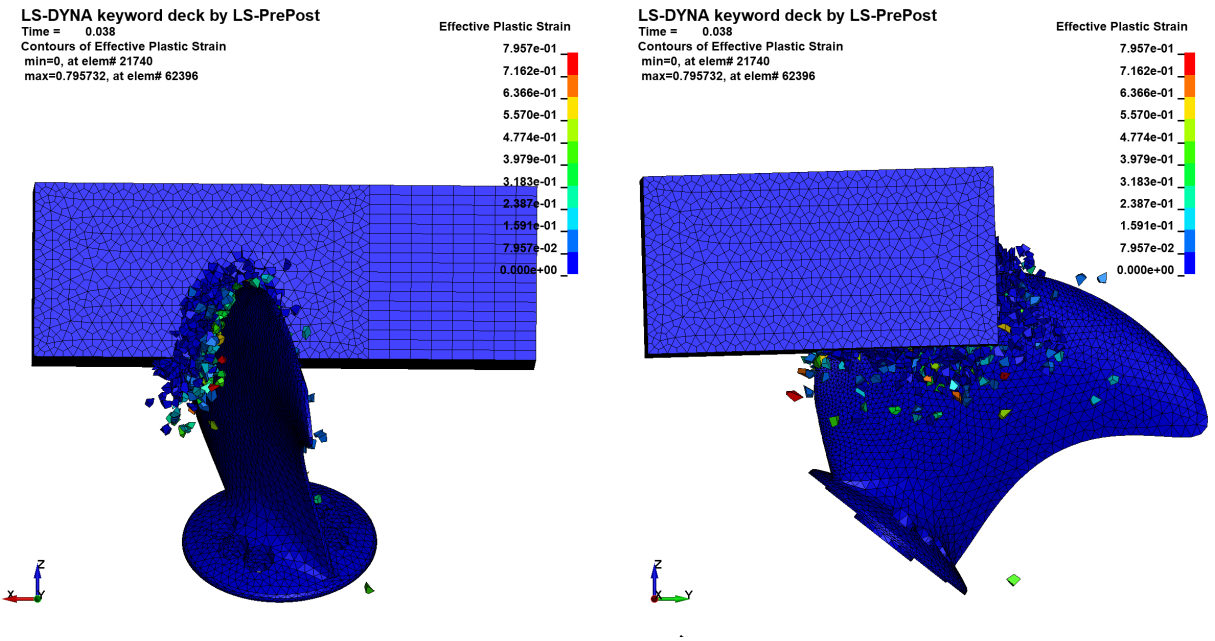

(a) xy-plane (b) yz-plane

Figure 29: FEM simulation of propeller–ice interaction. The propeller is modelled as a rigid body, the ice is described using a Mohr-Coulomb material model. The modelled ice cusp is the smallest cusp volume listed in Table 11. The propeller pitch is set to $P_{0.7_{\%}} = 95\%$.

Table 10: Propeller–ice contact forces for exemplary ice cusps and neutral pitch position

Cusp Volume	Length	Width	Height	Force	Torque
0.0000 m^3	0.0000 m	0.0000 m	0.0000 m	0.0 kN	0.0 kN m
3.7073 m^3	2.5006 m	1.7095 m	0.8672 m	240.55 kN	−244.58 kN m
6.5232 m^3	3.4286 m	2.2244 m	0.8553 m	263.11 kN	−267.17 kN m
9.4535 m^3	3.6429 m	2.5951 m	1.0000 m	291.05 kN	−282.97 kN m
12.5043 m^3	4.0715 m	2.8230 m	1.0879 m	362.60 kN	−347.22 kN m

Table 11: Propeller–ice contact forces for exemplary ice cusps and pitch percentage $P_{0.7_{\%}} = 95\%$

Cusp Volume	Length	Width	Height	Force	Torque
0.0000 m^3	0.0000 m	0.0000 m	0.0000 m	0.0 kN	0.0 kN m
3.7073 m^3	2.5006 m	1.7095 m	0.8672 m	763.09 kN	−841.47 kN m
6.5232 m^3	3.4286 m	2.2244 m	0.8553 m	1058.27 kN	−1092.60 kN m
9.4535 m^3	3.6429 m	2.5951 m	1.0000 m	1434.74 kN	−1384.67 kN m
12.5043 m^3	4.0715 m	2.8230 m	1.0879 m	1686.20 kN	−1658.78 kN m

6.1.3. Ice Load Spectrum

Since the hydrostatic and hydrodynamic properties of an ice cusp are mainly dependent on its volume, the computed forces and torques are interpolated with respect to the cusp volume. The force and torque values used for the interpolation are given in Table 11. In addition to the force and torque computed by the FEM simulation for the exemplary ice cusps, as a boundary condition, the force and torque for volume $V_{\text{cusp}} = 0$ are set to 0. This leads to $k = 5$ interpolation points and the interpolation using a Newton polynomial of order $n = k - 1$

$$\begin{aligned} p_4(V) = {} & f_0(x_0) + f_1(x_0, x_1)(V - x_0) \\ & + f_2(x_0, x_1, x_2)(V - x_0)(V - x_1) \\ & + f_3(x_0, x_1, x_2, x_3)(V - x_0)(V - x_1)(V - x_2) \\ & + f_4(x_0, x_1, x_2, x_3, x_4)(V - x_0)(V - x_1)(V - x_2)(V - x_3) \end{aligned}$$

with the Newton coefficients

$$f_1(x_i, x_{i+1}) = \frac{f_0(x_{i+1}) - f_0(x_i)}{x_{i+1} - x_i}, i \in \{0, 1, 2, 3\} \tag{23}$$

$$f_2(x_{i-1}, x_i, x_{i+1}) = \frac{f_1(x_i, x_{i+1}) - f_1(x_{i-1}, x_i)}{x_{i+1} - x_{i-1}}, i \in \{1, 2, 3\} \tag{24}$$

$$f_3(x_{i-1}, x_i, x_{i+1}, x_{i+2}) = \frac{f_2(x_i, x_{i+1}, x_{i+2}) - f_2(x_{i-1}, x_i, x_{i+1})}{x_{i+2} - x_{i-1}}, i \in \{1, 2\} \tag{25}$$

$$f_4(x_{i-2}, x_{i-1}, x_i, x_{i+1}, x_{i+2}) = \frac{f_3(x_{i-1}, x_i, x_{i+1}, x_{i+2}) - f_3(x_{i-2}, x_{i-1}, x_i, x_{i+1})}{x_{i+2} - x_{i-2}}, i = 2 \tag{26}$$

is used to allow a nonlinear representation of the volume–force and the volume–torque dependencies including all exemplary cusps as a function of the cusp volume V. The function f_0 represents the observed forces or torques during the FEM simulation and the variables x_i are used for the volumes used in the simulation. All values are listed in Table 11. The relation between the volume and the resulting forces is shown in Figure 30, the relation between the volume and the torque around the x-axis in Figure 31. Both relations are based on the values given in Table 11. The resulting load and torque spectra are shown in Figure 32 and Figure 33.

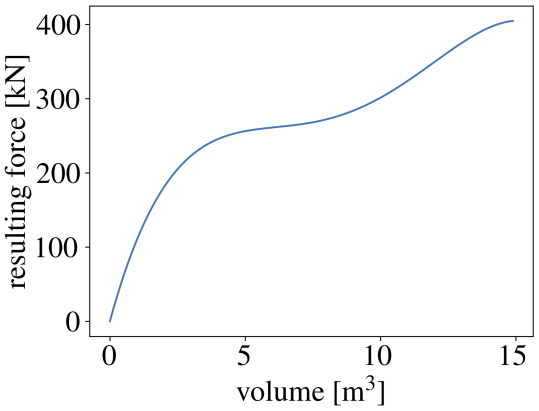

(a) $P_{0.7_{\%}} = 0\%$

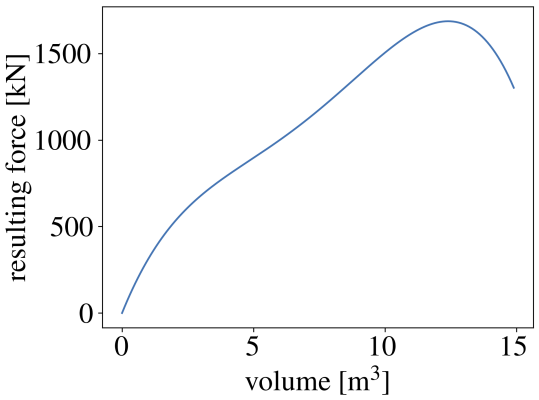

(b) $P_{0.7_{\%}} = 95\%$

Figure 30: Relation between the cusp volume and the resulting forces at the propeller for neutral pitch position $P_{0.7_{\%}} = 0\%$ and pitch $P_{0.7_{\%}} = 95\%$. The function is obtained using Newton's polynomial.

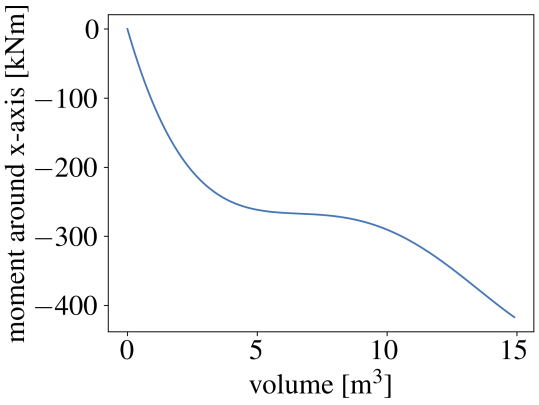

(a) $P_{0.7_{\%}} = 0\%$

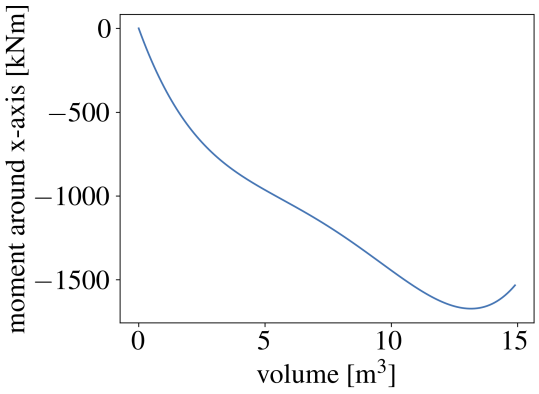

(b) $P_{0.7_{\%}} = 95\%$

Figure 31: Relation between the cusp volume and the torque around the x-axis at the propeller for neutral pitch position $P_{0.7_{\%}} = 0\%$ and pitch $P_{0.7_{\%}} = 95\%$. The function is obtained using Newton's polynomial.

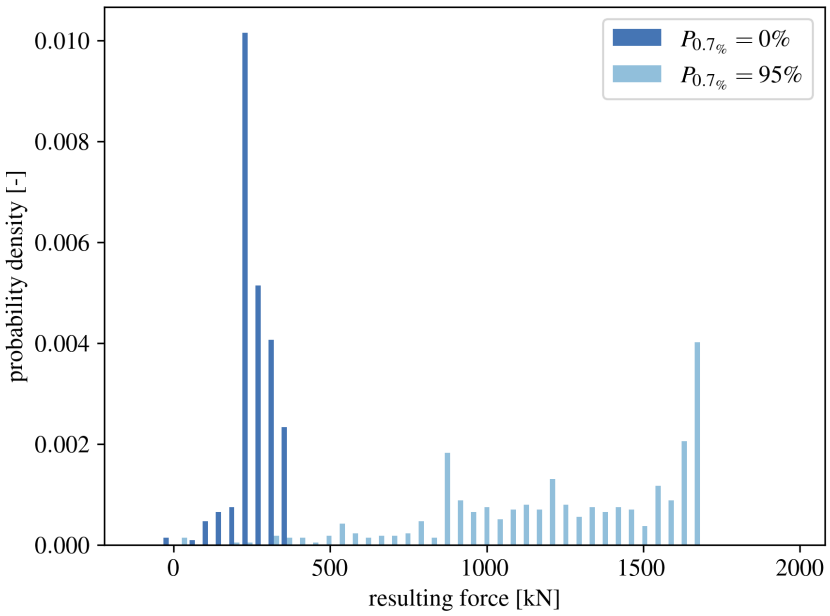

Figure 32: Load spectrum for reference configuration averaged over all four floe fields shown in Figure 1 for both pitch values regarded in this work.

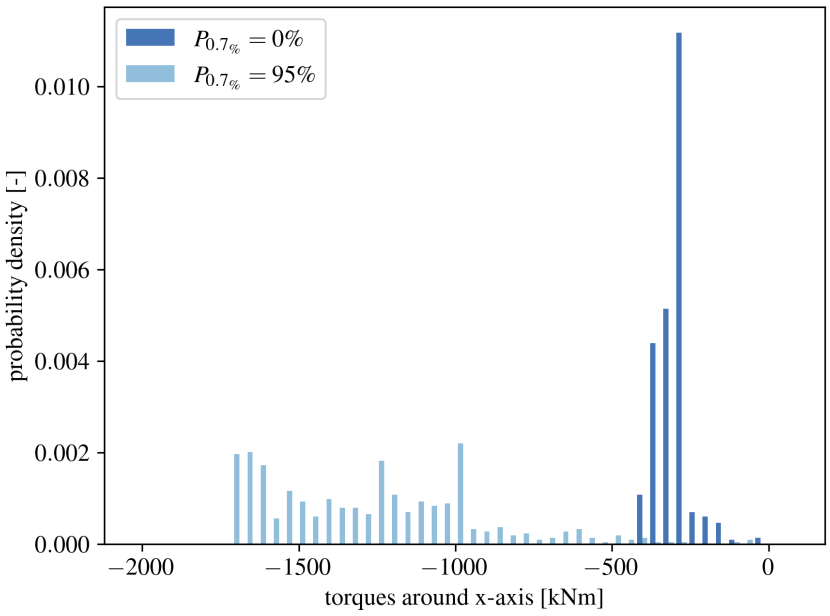

Figure 33: Torque spectrum for reference configuration averaged over all four floe fields shown in Figure 1 for both pitch values regarded in this work.

6.2. Comparison with Full-Scale Field Data

The computed torque spectrum computed for the propeller is compared to the measured torque distribution at the propulsion shaft during the expedition of PSRV S.A. Agulhas II in Antarctic regions during the summer season of 2019/20. The floe field data used in this simulation are extracted from the ice observation period on December 18, 2019, between 20:20 and 20:30. The measured torques of this observation period are shown in Figure A.2. The corresponding torques measured at the propulsion shaft are shown in Figure 35 using a logarithmic scale for the probability density. The same torques shown with a linear scale for the probability density are shown in Appendix A.3. The different points of measured and simulated torques are shown in Figure 34.

The simulated torque spectrum is made for two pitch angle configurations: First, a neutral position with pitch $P_{0.7} = 0\,\mathrm{m}$ is used. Afterwards, the same pitch as during the measurement cycle is used, namely $P_{0.7_\%} = 95\%$. The mean value of the observed ice thickness for the named observation period is $h = 0.4\,\mathrm{m}$, which is also used in this comparison for the simulated torque spectrum. It has to be noted that the measured torque spectrum contains all measured torques, including the influence of the surrounding water, whereas the simulated torque contains only the maximum torques that occurred for every ice cusp. Additionally, the measured torques are measured at the propulsion shaft whereas the simulated torques are computed directly at the propeller. Furthermore, the measured torques are sampled at the port-side shaft only whereas the simulated torques are computed for both propellers. Therefore, the comparison has to be made considering this difference.

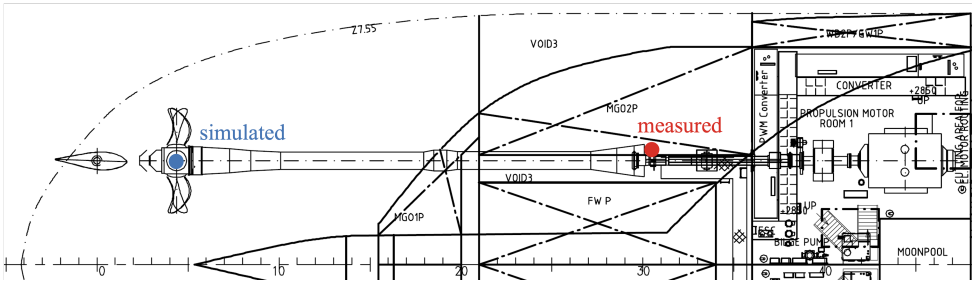

Figure 34: Simulation and measurement positions at the port-side propeller shaft of PSRV S.A. Agulhas II. The torques were measured at the propulsion shaft and are simulated directly at the propeller [52].

The torques measured vary between $T_{\mathrm{prop}}^{\mathrm{meas}} = -100\,\mathrm{kN\,m}$ and $T_{\mathrm{prop}}^{\mathrm{meas}} = 400\,\mathrm{kN\,m}$, with the significant part of the occurring torques in the range $[58\,\mathrm{kN\,m}, 152\,\mathrm{kN\,m}]$ with a probability density above 0.1%. The simulated torques for the neutral pitch position vary between $T_{\mathrm{prop}}^{\mathrm{P}0}_{0.7} = 20\,\mathrm{kN\,m}$ and $T_{\mathrm{prop}}^{\mathrm{P}0}_{0.7} = 210\,\mathrm{kN\,m}$, with the range $[58\,\mathrm{kN\,m}, 208\,\mathrm{kN\,m}]$ having a probability density above 0.1%. For the same pitch as in the measurement set, the occurring torques vary between $T_{\mathrm{prop}}^{\mathrm{P}95}_{0.7} = 0\,\mathrm{kN\,m}$ and $T_{\mathrm{prop}}^{\mathrm{P}95}_{0.7} = 1575\,\mathrm{kN\,m}$. The probability density of at least 0.1% is fulfilled for most of the occurring forces larger than $T_{\mathrm{prop}}^{\mathrm{P}95}_{0.7} = 900\,\mathrm{kN\,m}$, even if none of these torques reaches a probability density of 1%.

The simulation of both propellers in comparison with the measured torques at only one

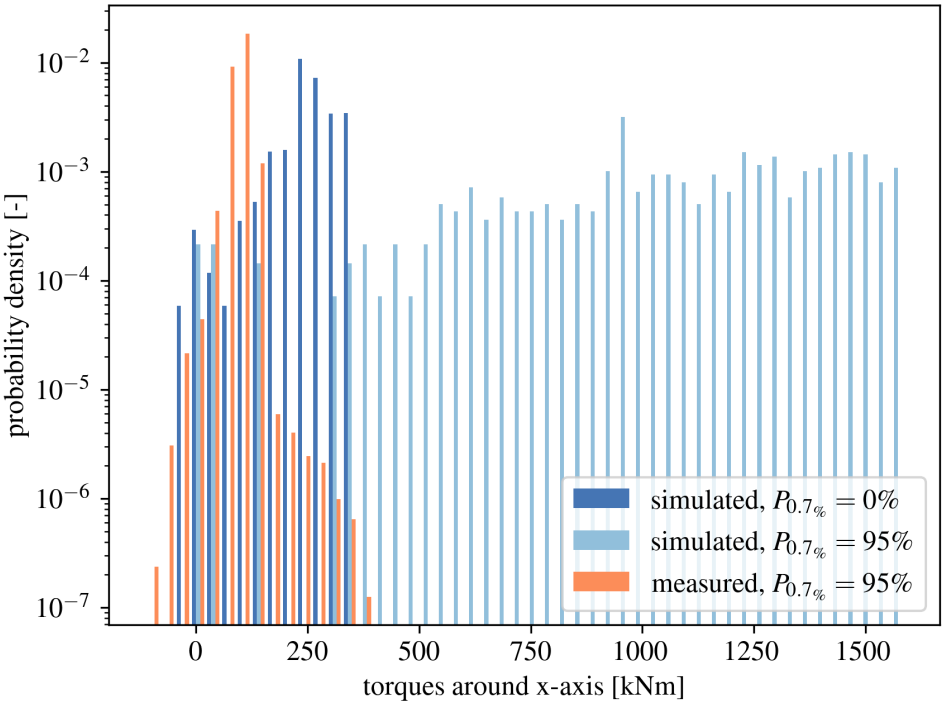

Figure 35: Spectrum of measured torques at the propulsion shaft and simulated torques at the propeller of PSRV S.A. AGULHAS II in ice thickness $h = 0.4\,\mathrm{m}$. The simulated torques are multiplied by -1 for better comparison. The y-axis is in logarithmic scale to also show the boundary areas of the measured torques.

propulsion shaft leads to a larger number of occurring torques. Additionally, all ice cusps are assumed to migrate into the propeller, which is not proven for the measured data. Since the probability density is used to compare the torques, the spectra are normalized to the same scale and thus comparable even if different numbers of cusps migrate into the propeller. Nevertheless, the limitations in the comparability due to the different measuring points remain unaffected by the normalization.

The simulated results overestimate the mean value of the measured torques. The simulation using the neutral pitch position underestimates the maximum value of the measured torques, whereas the simulation using the same pitch position as in the measurement set overestimates the maximum value. Possible reasons for this overestimation or underestimation of maximum and mean torque values are given in Section 6.3.

6.3. Conclusion of Propeller–Ice Interaction

In this section, the main findings of the propeller–ice interaction are summarized and reviewed.

Maximum Values Especially for smaller floes, some force and torque peaks occur during the FEM simulation mentioned in Section 6.1.2: For every simulation set few values occur, which are more than twice as high as the mean value over the 100 largest torque or force values. These values are assumed to be caused by numerical or simulation errors, for which the reasons are discussed in the following paragraphs.

Probable reasons for these peaks are the discretization of the propeller and the modelling of the propeller as a rigid, non-elastic body as well as the discretization of the ice cusp. Depending on the discretization of the propeller, the propeller blade surface is more or less smooth. Using a rough discretization can lead to sharp edges at the propeller surface, which again can lead to higher contact forces. The same holds for the discretization of the ice cusp. The torques measured are sampled at a sampling rate of 600 Hz, whereas the FEM simulation is driven at a discretization rate of 100 kHz. Two possible scenarios can occur, that influence the difference in the occurrence of torque peaks: On the one hand, the lower sampling rate of the measured data could miss the high impacts causing the peaks in torque data. On the other hand, these peaks can be caused by noise due to the numerical inaccuracy of the FEM simulation.

Since the propeller is modelled as a rigid body, no deformations are modelled. Especially during the initial contact with the ice cusp, high impacts can be the result. Time discretization can also be a factor that influences the peak occurrence due to numerical instability.

Mean Values One possible reason for the overestimation of the mean value by the simulated torque values is the focus on the largest torques during the simulation: Only the 100 largest torques and forces are indicated by the interpolation polynomials describing the relation between the cusp volume and the torques respective the forces. This leads to an underrepresentation of the lower values in the simulated torque data.

Another reason for the overestimation can be due to the peak values of the torques computed by the FEM simulation, which occur due to the discretization and contact conditions in the model, as described in Section 6.1.2. This can lead to an overestimation of the maximum values for the non-neutral pitch position. Furthermore, the torques measured at the propulsion shaft are expected to be lower than those appearing at the propeller. This is due to friction loss at the bearings, the moments of inertia of the propulsion components as well as other boundary conditions like the damping of the water surrounding the propeller.

Additionally, the forces and torques computed by the FEM simulation of the model with the propeller pitch $P_{0.7_{\%}} = 95\%$ are five to ten times higher than those computed of the model with the neutral pitch position. The reason can be the penetration depth of the propeller blade due to the different initial positions of the ice cusp. Different simulation settings are used for the different pitch angle simulations. The ice cusp for the simulation using the neutral pitch position is placed, such that the propeller indents the lower quarter of the cusp. The ice cusp for the simulation of the propeller blade rotated by the pitch $P_{0.7_{\%}} = 95\%$ is placed, such that the propeller indents the whole ice cusp. The latter results in a larger contact area between the cusp and the propeller. Since the pressure exerted on the propeller by the ice cusp is approximately the same for both cases, the resulting forces and therefore the resulting torques increase with an increasing contact area.

As described in Section 6.2, the simulated torque spectrum at the propeller is in the same magnitude as the measured torque spectrum, even though the simulated torques overestimate the torques occurring at the propeller. Possible reasons for this are the torque peaks due to the discretization and the use of interpolated force-volume and torque-volume functions.

Kinetic Energy of Ice Cusps Another influence on the differences between the measured and the simulated torques may be caused by the neglection of the kinetic energy of the ice cusps due to the static simulation of the ice cusps during the propeller–ice contact simulation. To estimate the error made, the energy of the four exemplary ice cusps described in Table 11 is computed. The kinetic energy is generally described by

$$E_{\text{kin}} = \frac{1}{2} m_{\text{cusp}} v_{\text{cusp}}^2 \tag{27}$$

with the mass of the ice cusp m_{cusp} and the speed of the cusp relative to the vessel v_{cusp}. The mass of the cusp is determined by

$$m_{\text{cusp}} = V_{\text{cusp}} \rho_{\text{ice}} \tag{28}$$

with the cusp volume V_{cusp} and the density of sea ice $\rho_{\text{ice}} = 917\,\frac{\text{kg}}{\text{m}^3}$. The velocity of the ice cusp relative to the vessel is assumed to be constant and equal to the vessel surge speed $v_{\text{cusp}} = v_{\text{ship}} = 3\,\frac{\text{m}}{\text{s}}$. Inserting Equation (28) into Equation (27) leads to the kinetic energies

$$E_{\text{kin},1} = 15.32\,\text{kJ}, \quad E_{\text{kin},2} = 26.90\,\text{kJ}, \quad E_{\text{kin},3} = 39.00\,\text{kJ}, \quad E_{\text{kin},4} = 51.59\,\text{kJ}$$

with the cusp volumes

$$V_1 = 3.71\,\mathrm{m}^2, \quad V_2 = 6.52\,\mathrm{m}^2, \quad V_3 = 9.45\,\mathrm{m}^2, \quad V_4 = 12.50\,\mathrm{m}^2.$$

The additional loads due to the kinetic energy of the ice cusps are relatively small compared to the loads and torques caused by the direct propeller ice interaction. Even the highest additional kinetic energy caused by the largest of the four exemplary ice cusps is less than 5% of the mean torques around the x-axis. For exact results, the kinetic energy of the cusps should be regarded. Because of the uncertainties due to the arbitrarily shaped ice cusps, which are modelled as cuboid bodies in the FEM simulation, the resulting load and torque spectra are only approximations of the real loads and torques. Therefore, the additional inaccuracy due to the neglected kinetic energy can be accepted.

7. Discussion of Results

In the following, the results of the icebreaking simulation and the generation of ice floe spectra are discussed regarding their validity and restrictions. First, the assumptions made in Section 3.1 are analyzed and contextualized in Section 7.1. Afterwards, the restrictions and results of the load spectrum generation are discussed in Section 7.2.

7.1. Assumptions and Restrictions of the Icebreaking Simulation

Sea Ice Model The assumptions made in this work are summed up in Table 2. Regarding the floe field, the assumptions with the highest impact on the resulting breaking behaviour are that the ice floes are assumed to be at fixed positions and therefore no interaction between different floes occurs. Due to the fixed positions, floes can not be pushed away by the bow. This leads to a higher amount of floes that are broken in comparison to the more realistic scenario of non-fixed floe positions. With their lower moment of inertia, smaller floes could be pushed away with less effort than larger ones. Therefore the influence of the assumption of fixed floe positions decreases with increasing floe size. This simplification is chosen in this work due to computational effort, even if this means a loss of generality, especially for small floes.

Additionally, the ice floes are modelled as rigid bodies during the failure by bending and the force-loaded cases at failure by cracking. Thus, they are not deformable elastically but only plastically. For the stress-loaded cases at failure by cracking, instead, the floes can absorb deformation energy and thereby are elastically deformable, even though the ice edge is not adapted to the elastic deformations.

The ice material is assumed to be homogeneous and isotropic. This includes the absence of grain boundaries, dislocations, brine channels and variation of the salinity. Depending on the temperature during growth and the age of the ice, the grain size of sea ice varies between less than 1 mm and more than 50 mm [10]. In comparison to the scale of the ice floes and the structure size – meaning the dimensions of the bow – even the largest ice grain is still very small. Since in this work, the focus lies on the icebreaking process on an engineering scale, the grain-size scale is neglected, although it would influence the breaking pattern slightly.

The ice thickness is assumed to be either constant or normally distributed within a predefined scope. In the latter case, it is not excluded that the thickness at two neighbouring discretization points can have a large difference. As a first approach, this is used to show the ability of the icebreaking algorithm to deal with varying ice thickness. This could be improved by using a low pass filter to avoid large differences between neighbouring points and therefore generate a smooth ice surface.

The surrounding water is modelled using a Winkler-type foundation for the simulation of failure by bending and the force-based approach of failure by cracking. For the energy-based approaches of the failure by cracking, the water is not modelled directly but has to be included in the choice of the fracture toughness, which is used as the cracking threshold. Depending on the choice of this fracture toughness, the modelling of the surrounding water could lead to an inconsistency in the model.

Vessel Model The model of the vessel consists of two bow lines – the upper and the lower ice waterline. These waterlines are at fixed heights and do not change besides the movement in the surge direction. Especially, both heave and pitch are neglected. The mass of the vessel is neglected, since the draught is assumed to be constant, even if ice contact occurs.

The discretization of the bow has to be sufficiently small because the bow is concatenated using linear panels between the discretization points of the upper and lower ice waterline. The larger the discretization distances are, the rougher the results will be. If the simulation should be applied on a vessel going through very thick ice, the discretization of the bow may be adapted, since the curved shape of the bow of an icebreaking vessel leads to different stem angles at different positions at the bow. For the vessel used in this work, combined with the sea ice conditions observed during the expedition Agu19/20, the differences in the stem angle are sufficiently small and therefore, the bow is assumed to be linear in each panel.

The vessel is moved forward after every simulation step using the predefined step width x_{step}. This step width is independent of the ice conditions. The assumption behind this approach is that the propulsion power is always sufficiently high, such that the vessel can always proceed. Another restriction going along with the predefined step width and therefore the predefined vessel positions is the absence of velocity modelling of the vessel. Hence, only the static ice–structure interaction is regarded. The implementation of dynamic effects, for example due to the ship velocity, will probably lead to higher contact forces at the same-sized contact area and therefore, the resulting ice cusps would be smaller. The neglection of vessel velocity results in a more conservative approach regarding the ice cusp sizes and the following forces at propeller–ice interaction. On the other hand, the loads on the bow could be underestimated when neglecting dynamic effects. This has to be taken into account when applying the simulation tool developed in this work to scenarios that focus on the load on the hull.

The bow is discretized for the upper and the lower ice waterline, which are at fixed heights. This can lead to a wrong calculation of the intersection area between the bow and ice floe. In further works, this can be improved by adapting the upper and lower ice waterlines to the actual ice thickness.

Ice–Structure Interaction The decision on the failure mode for floes below the area threshold of bending is made based on the bounding box of the ice floe, such that the bounding box is orthogonal to the current bow panel. The real shape of the ice floe is not considered. This can lead to special cases where the classification during the simulation is not the intended classification because the floe dimension proportions are calculated based on the bounding box instead of the real floe shape. During the testing of different ice configurations and floe fields described in Section 5, this wrong classification happens rarely and the resulting cusps are larger than they would be for the intended classification. This again leads to a more conservative modelling of the cusps that can reach the propeller.

In case of failure by cracking, two further assumptions take effect: First, the fracture mode is assumed to be uniform, meaning that the fracture modes shown in Figure 9 are not combined. In addition, only mode I failure is assumed to occur. In a real icebreaking

scenario, all three fracture modes would be combined, even if the first mode still dominates. It can be assumed that the ice cusps in real icebreaking are less regular than those in this simulation. Second, the cracking once started is assumed to proceed until the end of the floe. This is a direct result of the assumption about homogenous ice without dislocations mentioned above. If the crack tip energy is sufficiently large to initiate cracking and no dislocations are present, then no dissipation occurs and therefore, the crack continues until the end of the floe. To stay consistent during the cracking simulation, this assumption is also made for the force-based cracking description, even if the crack tip energy is not regarded in this case.

If a floe fails by direct rotation due to its position at the bow, it is assumed to stay beside the vessel instead of being pulled underneath it. To achieve a more precise differentiation between floes being pulled underneath the bow and those being pushed to the side of the bow, further flow simulations regarding the bow contour have to be done. As a first assumption in this work, all floes that fail by direct rotation, but not due to their small size, are categorized as not important to the propeller.

The assumed rectangular horizontal crushing areas are a rough approach, which leads to unexpectedly high crushing force values. Due to these high values, floes are broken by bending earlier and in larger pieces than expected. Since a more conservative estimate for the ice-induced propeller loads is chosen, this assumption does not contradict the other assumptions made.

Comparison and Contextualization with other Works The forces occurring at the bow, especially near the shoulder, are unexpectedly high. The same force distribution can be found by Erceg et al. [8]. One possible reason for this phenomenon is the calculation formula of the crushing area. Due to the nonlinear increase of the intersection area between the ice and the bow due to the arbitrarily shaped ice, the crushing area is inaccurate. This inaccuracy has the greatest effect when the angle of the bow panel is small and the bow panel is nearly orthogonal to the ice surface, which is the case for the points near the shoulder.

7.2. Restriction of the Ice Load Spectrum Generation

The ice load spectra generated in this work can be assumed to be a rough approximation of the real load spectra appearing at the propeller. The approximation has to be interpreted with care due to multiple uncertainties of both the icebreaking simulation and the algorithm for the generation of load and torque spectra. The uncertainties of the icebreaking simulation are highlighted in Section 7.1. This section deals with the uncertainties of the algorithm for the generation of the spectra.

The load spectra are based on FEM simulations of exemplary, cuboid ice cusps of different sizes, which are then interpolated using Newton's polynomial. For every exemplary ice cusp, one FEM simulation is conducted. This leads to the neglect of the influence of the cusp position relative to the propeller on the resulting loads and torques. A real propeller blade would experience different torques depending on the distance between the cusp and the propeller shaft. Additionally, the penetration depth of the propeller

directly influences the contact area and therefore the forces exerted by the ice cusp on the propeller. In the FEM simulation, the ice cusps are assumed to interact with the most outward propeller part, which leads to a large lever. Since the algorithm is designed to generate conservative load spectra, this large lever is preferred. Although the preference for large levers exists, they distort the resulting spectra and increase the mean value of the occurring loads and torques artificially.

Another uncertainty lies in the different ice parameters used in the icebreaking simulation and the FEM simulation. These parameter sets are chosen to enable comparability with existing work in each of the two areas. For further improvement, a consistent data set could be used for both parts.

To enable the generation of more realistic load spectra, further information on the cusp flow underneath the vessel is needed. Only then the position of the cusp relative to the propeller can be determined and respected in the generation of load and torque spectra. Additionally, the shape of the ice cusps and the influence of the surrounding water is not respected sufficiently to enable precise load predictions.

In summary, the developed approach for the generation of load and torque spectra is a good starting point to predict the scale of occurring forces and torques. It gives an overview of the possible loads appearing at the propeller. Therefore, specific ice conditions can be taken into account for both the construction of new propulsion systems as well as the navigation planning of existing vessels. The modular structure of the developed simulation allows further improvements on specific simulation parts. This can be used to adapt the simulation to different ice conditions and new findings by further work.

8. Conclusion and Outlook

Within this work, an icebreaking simulation for floe ice is developed and implemented. The existing failure descriptions of the local failure by bending and the global failure by cracking as well as the failure due to direct rotation are extended by the local cracking described in Section 4.3. This is a fourth failure mode which combines the failure initiation of cracking with the breaking pattern of the failure by bending. The simulation is validated for both the crushing forces at the bow in Section 5.1 as well as the generated breaking pattern by comparison with observations and another simulation approach in Section 5.2. Furthermore, the influence of different parameters concerning the simulative and physical control of the model is investigated by a parameter study in Section 5.3.

The simulation can be applied on arbitrary ice floe fields in combination with any icebreaking vessel bow contour to compute the breaking pattern including the ice cusps which are pulled underneath the bow. Additionally, an algorithm for the generation of load and torque spectra based on the computed ice cusps resulting from the icebreaking simulation is developed and applied, which is described in Section 6.1. The generated torque spectrum is compared to field measurement data in Section 6.2. Finally, the assumptions and restrictions of the icebreaking simulation and the ice load spectrum generation are discussed in Section 7.

The icebreaking simulation returns a similar breaking pattern to those observable in both model-scale and full-scale experiments [46, 47]. The crushing forces computed during the simulation are very close to those determined by an existing simulation [8] as well as measured full-scale data [1]. The generated torque spectrum is within the same order of magnitude as the measured torques [39].

With the help of the simulation developed in this work, the forces and torques acting on the propeller and thus the propulsion system can be estimated. This simulation is developed as an alternative approach to the indirect approach by Nickerson and Becker [7] for determining the loads on the propeller. The comparative validations in this work show that the chosen approach can achieve good results at low computational effort even with limited information about the cusp propagation under the hull and the exact floe field distribution in front of the ship. Furthermore, the resulting forces at the bow during the icebreaking process computed by the bow for the whole breaking process have high accordance with the forces determined by another simulation approach by [8], which is validated against measurement data.

In addition, the simulation can easily be adapted to different ice conditions, bow contours and propulsion systems. Therefore, it can be a useful tool during the design of future icebreaking vessels, especially their propulsion system. Furthermore, it can be used during expedition and navigation planning for existing icebreaking vessels, to avoid hazardous propeller–ice interactions. In summary, the developed simulation tool can help prevent damage to the propulsion system in Arctic and Antarctic waters.

Outlook In further work, the floe field can be adapted to an interactive floe field with interactions between neighbouring floes. This can be done as a second simulation in parallel to the icebreaking simulation itself. Additionally, the propulsion power of the

ship can be included in the simulation as well as detailed ship movements. The breaking pattern, especially the pattern of the newly invented local cracking, should be validated experimentally. The flow field of the cusps underneath the ship has to be determined to enable a more precise prediction of the cusps interacting with the propeller and therefore the occurring loads.

To improve the interaction between the icebreaking simulation and the algorithm for the generation of load spectra, more detailed ice observation data is needed. This concerns especially the floe pattern directly in front of the bow as well as the breaking process itself and the number of ice cusps that migrate in the propeller. A future expedition in arctic or antarctic regions could gather a coherent data set consisting of torque data at the propulsion shaft, detailed ice observation data including image data from the ice floes at the bow and the stern as well as underwater recordings of the icebreaking and cusp-migration process.

References

[1] Lutz Hoffmann. Impact forces and friction coefficent on the forebody of the german polar research vessel "Polarstern". In *POAC'85, 8th International Conference on Port and Ocean Engineering Under Arctic Conditions*, 1985.

[2] Mikko Suominen, Jouko Karhunen, Anriëtte Bekker, Pentti Kujala, Mikko Elo, Håkan Enlund, Sami Saarinen, et al. Full-scale measurements on board psrv sa agulhas ii in the baltic sea. In *Proceedings of the International Conference on Port and Ocean Engineering Under Arctic Conditions*, 2013.

[3] Mikko Suominen. *Uncertainty and variation in measured ice-induced loads on a ship hull*. PhD thesis, Aalto University, 2018.

[4] Olaf Boebel. The expedition ps89 of the research vessel Polarstern to the weddell sea in 2014/2015, 2015.

[5] Nick Blenkey. Polar star beats engineering challenges to complete mission. `https://www.marinelog.com/news/video-polar-star-beats-engineering-challenges-to-complete-mission/`, 2018. accessed: 14 Aug 2023.

[6] Greg Dobie. Safety and shipping review 2017, 2017.

[7] Brendon Mark Nickerson and Anriëtte Bekker. Inverse model for the estimation of ice-induced propeller moments using modal superposition. *Applied Mathematical Modelling*, 102:640–660, 2022.

[8] Sandro Erceg, Boris Erceg, Franz von Bock und Polach, and Sören Ehlers. A simulation approach for local ice loads on ship structures in level ice. *Marine Structures*, 81:103117, 2022.

[9] Erland M Schulson. The structure and mechanical behavior of ice. *Jom*, 51:21–27, 1999.

[10] GW Timco and WF Weeks. A review of the engineering properties of sea ice. *Cold regions science and technology*, 60(2):107–129, 2010.

[11] Hauke John Herrnring. *Experimental and numerical investigation of brittle ice crushing loads*. PhD thesis, Technische Universität Hamburg, 2023.

[12] Agnieszka Herman. Molecular-dynamics simulation of clustering processes in sea-ice floes. *Physical Review E*, 84(5):056104, 2011.

[13] Agnieszka Herman. Influence of ice concentration and floe-size distribution on cluster formation in sea-ice floes. *Central European Journal of Physics*, 10:715–722, 2012.

[14] Agnieszka Herman. Numerical modeling of force and contact networks in fragmented sea ice. *Annals of glaciology*, 54(62):114–120, 2013.

[15] Agnieszka Herman. Wave-induced stress and breaking of sea ice in a coupled hydrodynamic discrete-element wave–ice model. *The Cryosphere*, 11(6):2711–2725, 2017.

[16] Mark A Hopkins and Alan S Thorndike. Floe formation in arctic sea ice. *Journal of Geophysical Research: Oceans*, 111(C11), 2006.

[17] Alberto Alberello, Luke Bennetts, Petra Heil, Clare Eayrs, Marcello Vichi, Keith MacHutchon, Miguel Onorato, and Alessandro Toffoli. Drift of pancake ice floes in the winter antarctic marginal ice zone during polar cyclones. *Journal of Geophysical Research: Oceans*, 125(3):e2019JC015418, 2020.

[18] Donald E Nevel. The narrow free infinite wedge on an elastic foundation. *Cold Regions Research and Engineering Laboratory (US)*, 1961.

[19] Gustav Lindqvist. A straightforward method for calculation of ice resistance of ships. *POAC'89*, 1989.

[20] Wenjun Lu, Raed Lubbad, and Sveinung Løset. In-plane fracture of an ice floe: A theoretical study on the splitting failure mode. *Cold Regions Science and Technology*, 110:77–101, 2015.

[21] Wenjun Lu, Raed Lubbad, Sveinung Løset, and Marat Kashafutdinov. Fracture of an ice floe: Local out-of-plane flexural failures versus global in-plane splitting failure. *Cold Regions Science and Technology*, 123:1–13, 2016.

[22] Wenjun Lu, Hans-Martin Heyn, Raed Lubbad, and Sveinung Løset. A large scale simulation of floe-ice fractures and validation against full-scale scenario. *International Journal of Naval Architecture and Ocean Engineering*, 10(3):393–402, 2018.

[23] Rui Li, Yang Zhong, and Ming Li. Analytic bending solutions of free rectangular thin plates resting on elastic foundations by a new symplectic superposition method. *Proceedings of the Royal Society A: Mathematical, Physical and Engineering Sciences*, 469(2153):20120681, 2013.

[24] Jeong-Hwan Kim, Wenjun Lu, Raed Lubbad, Sveinung Løset, and Beom-Seon Jang. Dynamic bending of an ice wedge resting on a winkler-type elastic foundation. *Cold Regions Science and Technology*, 199:103579, 2022.

[25] Oriol Jou, Miguel Angel Celigueta, Salvador Latorre, Ferrán Arrufat, and Eugenio Oñate. A bonded discrete element method for modeling ship–ice interactions in broken and unbroken sea ice fields. *Computational Particle Mechanics*, 6:739–765, 2019.

[26] Zdeněk P Bažant. Size effect in blunt fracture: concrete, rock, metal. *Journal of engineering mechanics*, 110(4):518–535, 1984.

[27] Zdeněk P Bažant and Phillip A Pfeiffer. Determination of fracture energy from size effect and brittleness number. *ACI Materials Journal*, 84(6):463–480, 1987.

[28] JP Dempsey, RM Adamson, and SV Mulmule. Scale effects on the in-situ tensile strength and fracture of ice. Part II: First-year sea ice at Resolute, NWT. *International journal of fracture*, 95(1-4):347–366, 1999.

[29] Luofeng Huang, Jukka Tuhkuri, Bojan Igrec, Minghao Li, Dimitris Stagonas, Alessandro Toffoli, Philip Cardiff, and Giles Thomas. Ship resistance when operating in floating ice floes: A combined CFD&DEM approach. *Marine Structures*, 74:102817, 2020.

[30] Shotaro Uto, Haruhito Shimoda, Daisuke Wako, and Takatoshi Matsuzawa. NSR transit simulations by the vessel performance simulator "VESTA". part 2: Simple resistance formulae of ships in floe ice. In *Proceedings of the International Conference on Port and Ocean Engineering Under Arctic Conditions*, 2015.

[31] Chao Wang, Xiaohan Hu, Taiping Tian, Chunyu Guo, and Chunhui Wang. Numerical simulation of ice loads on a ship in broken ice fields using an elastic ice model. *International Journal of Naval Architecture and Ocean Engineering*, 12:414–427, 2020.

[32] Raed Lubbad and Sveinung Løset. A numerical model for real-time simulation of ship–ice interaction. *Cold Regions Science and Technology*, 65(2):111–127, 2011.

[33] Junji Sawamura. 2D numerical modeling of icebreaker advancing in ice-covered water. *International Journal of Naval Architecture and Ocean Engineering*, 10(3):385–392, 2018.

[34] Harri Soininen. *A propeller-ice contact model*, volume 343. Technical Research Centre of Finland, 1998.

[35] Brian Veith. *Prediction of ice contact forces on a marine screw propeller during the propeller-ice cutting process*. PhD thesis, Helsinki University of Technology, 1995.

[36] Angelo Mario Böhm, Hauke Herrnring, and Franz von Bock und Polach. Data from uniaxial compressive testing of laboratory-made granular ice. *Data in Brief*, 42:108236, 2022.

[37] Angelo Mario Böhm, Hauke Herrnring, and Franz von Bock und Polach. Splitting-tests of laboratory-made granular ice with a propeller-like indenter. *International Conference on Offshore Mechanics and Arctic Engineering*, 2022.

[38] Angelo Mario Böhm, Franciska Müller, Hauke Herrnring, and Franz von Bock und Pollach. High-speed impact drop tower-test of cylindrical granular ice specimens. *POAC'23, 27th International Conference on Port and Ocean Engineering Under Arctic Conditions*, 27, 2023.

[39] Etienne Purcell, Amir R Nejad, and Anriëtte Bekker. Detection of ice using ship propulsion and navigation measurements. *Ocean Engineering*, 273:113992, 2023.

[40] Det Norske Veritas (DNV). Vessel register for DNV - S.A. Agulhas II. `https://vesselregister.dnv.com/vesselregister/details/30528`, 2022. accessed: 8 Aug 2023.

[41] Dietmar Gross and Thomas Seelig. *Fracture mechanics: with an introduction to micromechanics*. Springer, 2017.

[42] HW Liu and KJ Miller. Fracture toughness of fresh-water ice. *Journal of glaciology*, 22(86):135–143, 1979.

[43] Mark P Fischer, Richard B Alley, and Terry Engelder. Fracture toughness of ice and firn determined from the modified ring test. *Journal of glaciology*, 41(138):383–394, 1995.

[44] Julia Christmann, Ralf Müller, Kyle G Webber, Daniel Isaia, Florian H Schader, Sepp Kipfstuhl, Johannes Freitag, and Angelika Humbert. Measurement of the fracture toughness of polycrystalline bubbly ice from an antarctic ice core. *Earth System Science Data*, 7(1):87–92, 2015.

[45] JP Dempsey, DM Cole, and Shen Wang. Tensile fracture of a single crack in first-year sea ice. *Philosophical Transactions of the Royal Society A: Mathematical, Physical and Engineering Sciences*, 376(2129):20170346, 2018.

[46] Fernando Puntigliano. *Review of Ship Resistance in Level Ice*. Institut für Schiffbau, 1993.

[47] Robert Ettema, Frederick Stern, Javier Lazaro, et al. Dynamics of continuous-mode icebreaking by a polar-class icebreaker hull. Technical report, Iowa Institute of Hydraulic Research, University of Iowa, 1987.

[48] Claude Daley. Ice class rules - description and comparison. Memorial University St. John's, Canada, 2014.

[49] Jan Babicz. Wärtsilä encyclopedia of ship technology. 2015.

[50] RJO De Waal, A Bekker, and Philippus Stephanus Heyns. Data for indirect load case estimation of ice-induced moments from shaft line torque measurements. *Data in brief*, 19:1222–1236, 2018.

[51] International Maritime Organization (IMO). Clasifications register rules and regulations - rules and regulations for the classification of ships, july 2022 - part 8 rules for ice and cold operations - chapter 2 ice operations - ice class - section 11 machinery strengthening requirements for navigation in multi-year ice conditions – ice classes pc1, pc2, pc3, pc4, pc5, pc6, pc7 and icebreaker. `https://www.imorules.com/LRSHIP_PT8_CH2_11.html`, 2022. accessed: 5 Jul 2023.

[52] Brendon Mark Nickerson and Anriëtte Bekker. Recommendations for regularization in the inverse estimation of ice-induced propeller moments for ice-going vessels. *Cold Regions Science and Technology*, 192:103378, 2021.

A. Appendix

A.1. Algorithms of Ice Floe Breaking

Algorithm 2: Failure mode classification

input : ice_floe_object, $this\_bow\_panel$
output: $failure\_mode$

Get bounding box of ice_floe_object with orientation s. t. box is perpendicular to $this\_bow\_panel$
Get member variables $width$ and $length$ of ice_floe_object ()
$\ell \leftarrow$ (set_characterstic_length)()
if $get\_area() \leq 13.5(\mathbf{mean}(thickness))^{\frac{3}{4}}$ **then**
  $failure\_mode \leftarrow$ `'unbreakable'`
else if $width \leq 2\ell$ ***or*** $length \leq 2\ell$ **then**
  if $width \leq length$ **then**
    $failure\_mode \leftarrow$ `'bending'`
  else
    $failure\_mode \leftarrow$ `'cracking'`
else
  $failure\_mode \leftarrow$ `'bending'`

Algorithm 3: Contact Forces

def *contact_forces(A_c)*:

`// contact coefficient` $k_c = 1$, `crushing strength` $\sigma_c = 1280\,\mathrm{kPa}$, `friction coefficient` $\mu = 0.15$

$F_c \leftarrow k_c \sigma_c A_c$ `// Crushing force`

$F_v \leftarrow F_c \mathbf{sin}(bow.\psi) - \mu F_c \mathbf{cos}(bow.\psi)$ `// Vertical crushing force`

$F_h \leftarrow F_c \mathbf{cos}(bow.\psi) - \mu F_c \mathbf{sin}(bow.\psi)$ `// Horizontal crushing force`

return F_c, F_v, F_h

Algorithm 4: Bending Line

input : ice_floe_object, bow_object, A_c, (O_x, O_y), (W_x, W_y)
// A_c: contact area, (Ox, Oy): common origin of discretized wedges, Wx : wedge distribution points x, Wy: wedge distribution points y
output: ice_floe_object, $xInt$, $yInt$, k

$F_c, F_v, F_h \leftarrow contact_forces(A_c)$
Compute breaking length and store to l_{br}
Compute bearing capacity and store to P
$W_{\text{vec}} \leftarrow (Wx, Wy)^T$ // Array with wedge distribution points
$O_{\text{vec}} \leftarrow \mathbf{ones}(\mathbf{len}(W_x))(O_x, O_y)^T$
$V \leftarrow W_{\text{vec}} - O_{\text{vec}}$ // Array with direction vectors to wedge center lines
Normalize V and store to U
$B \leftarrow O_{\text{vec}} + l_{\text{br}}U$ // breaking points
$ice\_floe\_object.xCusp \leftarrow B[0]$
$ice\_floe\_object.yCusp \leftarrow B[1]$
if $Fv > P$ **then**
  $xInt, yInt \leftarrow$ intersection between bending line and ice edge
  $k = 1$ // key for failure by bending
else
  $k = 0$ // key for no failure
return $ice\_floe\_object, xInt, yInt, k$

Algorithm 5: Cracking Line

input : ice_floe_object, bow_object, A_c, (O_x, O_y), (W_x, W_y)
// A_c: contact area, (Ox, Oy): common origin of discretized wedges, Wx : wedge distribution points x, Wy: wedge distribution points y, ℓ: characteristic length
output: ice_floe_object, $xInt$, $yInt$, k

$F_c, F_v, F_h \leftarrow contact_forces(A_c)$
Compute bearing capacity and store to P
$bowVecNormal \leftarrow$ Compute normal vector with length 1 of bow segment intersecting with ice
$midBow \leftarrow$ Find bow point in the middle of intersection with ice
$startCusp \leftarrow midBow - bowVecNormal\frac{\ell}{5}$
$endCusp \leftarrow startCusp + bowVecNormal\frac{\ell}{5} + bowVecNormal5\ell$
$ice\_floe\_object.xCusp \leftarrow$ **arange**$(startCusp[0], endCusp[0], 30)$
$ice\_floe\_object.yCusp \leftarrow$ **arange**$(startCusp[1], endCusp[1], 30)$
Check fracture criterion (Algorithm 7)
if *Fracture* **then**
  $xInt, yInt \leftarrow$ intersection between bending line and ice edge
  $k = -1$ // key for failure by cracking
else
  $k = 0$ // key for no failure
return $ice\_floe\_object, xInt, yInt, k$

Algorithm 6: Local Cracking Line

input : ice_floe_object, bow_object, A_c, (O_x, O_y), (W_x, W_y)
// A_c: contact area, (Ox, Oy): common origin of discretized wedges, Wx : wedge distribution points x, Wy: wedge distribution points y
output: ice_floe_object, $xInt$, $yInt$, k

$F_c, F_v, F_h \leftarrow contact_forces(A_c)$
Compute breaking length and store to l_{br}
Compute bearing capacity and store to P
// first part of breaking line
$bowVecNormal \leftarrow$ Compute normal vector with length 1 of bow segment intersecting with ice
$midBow \leftarrow$ Find bow point in the middle of intersection with ice
$startCusp \leftarrow midBow - bowVecNormal\frac{\ell}{5}$
$endCusp \leftarrow startCusp + bowVecNormal\frac{\ell}{5} + bowVecNormal5\ell$
$ice\_floe\_object.xCusp \leftarrow$ **arange**$(startCusp[0], endCusp[0], 30)$
$ice\_floe\_object.yCusp \leftarrow$ **arange**$(startCusp[1], endCusp[1], 30)$
// last part of breaking line
$W_{\text{vec}} \leftarrow (Wx, Wy)^T$ // Array with wedge distribution points
$O_{\text{vec}} \leftarrow$ **ones**(**len**$(W_x))(O_x, O_y)^T$
$V \leftarrow W_{\text{vec}} - O_{\text{vec}}$ // Array with direction vectors to wedge center lines
Normalize V and store to U
$B \leftarrow O_{\text{vec}} + l_{\text{br}}U$ // breaking points
$xCuspEnd \leftarrow B[0]$
$yCuspEnd \leftarrow B1$
// connecting breaking lines
$xCuspMid, yCuspMid \leftarrow$ Bezier Curve between first and last breaking line
Check fracture criterion (Algorithm 7)
if *Fracture* **then**
  $xInt, yInt \leftarrow$ intersection between bending line and ice edge
  $k = -1$ // key for failure by cracking
else
  $k = 0$ // key for no failure
return $ice\_floe\_object, xInt, yInt, k$

Algorithm 7: Fracture Criterion for Failure by Cracking

```
// Fracture criterion functions for different failure cases for
   failure by cracking
def facture_criterion_simple(F_h, P):
    return F_h > P
def facture_criterion_mode1(F_h, K_Ic, a):
    // horizontal crushing force F_h, fracture toughness K_Ic, crack
       length a
    F_cr ← 1/(2 tan(0.5α)) F_h                    // bow angle at bow tip α = 64.54°
    K_I ← 0.878 F_cr √(π/a)
    return K_I > K_Ic
def facture_criterion_mode1(K_Ic, a, b):
    // fracture toughness K_Ic, crack length a, floe length b
    G_I ← (0.923 + 0.199(1 − sin((πa)/(2b)))^4)/(cos((πa)/(2b)))
    K_I ← σ_tn √(πa) √((2b)/(πa) tan((πa)/(2b))) G_I(a/b)
                          // σ_tn: tensile strength using scale effect law
    return K_I > K_Ic
def facture_criterion_mode1(K_Ic, a, b):
    // fracture toughness K_Ic, crack length a, floe length b
    G_I ← (0.752 + 2.02a/b + 0.37(1 − sin((πa)/(2b)))^3)/(cos((πa)/(2b)))
    K_I ← σ_tn √(πa) √((2b)/(πa) tan((πa)/(2b))) G_I(a/b)
                          // σ_tn: tensile strength using scale effect law
    return K_I > K_Ic
```

A.2. Measured Torque Data

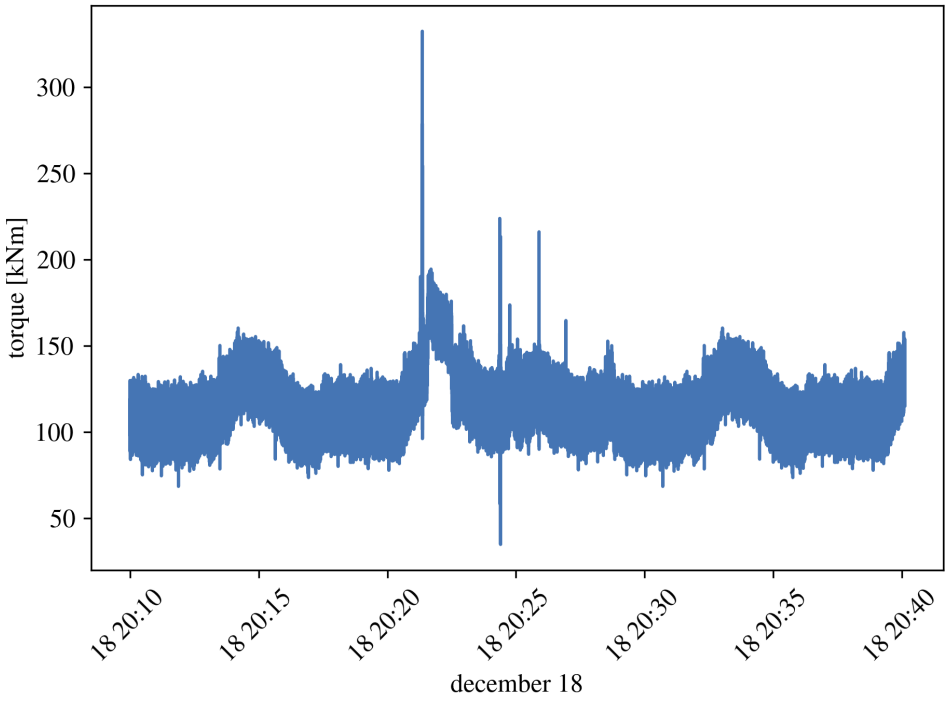

Figure 36: Measured torques at the propulsion shaft of PSRV S.A. AGULHAS II in ice thickness $h = 0.4\,\mathrm{m}$. The period between 20:20 and 20:30 is used in this work as a comparison. The peaks can be caused by contact with large ice cusps.

A.3. Measured and Simulated Torque Spectra

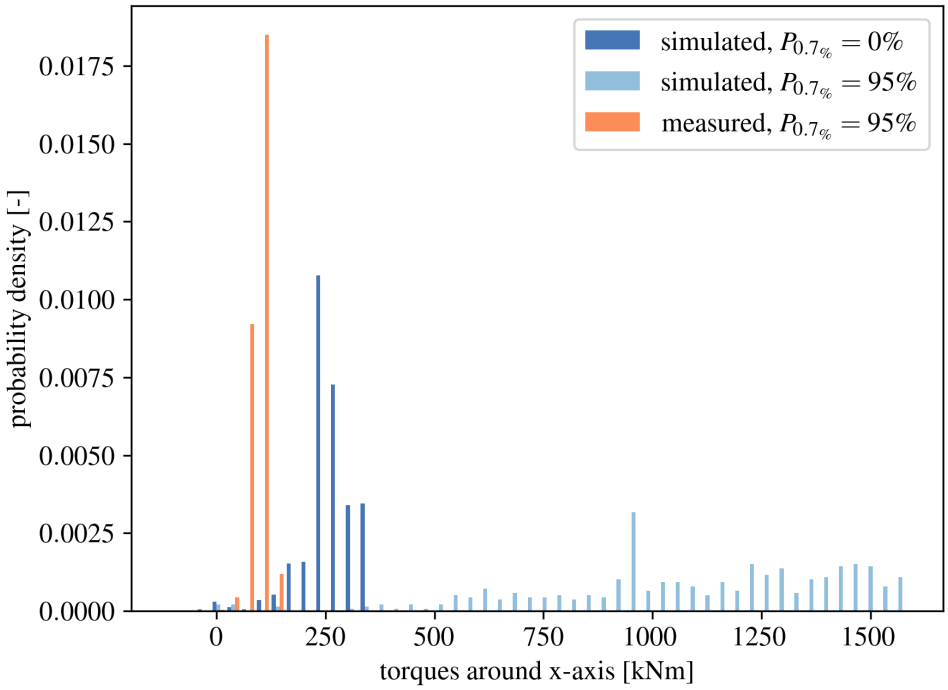

Figure 37: Spectrum of the measured torques at the propulsion shaft and simulated torques at the propeller of PSRV S.A. AGULHAS II in ice thickness $h = 0.4\,\mathrm{m}$. The simulated torques are multiplied by -1 for better comparability.

A.4. Computation of Bearing Capacity

Computation of the bearing capacity as described by Erceg et al. [8]. The bearing coefficients used in `bearing_capacity` are given by Nevel [18].

```
import numpy as np
import scipy
import bearing_coefficients
def bearing_capacity_interpolated(h, r, gamma):
    """
    :param h: ice thickness (m)
    :param r: loading radius (m)
    :param gamma: wedge angle, deg
    :return: interpolated value of bearing capacity P for the comibation of ice thickness, loading radius and wedge angle
    """
    r_vec = np.array([0.1, 0.3, 0.6, 1.0, 1.5])
    gamma_vec_upper = [60, 90, 105, 135, 165, 180]
    gamma_vec = np.concatenate((np.arange(1, 60, 1), gamma_vec_upper))
    h_vec = [0.0, 0.3, 0.6, 0.9, 1.2]

    # use boundary values if r is out of range
    r[r<r_vec[0]] = r_vec[0]
    r[r>r_vec[-1]] = r_vec[-1]

    if np.min(np.abs(r - r_vec)) < 1e-10:
        r1 = r
        r2 = r
    else:
        r1 = r_vec[(np.where(r_vec > r)[0]-1)[0]] # take the element before the first element that fulfills r_vec > r
        r2 = r_vec[np.where(r_vec > r)[0][0]] # take the first element that fulfills r_vec > r

    # use boundary values if gamma is out of range
    if np.min(np.abs(gamma - gamma_vec_upper)) < 1e-10:
        gamma1 = gamma
        gamma2 = gamma
    elif gamma > 180:
        gamma1 = 180
        gamma2 = 180
    else:
        gamma1 = gamma_vec[(np.where(gamma_vec > gamma)[0]-1)[0]] # take the element before the first element that fulfills gamma_vec > gamma
        gamma2 = gamma_vec[np.where(gamma_vec > gamma)[0][0]] # take the first element that fulfills gamma_vec > gamma

    if np.min(np.abs(h - h_vec[1:])) < 1e-10:
        h1 = h
        h2 = h
    elif h > 1.2:
        h1 = 1.2
        h2 = 1.2
    else:
        h1 = h_vec[np.where(h_vec > h)[0][-1]]
        h2 = h_vec[np.where(h_vec > h)[0][0]]
```

```
47
48      P111 = bearing_capacity(h1, r1, gamma1, r_vec, gamma_vec)
49      P112 = bearing_capacity(h1, r1, gamma2, r_vec, gamma_vec)
50      P121 = bearing_capacity(h1, r2, gamma1, r_vec, gamma_vec)
51      P122 = bearing_capacity(h1, r2, gamma2, r_vec, gamma_vec)
52      P211 = bearing_capacity(h2, r1, gamma1, r_vec, gamma_vec)
53      P212 = bearing_capacity(h2, r1, gamma2, r_vec, gamma_vec)
54      P221 = bearing_capacity(h2, r2, gamma1, r_vec, gamma_vec)
55      P222 = bearing_capacity(h2, r2, gamma2, r_vec, gamma_vec)
56
57      # averaging for the wedge angle (gamma) value
58      P11 = (P111 + P112)/2
59      P12 = (P121 + P122)/2
60      P21 = (P211 + P212)/2
61      P22 = (P221 + P222)/2
62
63      # averaring for the ice thickness value
64      P1 = (P11 + P21)/2
65      P2 = (P12 + P22)/2
66
67      # final averaging is averaging for the value of loading radius
68      P = (P1 + P2)/2 # interpolated values of the bearing capacity for the desired
    values of (h, r, gamma), kN
69
70      return P
```

```
4   def bearing_capacity(h, r, gamma, r_vec, gamma_vec):
5       """
6       :param h: ice thickness (m)
7       :param r: loading radius (m)
8       :param gamma: wedge angle, deg
9       :return: bearing capacity P (kN), for desired combination of ice thickness,
    loading radius and wedge angle
10      """
11      if np.abs(h - 0) < 1e-10:
12          myP = bearing_coefficients.P1
13      elif np.abs(h - 0.3) < 1e-10:
14          myP = bearing_coefficients.P1
15      elif np.abs(h - 0.6) < 1e-10:
16          myP = bearing_coefficients.P2
17      elif np.abs(h - 0.9) < 1e-10:
18          myP = bearing_coefficients.P3
19      elif np.abs(h - 1.2) < 1e-10:
20          myP = bearing_coefficients.P4
21      else:
22          raise ValueError('h must be 0, 0.3, 0.6, 0.9 or 1.2')
23
24      r[r<r_vec[0]] = r_vec[0]
25
26      r[r>r_vec[-1]] = r_vec[-1]
27
28      if gamma > 180:
29          gamma = 180
30
31      P = scipy.interpolate.interpn((r_vec, gamma_vec), myP, (r, gamma),
    method='linear', bounds_error=False, fill_value=None)
32      return P
```